UNIVERSIDAD POLITÉCNICA DE MADRID
Escuela Técnica Superior de Ingenieros de Caminos, Canales y Puertos

Bifurcation of tubes under several loading conditions with application to arteries

D O C T O R A L T H E S I S

Submitted for the degree of Doctor by:

Soheil Moradalizadeh
Civil and Structural Engineering, MSc.

Madrid 2025


UNIVERSIDAD POLITÉCNICA DE MADRID
Escuela Técnica Superior de Ingenieros de Caminos, Canales y Puertos

DOCTORAL DEGREE IN ENGINEERING OF STRUCTURES, FOUNDATIONS AND MATERIALS

Bifurcation of tubes under several loading conditions with application to arteries

D O C T O R A L T H E S I S

Submitted for the degree of Doctor by:

Soheil Moradalizadeh
Civil and Structural Engineering, MSc.

Under the supervision of:
Professor José Merodio

Madrid, 2025

Title: Bifurcation of tubes under several loading conditions with application to arteries

Author: Soheil Moradalizadeh

Doctoral Programme: ENGINEERING OF STRUCTURES, FOUNDATIONS AND MATERIALS

Thesis Supervision:

Dr. José Merodio, Professor, Departamento de Matemática Aplicada a las TIC, Escuela Técnica Superior de Ingeniería de Sistemas Informáticos (ETSISI), Universidad Politécnica de Madrid

Thesis external reviewers:

Thesis Defense Committee:

Thesis Defense Date:

To my family

Acknowledgement

I would like to express my deepest gratitude to Prof. José Merodio for his invaluable guidance and unwavering support throughout the development of my thesis. His extensive knowledge and insightful advice have been a source of inspiration and motivation during my research journey. This work would not have been possible without his mentorship and encouragement.

Abstract

Aneurysms in arterial wall tissues represent a significant medical challenge due to their potential for rupture, leading to severe consequences such as hemorrhage, stroke, or death. The constitution of aneurysms is a complex process influenced by various bio-mechanical and physiological factors. Under-stressed thin- and thick-walled cylindrical tubes have garnered attention in recent research, as geometric instabilities within these structures play a crucial role in aneurysm formation. Inflated tubes may face various types of instabilities, which result from factors such as geometry, properties of the materials, and loading types. Determining the onset of bifurcation instabilities in soft structures presents significant challenges due to the distinct qualitative differences between bifurcation and post-bifurcation behaviors. The bifurcation of an inflated and extended swellable isotropic cylindrical membrane is addressed in chapter three considering a combination of the neo-Hookean material and the Demiray models. This model found its use in the modeling of various types of soft tissue in which swelling is important but was not considered. The presented results may be helpful in the planning of more complex numerical treatments, which will invoke larger computational resources. Moreover, non-linear finite element analysis of double-layered cylindrical tubes including residual stresses subjected to axial stretch and internal pressure were carried out to investigate the application of mechanical and material aspect in developing abdominal aortic aneurysms (AAA) and aneurysm rupture in chapter four. In this regard, bulging and bending instabilities regarding the axial stretches and initial condition were investigated. The results show that for large values of axial stretch, the axial stress is sufficiently large to produce bulging instability rather than bending instabilities. Moreover, combined modes of bulging bifurcations were observed for double-layered cylindrical tubes, which can aggravate the possibility of developing of abdominal aortic aneurysms (AAA). For axial stretches lower than 1.2, bending bifurcations were captured. Also, the results revealed that residual stresses significantly affect bifurcation outcomes compared to models without residual stress, underscoring their importance in accurately modeling biological tissues such as arteries and related cardiovascular conditions like aneurysms. The study also examined helical stability in elastic cylinders. A doubly fiber-reinforced, incompressible, nonlinear elastic tube subjected to axial loading, internal pressure, and twist was analyzed using a modified Riks procedure. These loading conditions, mimicking physiological scenarios in arteries, produced tortuous shapes and complex morphologies, such as helical coiling, looping, and winding. These configurations, highly sensitive to pressure, axial stretch, and twist, were simulated using an anisotropic constitutive model incorporating fiber stretching and shearing, extending previous research focused solely on fiber stretching.

Resumen

Los aneurismas en los tejidos de las paredes arteriales representan un desafío médico significativo debido a su potencial de ruptura, lo que puede llevar a consecuencias graves como hemorragias, accidentes cerebrovasculares y la muerte. La formación de los aneurismas es un proceso complejo influenciado por diversos factores biomecánicos y fisiológicos. Los tubos cilíndricos de pared delgada y gruesa sometidos a bajos niveles de estrés han ganado atención en investigaciones recientes, ya que las inestabilidades geométricas dentro de estas estructuras pueden desempeñar un papel crucial en la formación de los aneurismas. Los tubos inflados pueden enfrentar varios tipos de inestabilidades, que resultan de factores como la geometría, las propiedades de los materiales y los tipos de carga. Determinar el inicio de las inestabilidades de bifurcación en estructuras blandas presenta desafíos significativos debido a las diferencias cualitativas entre los comportamientos de bifurcación y post-bifurcación. La bifurcación de una membrana cilíndrica isótropa inflada y extendida con capacidad de hinchamiento se aborda en el capítulo tres, considerando una combinación del modelo de material neo-Hookeano y el modelo de Demiray. Este modelo ha sido utilizado en la modelización de diversos tipos de tejidos blandos en los que el hinchamiento es importante. Los resultados presentados pueden ser útiles para la planificación de tratamientos numéricos más complejos, que requerirán mayores recursos computacionales. Además, en el capítulo cuatro se realizó un análisis no lineal por elementos finitos de tubos cilíndricos de doble capa, incluyendo tensiones residuales, sometidos a estiramiento axial y presión interna, con el objetivo de investigar la aplicación de aspectos mecánicos y de materiales en el desarrollo de aneurismas de aorta abdominal (AAA) y su ruptura. En este contexto, se investigaron las inestabilidades de abultamiento y flexión en relación con los estiramientos axiales y las condiciones iniciales. Los resultados muestran que, para valores grandes de estiramiento axial, la tensión axial es lo suficientemente grande como para producir inestabilidad por abultamiento en lugar de inestabilidades de flexión. Además, se observaron modos combinados de bifurcaciones en tubos cilíndricos de doble capa, lo que puede agravar la posibilidad de desarrollar aneurismas de aorta abdominal (AAA). Para estiramientos axiales menores a 1.2, se capturaron bifurcaciones de flexión. Asimismo, los resultados revelaron que las tensiones residuales afectan significativamente los resultados de la bifurcación en comparación con los modelos sin tensiones residuales, subrayando su importancia para modelar con precisión tejidos biológicos como las arterias y condiciones cardiovasculares relacionadas, como los aneurismas. El estudio también examinó la estabilidad helicoidal en cilindros elásticos. Se analizó un tubo elástico no lineal, incomprensible y reforzado con fibras dobles, sometido a carga axial, presión interna y torsión, utilizando un procedimiento de Riks modificado. Estas condiciones de carga, que imitan escenarios fisiológicos en las arterias, produjeron formas tortuosas y morfologías complejas, como enrollamientos helicoidales y bucles. Estas configuraciones, altamente sensibles a la presión, el estiramiento axial y la torsión, se simularon utilizando un modelo constitutivo anisótropo que incorpora el estiramiento y el corte de fibras, extendiendo investigaciones previas enfocadas exclusivamente en el estiramiento de fibras.

Table of Contents

List of Figures

List of Tables

Chapter 1

Introduction

1.1 Overview

In this chapter, a brief overview on the motivations, applications, methods, goals, and contents of the presented thesis is provided. The motivations and applications of modeling of human tissues, structural instabilities of arteries, residual stresses are dealt with in the first three sections. Next, a summary of aneurysm in arterial wall tissues is presented. Later, an introduction to the methodology and analyses used in this work in presented and the goals of the presented thesis are provided in Section 1.4. At last, Section 1.5 provides a categorization of this thesis.

1.2 Motivation and application

Computational modeling of human blood vessels, such as those located in the brain and cardiovascular system, offers the capability for a deeper comprehension of the causes and effects of biological organ-related issues, the anticipation of how the human body will respond to various conditions such as diseases, external loads, treatments, paving the way for a better understanding of risk factors and leading to more efficient and safer choices. Additionally, this knowledge can expedite the development of modern bio-medical and surgical instruments tailored to specific environments, which is increasingly critical in contemporary contexts. Furthermore, advancements in modeling and simulation technologies are driving the production of artificial tissues mimicking the properties of natural human tissues, facilitating further progress in medical research and innovation.

Multiple studies have demonstrated that blood vessels can exhibit intricate patterns of buckling deformation, especially when experiencing pathological conditions. A buckling deformation is referred to a condition under which the vessels exhibit instability. Aside from conditions related to genetics or diseases, these instabilities can be the results of mechanical properties, such as material non-linearity, bulging bifurcation, bending bifurcation, etc. Reliable computer modeling offers distinct and significant advantages over traditional approaches.It is non-invasive, cost-effective, and has the potential to unveil crucial physiological

mechanisms. Despite considerable advancements in recent decades, numerous challenges persist in the domain of instabilities observed in both thin-walled and thick-walled cylinders, such as arteries, subjected to various boundary conditions.The mechanical modeling of human tissues necessitates a sophisticated integration of strongly linked multi-scale and multi-physics mechanisms, alongside non-linear elasticity and residual stresses. Numerous sources have explored these aspects, highlighting their importance in understanding the behavior of tissues at various scales and under different conditions. Despite these efforts, many aspects remain to be fully addressed and understood.

In recent years, there has been growing interest among researchers in the geometric instabilities observed in under-stressed thin- and thick-walled cylindrical tubes, such as blood vessels. This focus has led to numerous studies exploring the role of such structures in the development and propagation of aneurysms within arterial wall tissues. Typically, stress is expected to maintain a homeostatic balance in standard vessels. However, aneurysms exhibit highly degenerative walls, where the biological mechanisms responsible for remodeling towards homostatic stress are impaired, leading to pathological alterations in structural proteins. In addition to the geometric properties of the tubes, the formation of aneurysms involves a multitude of biomechanical factors, including cell degradation, aging, material heterogeneity, biochemical reactions, and anisotropy. Nonetheless, understanding the mechanical modulation of this process is crucial for potential inclusion in future biochemical applications and warrants thorough investigation.

1.3 An overview on the constitution and propagation of aneurysms in arterial wall tissues

Aneurysms in arterial wall tissues represent a significant medical challenge due to their potential for rupture, leading to severe consequences such as hemorrhage, stroke, or death. The constitution of aneurysms is a complex process influenced by various bio-mechanical and physiological factors. Under-stressed thin- and thick-walled cylindrical tubes have garnered attention in recent research, as geometric instabilities within these structures play a crucial role in aneurysm formation. Studies have demonstrated that the standard vessel's homeostatic stress maintenance is disrupted in aneurysms, leading to pathological remodeling of structural proteins. This disruption, combined with factors such as cell degradation, aging, material heterogeneity, biochemical reactions, and anisotropy, contributes to the degenerative changes observed in aneurysmal walls.

Aneurysm propagation further complicates the clinical management of these conditions. Once formed, aneurysms exhibit dynamic behavior, with the potential for growth, rupture, or stabilization. Hemo-dynamic forces, including pressure gradients and blood flow patterns, exert mechanical stress on the arterial wall, influencing the progression of aneurysms. Computational models have been developed to simulate these hemo-dynamic conditions and predict aneurysm growth and rupture risk, aiding clinicians in treatment decision-making. Advances in imaging modalities, such as magnetic resonance imaging (MRI) and computed tomography angiography (CTA), have enabled the non-invasive detection and characterization of aneurysms, facilitating early diagnosis and intervention. However, challenges remain in accurately assessing aneurysm

stability and predicting individualized patient outcomes.

The mechanical modulation of aneurysm formation and progression holds promise for future therapeutic interventions. Targeting bio-mechanical factors implicated in aneurysm patho-genesis, such as abnormal stress distribution and structural weakness, may offer new avenues for treatment. Bio-mechanical approaches aiming to reinforce the arterial wall promote healing, thereby reducing the risk of rupture and improving patient outcomes. In conclusion, understanding the constitution and propagation of aneurysms in arterial wall tissues requires a multi-disciplinary approach integrating bio-mechanics, physiology, imaging, and computational modeling. By elucidating the underlying mechanisms driving aneurysm development and progression, clinicians and researchers can develop more effective strategies for prevention, diagnosis, and treatment, ultimately improving patient care and outcomes.

1.4 Methodology and objective

One of the factors hindering a structure to be fully loaded and exhibit proper deformation is mechanical instabilities, especially when the structure is compressed. However, the instabilities sometimes occur when the structure is loaded in tension and the existing literature shows the importance of the subject. In practice, a common struggle is to find a critical load, referred to as buckling load, under which the structure exhibits instability. These instabilities can be the results of material non-linearity, bulging bifurcation, bending bifurcation, etc. A bifurcation manifests when there's a substantial and abrupt change in a variable, such as displacements, triggered by a slight, smooth increase in the magnitude of a parameter, like internal pressure. Post-bifurcation characterizes the material's response after undergoing bifurcation. To solve such a problem, one has to solve a total non-linear problem.

The traditional approaches, such as those presented in continuum mechanics, adequately address the design requirements of many structures, focusing on instability matters. The foundation of continuum mechanics lies in the mathematical description of Kinematics, which encompasses concepts such as the rigid motion, deformation, displacement, velocity, reference configuration (Lagrangian or undeformed body), and deformed configuration. Subsequently, Balance laws, including the equilibrium of momentum and mass are expressed, often through Partial Differential Equations (PDEs). Finally, material laws are commonly employed to establish the relationship between stresses and strains. There exist various types of material laws in mechanics. The linear elastic material law is suitable for materials experiencing small strains, encompassed by parameters such as the Young's modulus and Poisson's ratio. In contrast, non-linear elastic materials necessitate a coefficient of strain that varies with deformation, apt for materials undergoing significant distortion. Hyperelasticity establishes a distinct constitutive relation between stresses and strain. This relation is irrespective to the loading history and is elucidated through a Strain Energy Density Function, where stresses are derived from derivatives of this function. Analytical analysis serves as a modeling technique. In recent studies, the principles of continuum mechanics and hyperelasticity are employed to establish a balance relationship between the body motions and applied loads. However, certain structural instabilities linked to the propagating instabilities present challenges where the traditional approach fails to account for the bifurcation point (or limit load instability).

The exploration of various bifurcation and post-bifurcation modes holds significant importance in probing diverse structural instabilities. Notably, advancements in this area have been noteworthy, especially concerning cylinders subjected to various boundary conditions, which have seen notable progress in recent years.

1.5 Content

This thesis is structured into six chapters. Chapter 2 focuses on bifurcation in extended and inflated cylindrical tubes, elucidating the bifurcation criterion for membranes. In Chapter 3, we delve into a numerical procedure for analyzing bifurcation phenomena in isotropic solids, employing an invariant-based phenomenological approach. Chapter 4 provides a detailed account of the numerical methodology and ABAQUS implementation of the model, aiming to comprehensively capture the bulging and bending bifurcation of a residually-stressed two-layer cylindrical tube. This work investigates the combined influence of axial loading and internal pressure on the bifurcation and post-bifurcation of double-layered cylindrical tubes and follows these objectives:

1- Investigation on the bifurcation of double-layered cylindrical tubes made of incompressible material under axial load and internal pressure utilizing modified Riks method.

2- Including the residual stresses on the constitutive behavior of the double-layered cylindrical tubes.

3-Investigation for comprehensively capturing the bulging and bending bifurcation phenomena in a residually-stressed cylindrical tube.

Subsequently, bifurcation and stability analyses are conducted for a tube under internal pressure and twist in Chapter 5. Finally, the findings of the research article are summarized in Chapter 6, providing a concise overview of the research outcomes.

Chapter 2

Deformation of bifurcation for extended and inflated cylindrical tubes

2.1 Introduction

In recent years, significant strides have been taken to delve into boundary value problems within the realm of stability theory. This endeavor encompasses a diverse array of loading conditions, geometries, and materials. Bifurcation phenomena have garnered considerable attention from numerous researchers across a multitude of contexts, as evidenced by the extensive references available. While obtaining analytical solutions for this phenomenon proves challenging, their discovery often yields profound insights into the underlying physical phenomena.

The specific focus here pertains to the bulging and bending bifurcation of a tube, for which solutions have been articulated in terms of incremental equations. The methodology directly addresses the equilibrium of distinct infinitesimal volume elements, with the mode of bifurcation guiding the selection of the appropriate differential volume element for consideration. What distinguishes this approach is its reliance on intuitive engineering or physics-based reasoning rather than complex mathematical formalism. As a result, it offers a lucid interpretation of the bifurcation analysis, facilitating a deeper understanding of the underlying mechanics. Importantly, the methodology presented herein not only offers theoretical insights but also holds practical relevance, aligning closely with the problem-solving mindset prevalent in engineering and physics disciplines.

The analysis following the bifurcation continues to center on the equilibrium of infinitesimal volume elements, extending its scope to include a comprehensive examination of bifurcation modes. The solution methodology is tailored to non-linearly elastic material models, specifically targeting incompressible models wherein deformation and stress align along principal directions. This approach not only enhances our understanding of the bulging phenomenon but also provides practical implications for predicting and managing instabilities in materials subjected to varying pressure conditions. By delving into the intricacies of bifurcation modes and their implications for instability onset, this study contributes to the broader understanding of

material behavior under complex loading scenarios.

First, we deals with the equations that provide the description of the deformation, geometry, and the boundary value problem at hand within the context of finite deformation theory. Subsequently, concepts and definitions of residually-stressed constitutive model, equilibrium and bifurcation behavior of thick-walled circular cylindrical tubes under different loading conditions are described.

2.2 Basic equations in nonlinear elasticity

Assume that $\boldsymbol{B}_0 \in \boldsymbol{R^3}$ is a fixed continuous reference configuration of the body, while current continuous configuration is denoted as $\boldsymbol{B}_t \in \boldsymbol{R^3}$. The nonlinear deformation mapping describes the mapping of material points $\boldsymbol{X} \in \boldsymbol{B}_0$ onto the current configuration $\boldsymbol{x} \in \boldsymbol{B}_t$ at time t such that:

$$\boldsymbol{x} = \Omega(\boldsymbol{X}, t) \quad ; \quad \text{and} \quad \boldsymbol{X} = \Omega^{-1}(\boldsymbol{x}, t) \tag{2.1}$$

where Ω is a function. The displacement $\boldsymbol{u}$ is $\boldsymbol{u} = \boldsymbol{x} - \boldsymbol{X}$ Accordingly, the deformation gradient denoted by $\boldsymbol{F}$ relates the one-to-one mapping of line vectors from the reference to the current placements by:

$$\boldsymbol{F} = \frac{\partial \Omega(\boldsymbol{x}, t)}{\partial \boldsymbol{X}} = \boldsymbol{I} + \nabla \boldsymbol{u}(\boldsymbol{X}) \tag{2.2}$$

in which $\nabla \boldsymbol{u}(\boldsymbol{X})$ is the displacement gradient tensor. The ratio of the reference to current volume is presented by the determinant of the deformation gradient $\det(\boldsymbol{F}) > 0$; and for the case of non-compressibility $\det(\boldsymbol{F}) = 1$ must be satisfied. The symmetric and positive definite right Cauchy–Green tensor is given by $\boldsymbol{C} : \boldsymbol{F}^T \boldsymbol{F}$.

In order to account for swelling, a swelling parameter v is introduced such that:

$$v = \det(\boldsymbol{F}). \tag{2.3}$$

If $v > 1$ then the material is swollen, and if $0 < v < 1$ then the material is de-swollen.

The mechanical behavior of an isotropic material is often modeled as a function W of the first three principal invariants $I_1(\boldsymbol{C})$, $I_2(\boldsymbol{C})$, and $I_3(\boldsymbol{C})$. For an incompressible swellable material, these three principal invariants of $\boldsymbol{C}$ have the following forms:

$$\begin{aligned} I_1(\boldsymbol{C}) &= \operatorname{tr}(\boldsymbol{C}) \\ I_2(\boldsymbol{C}) &= 0.5\left[(\operatorname{tr}(\boldsymbol{C}))^2 - \operatorname{tr}(\boldsymbol{C}^2)\right] \\ I_3(\boldsymbol{C}) &= v^2 \end{aligned} \tag{2.4}$$

For an isochoric, isotropic material ($\det(\boldsymbol{F}) = 1$) the third invariant reduces to $I_3(\boldsymbol{C}) = 1$. The nominal stress $\boldsymbol{P}$ for an incompressible material is defined as:

$$\boldsymbol{P} = \frac{\partial \Psi_m}{\partial \boldsymbol{F}} - p\boldsymbol{F}^{-1} \tag{2.5}$$

where p is the Lagrange multiplier arising from the incompressibility constraint. The Cauchy stress is:

$$\boldsymbol{\sigma} = \boldsymbol{F}\frac{\partial \Psi_m}{\partial \boldsymbol{F}} - p\boldsymbol{I} \tag{2.6}$$

where I is the identity tensor.

On the other hand, the strain energy density of an incompressible, isotropic, and swelling material is presented in [3, 4] as:

$$W(I_1, I_2, v) = m(v) W_{iso}(v^{-\frac{2}{3}} I_1, v^{-\frac{4}{3}} I_2) \tag{2.7}$$

where $W_{iso}(I_1, I_2)$ is the strain energy density function for an isotropic material without swelling. The term $m(v)$ describes the proportional change in stored energy with swelling [4].

In incompressible and swellable materials, the relation between the Cauchy stress tensor $\boldsymbol{\sigma}$ and the deformation is:

$$\boldsymbol{\sigma} = -p\boldsymbol{I} + \frac{1}{v}\frac{\partial W}{\partial \boldsymbol{F}}\boldsymbol{F}^T. \tag{2.8}$$

Eq. (2.8) satisfies the equilibrium condition div$\boldsymbol{\sigma} = 0$.

2.3 Description of the geometry and the boundary value problem:an inflated and extended tube

Consider an arbitrary undeformed circular cylindrical tube described by:

$$A \leq R \leq B \quad , \quad 0 \leq Z \leq L \quad , \quad 0 \leq \theta \leq 2\pi \tag{2.9}$$

in which R, Z, θ are cylindrical coordinates of tube identifying the inner and outer radii by A and B, respectively, and L stands for the length. The thickness of tube is denoted as $T = B - A$. The position vector of a material point is accordingly represented as follows:

$$X = R\, e_R(\theta) + Z\, e_Z \tag{2.10}$$

where e_R, e_Z and e_θ are unit vectors in the indicated directions. The cylinder is extended (applying uniform stretch along the z-direction λ_Z) and inflated, with uniform inflation pressure P in such a way that the deformed configuration the cylinder is described as:

$$x = r\, e_r(\theta) + z\, e_z \quad ; \quad a \leq r \leq b \quad , \quad 0 \leq z \leq l \quad , \quad 0 \leq \theta \leq 2\pi \tag{2.11}$$

in which (r, θ, z) are cylindrical polar coordinates and e_r, e_z, e_θ are unit vectors in the deformed configuration, while the deformed length of the cylinder is identified by l. Referring to the cylindrical coordinate system, the associated deformation gradient tensor $\boldsymbol{F}$ can be represented as diag $(\lambda_r, \lambda_\theta, \lambda_Z)$ where the principal radial stretch for an incompressible material $(v = 1)$

follows the relation$\lambda_r = \lambda_\theta^{-1}\lambda_z^{-1}$, and the azimuthal principal stretch is $\lambda_\theta = \dfrac{r}{R} > 0$ and the axial stretch is $\lambda_Z = \dfrac{l}{L}$.

We consider materials for which the principal axes of stress and strain coincide. In particular, in this section, we consider the material body to be composed of an in-compressible isotropic hyperelastic material, the mechanical behavior of which is described in by a strain-energy function $\Psi_m = \Psi_m(\boldsymbol{F})$ per unit initial configuration.

in which μ is the shear modulus of the material. The local equilibrium equations must comply with the following:

$$\mathrm{Div}\boldsymbol{P} = 0 \quad , \quad \mathrm{div}\boldsymbol{\sigma} = 0, \tag{2.12}$$

where Div is the divergence with respect the reference configuration while div is the divergence with respect to the deformed configuration. In what follows, we give motivation for the analysis of bifurcation.

2.4 Solution of the boundary value problem

By considering a uniform axial stretch, the deformation is expressed as:

$$r = f(R) = \sqrt{[a^2 + \lambda_z^{-1}(R^2 - A^2)]} \tag{2.13}$$

To illustrate, consider the mechanical response of a body according to a standard neo-Hookean material law, whose strain energy function can be expressed as [5, 6]:

$$\Psi_m = \frac{\mu}{2}\left(\lambda_r^2 + \lambda_\theta^2 + \lambda_z^2 - 3\right) \tag{2.14}$$

For the material at hand, the uniform internal pressure P for the assumed boundary conditions is:

$$P = \int_{\lambda_a}^{\lambda_B} \frac{\left(\frac{\partial \psi_m}{\partial \lambda_\theta}\right)}{1 - \lambda_\theta^2\lambda_z} d\lambda_\theta = \mu\left[\frac{1}{2\lambda_\theta^2\lambda_z^2} - \frac{1}{\lambda_z}\ln\lambda_\theta\right] \quad , \quad \lambda_a = \frac{a}{A} \quad ; \quad \lambda_b = \frac{b}{B} \tag{2.15}$$

Utilizing the above relation, the internal pressure P can be regarded as a function of λ_z and λ_b. Fig. 2.1 shows the normalized pressure as a function of the stretchλ_b for thickness ratios defined as $\eta = \frac{T}{A}$, assuming that the axial stretch λ_z is taken to be one.

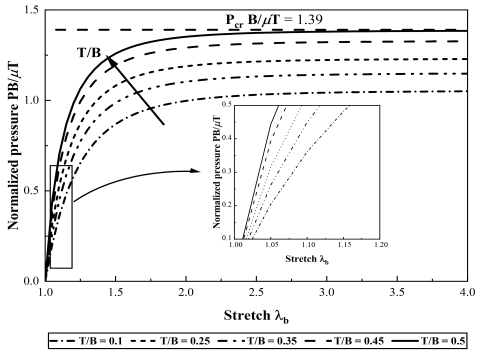

Figure 2.1: Variation of the applied pressure on the stretch λ_b. The legend shows the value of thickness ratio $\eta = \frac{T}{B}$, whereas the arrow indicates the increasing value of η.

The asymptotic value of pressure can be obtained and yields:

$$\frac{P_{cr}}{\mu} = \frac{1}{\lambda_z} \ln\left(\frac{B}{A}\right). \tag{2.16}$$

An asymptotic curve ($\lambda_b \propto \infty$) corresponding to the critical pressure $\frac{P_{cr}}{\mu}$ is shown as (dashed line) for $\eta = 0.5$. Alternatively, one can imagine the asymptotic curve of $\frac{P_{cr}}{\mu}$ vs. λ_z for a fixed value of B/A. This particular scenario indicates possible loss of stability with no pressure maximum. This example serves us to introduce the instabilities at hand. Once the tube is being inflated, at a particular deformation the tube losses its perfect cylindrical shape, i.e. it bifurcates. In the next section we introduce these possible bifurcations for the problem at hand.

2.5 Bifurcation of tubes

To assess the bifurcation of the inflated tubes, one considers the increments of displacements in the form of:

$$\delta \boldsymbol{u} = \delta u_z(r,\theta,z)e_z + \delta u_r(r,\theta,z)e_r + \delta u_\theta(r,\theta,z)e_\theta \tag{2.17}$$

Bifurcation are categorized in three modes: 1) the prismatic form, in which the increments of displacement are independent of the longitudinal movements, 2) the bulging form, which assumes that $\delta \boldsymbol{u}$ is independent of θ, leading to a axisymmetric displacement retaining the circular shape of the cross-section. 3) the bending mode, also called the composite form, which is a general case with no assumptions interpreted as the combination of bulging and prismatic modes, see Fig. 2.2.

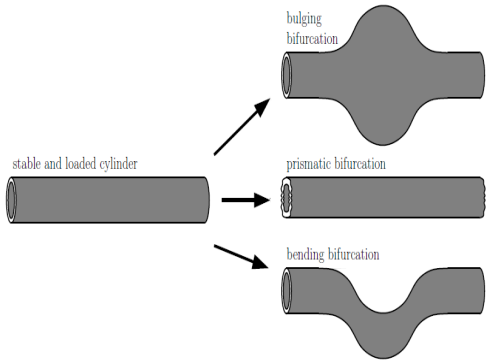

Figure 2.2: Three different bifurcation modes, bulging, prismatic, and bending

2.5.1 Bulging bifurcation

Several studies addressed the bulging bifurcation [7–9]. We just give here main equations for incompressible materials and the membrane case. In order to investigate the bulging bifurcation of a cylinder, one considers incremental displacements Eq. (2.17) in the form:

$$\delta \boldsymbol{u} = \delta u_z(r,z)e_z + \delta u_r(r,z)e_r \tag{2.18}$$

which is independent of θ and δu_θ. For a membrane there is no dependance on r. Furthermore, consider that $W = W(\lambda_r, \lambda_\theta, \lambda_z)$ is the strain energy function. This includes isotropic materials as well as orthotropic materials with the axes of orthotropy coinciding with the principal axes of stress. In the latter case, one could think of a material with two preferred directions which are mechanically equivalent and are symmetrically disposed. Introducing the notation $\hat{W}(\lambda_\theta, \lambda_z) = W(\lambda_\theta^{-1}\lambda_z^{-1}, \lambda_\theta, \lambda_z)$, It can be obtained that the bifuration condition for a cylinder made of a material with an enrgy function W, with with radius R and length L [1] is:

$$f\left(\hat{W}, \lambda_\theta, \lambda_z\right) + \left(\frac{2\pi R}{L}\right)^2 \lambda_\theta^2 \lambda_z \hat{W}_{\lambda_z} \hat{W}_{\lambda_z\lambda_z} = 0 \tag{2.19}$$

in which:

$$f\left(\hat{W}, \lambda_\theta, \lambda_z\right) = \lambda_z^2 \hat{W}_{\lambda_z\lambda_z}\left(\lambda_\theta^2 \hat{W}_{\lambda_\theta\lambda_\theta} - \lambda_\theta \hat{W}_{\lambda_\theta}\right) - \left(\lambda_\theta \lambda_z \hat{W}_{\lambda_\theta\lambda_z} - \lambda_\theta \hat{W}_{\lambda_\theta}\right)^2. \tag{2.20}$$

This latter equation is used as a guide in the case of thick-walled tubes. Furthermore, it can be shown that it is also the bulging bifurcation condition for swellable (incompressible) materials. Fig. 2.3 depicts the bulging bifurcation of a cylinder.

2.5.2 Prismatic bifurcation

In the prismatic mode, the cylinder's section deforms into a prismatic, non-circular shape. In this case, Eq. (2.17) becomes:

$$4\delta \boldsymbol{u} = \delta u_r(r,\theta)e_r + \delta u_\theta(r,\theta)e_\theta \tag{2.21}$$

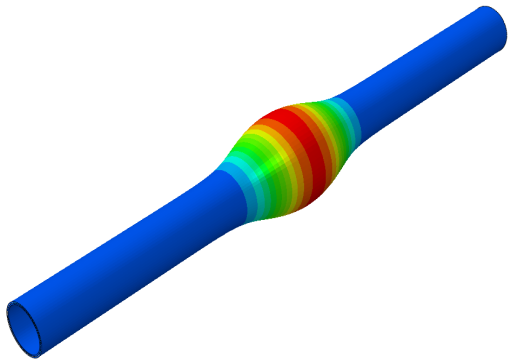

Figure 2.3: Bulging bifurcation mode of a cylinder

For a membrane there is no dependance on r. it follows that the onset of bifurcation is given by

$$\hat{W}_{\lambda_\theta \lambda_\theta} = 0. \tag{2.22}$$

Furthermore, it can be shown that this equation is also the prismatic bifurcation for swellable (incompressible) materials.

2.5.3 Bending bifurcation

In the realm of venous tortuosity within blood vessels, such as retinal arteries and veins, it is common for them to adopt a tortuous path. This phenomenon is often associated with conditions like hypertension, diabetes, and retinopathy [10, 11]. Research indicates that the reduction of axial extension in arteries can contribute to their development of a tortuous shape, altering their originally circular cylindrical geometry [12]. Additionally, certain arteries, such as the superficial femoral artery, undergo considerable bending, necessitating specialized stent designs to accommodate these large bending deformations. The presence of significant bending in arteries may also give rise to saccular aneurysms. Therefore, it is crucial to investigate various factors linked to arterial bending [13]. The upcoming chapter will delve into the concept of bending instability, emphasizing its mathematical formulation and providing valuable insights into this phenomenon

Assuming a perfect circular cylindrical membrane under internal pressure and axial loading, see [1], the bending mode may occur according to Fig. 2.4. It would be reasonable to anticipate that an increase in λ_z corresponds to an increase in axial load (N). This relationship is demonstrated by [14], where it is observed that $N = 0$ when $\lambda_\theta \lambda_z^2 = 1$, indicating that inflation results in axial shortening in the absence of axial constraint; thus, $\lambda_\theta > 1$ implies $\lambda_z < 1$. Consequently, to maintain $\lambda_z = 1$ during inflation, $N > 0$, implying that if both ends of the cylinder are fixed, inflation would induce axial load. Bifurcation associated with the bending mode is depicted in [15]. The cylinder axis experiences virtual radial displacement δu_r^0. The equilibrium of moments can be expressed as:

$$M = N\delta u_r^0 - p\pi r^2 \delta u_r^0 \tag{2.23}$$

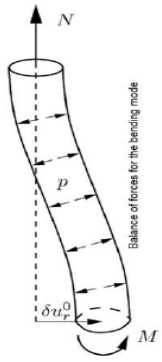

Figure 2.4: Bending bifurcation mode of a cylinder [1]

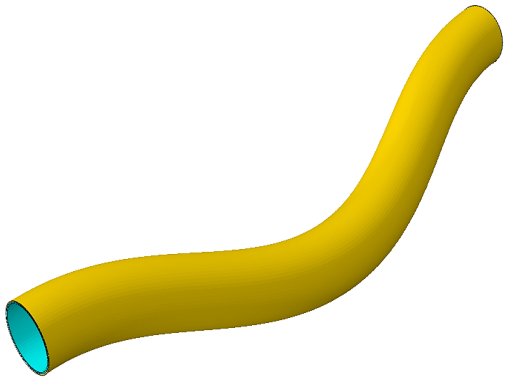

Figure 2.5: The beginning of bending bifurcation of a cylinder

in which M is the resultant moment. $N\delta u_r^0$ is related to moment caused by axial load and $p\pi r^2\delta u_r^0$ is related to the moment caused by inflation. . Moreover, the axial load and internal pressure can be interpreted as $N = 2\pi rh\sigma_{zz}$ and $p = \frac{h\sigma_{\theta\theta}}{r}$, respectively [15].Stable equilibrium can be achieved by $M = 0$. Therefor, Eq. (2.23) can be re-written as:

$$\sigma_{\theta\theta} = 2\sigma_{zz} \tag{2.24}$$

In the case of tube with a thickness,in this work, average values of σ_{zz} and $\sigma_{\theta\theta}$ across the thickness are used [9]. Concretely, the unstable state of bending bifurcation starts with $\sigma_{\theta\theta} > 2\sigma_{zz}$, see Fig. 2.5. Furthermore, it can be shown that this equation is also the bending bifurcation for swellable (incompressible) materials.

Chapter 3

Bifurcation of an inflated and extended isotropic tube

3.1 Introduction

Inflated tubes may face various types of bifurcation modes, which result from factors such as geometry, properties of the materials, and loading types. For instance, during the last decades, numerous theoretical and experimental works [1, 7, 8, 15–49] study the formation of instabilities as a result of both the internal pressure of the cylinders and axial loading. While bulging bifurcation has received some substantial attention, the same is not true for bending and prismatic bifurcation modes. For prismatic bifurcation to occur, a sufficient condition is a maximum in the curve giving values of the stress component in the azimuthal direction vs azimuthal stretch [15]. Bifurcation analyses that apply small deformations which are superimposed on a finite deformation have been presented for both thin-walled [15] and thick-walled tubes [15]. Prismatic bifurcation and bending bifurcation have been investigated in the modeling of arterial tissue in order to understand the consequences of *Marfan's syndrome*, a connective tissue disorder, in which the affected arterial wall shows a weakening behavior [50–52, 52–65]. The influence of residual stresses on the bifurcation of the cylinder has been studied in [66–68].

Many articles on the bifurcation of tubular structures focus on a single bifurcation mode, often neglecting that the onset of a certain bifurcation mode may have higher relevance than another (see, e.g., Font et al. [9] and Topol et al. [69]). This chapter studies the occurrence of three bifurcation modes in the inflated and axially loaded tubes, namely bulging bifurcation, prismatic bifurcation, and bending bifurcation. The bulk of articles on the bifurcation of cylinders focuses on volume-preserving problems. Yet in biological soft tissues, edema, mechanical trauma, and inflammations [70–72] and further factors may lead to swelling of the material. Swelling processes in hyperelastic materials have been taken into account in works such as [73, 74]. The changes in both the cylinder geometry and the elastic properties due to swelling will affect the bifurcation characteristics. Such a swelling effect has been studied in [75–77] for bulging bifurcation of fibrous materials, and in most cases, the isotropic constituent has been taken to be a neo-Hookean or Mooney-Rivlin type of material [78]. The

study of fibrous material is often inspired by the composition of arterial soft tissue, in which multiple collagen fiber families reinforce a ground substance material [79].

Motivated by the restriction of swellable materials to modifications of neo-Hookean or Mooney-Rivlin types of material in articles on bifurcation analysis, this chapter focuses on an isotropic material that combines the neo-Hookean material with the Demiray model [80]. The latter model has an exponential form, and such types of models found their use in soft tissue modeling for several decades [81]. Such a material that combines the neo-Hookean with the Demiray model has been studied in [82] for bulging in a volume-preserving context. This work modifies this material model in order to account for swelling, and, accordingly, it compares in both scenarios (volume-preserving and not volume-preserving) the occurrence of bulging bifurcation, prismatic bifurcation, and bending bifurcation. This chapter shows that despite its restriction to isotropic material behavior without fibrous constituents, the initiation and competition of the relevant instability modes can be quite complex with a dependence on various factors that include the specification of the material constituents in our material model, the geometry of the considered problem, and the amount of swelling.

3.2 Inflation of an Isotropic Tube

3.2.1 Geometry of the Inflated Tube

We consider a hyperelastic tube, which is subjected to an inner pressure and an axial stretch. We continue using the same notation. Therefore, the unloaded configuration is taken to be the reference configuration or natural configuration $\mathcal{B}_r$ for the tube. In terms of cylindrical coordinates (R, Θ, Z), the geometry of the unloaded tube is

$$A \leq R \leq B, \qquad 0 \leq \Theta \leq 2\pi, \qquad -L/2 \leq Z \leq L/2, \tag{3.1}$$

where A is the inner radius, B is the outer radius, and L is the length. Any point of this undeformed cylinder can be described by the position vector $\boldsymbol{X} = R\boldsymbol{E}_R(\Theta) + Z\boldsymbol{E}_Z$ where $\{\boldsymbol{E}_R, \boldsymbol{E}_\Theta, \boldsymbol{E}_Z\}$ are the base unit vectors of the undeformed configuration. In the deformed configuration $\mathcal{B}$, the geometry of the tube is described in terms of the cylindrical coordinates (r, θ, z),

$$a \leq r \leq b, \qquad 0 \leq \theta \leq 2\pi, \qquad -\ell/2 \leq z \leq \ell/2, \tag{3.2}$$

where a is the inner radius, b is the outer radius, and ℓ is the deformed length. Any point of this cylinder can be described by the position vector $\boldsymbol{x} = r\boldsymbol{e}_r(\Theta) + z\boldsymbol{e}_z$, where $\{\boldsymbol{e}_r, \boldsymbol{e}_\theta, \boldsymbol{e}_z\}$ are the base unit vectors of the deformed configuration. The displacement $\boldsymbol{u}$ is given by $\boldsymbol{u} = \boldsymbol{x} - \boldsymbol{X}$.

A compressible (non-swelling) material that depends on the invariants I_1, I_2, and I_3 could also be modified so as to include volume-changing effects that result from both the compressible nature of the material and swelling [83]. The term $m(v)$ describes the proportional change in stored energy as the swelling field v varies [84]. This function $m(v)$ is positive, and it obeys $m(1) = 1$. A standard form for m is (see, e.g., Gou et al. [85])

$$m(v) = v^q, \tag{3.3}$$

which we also apply in this research, where q is a positive constant. For W_{iso} we apply a combination of the neo-Hookean model and the Demiray model [80] in the form (see Alhayani et al. [82])

$$W_{\text{iso}}(I_1) = \frac{\mu}{2\left[1-k+k\alpha\right]}\left\{\left[1-k\right]I_1 + k\exp\left(\alpha\left[I_1-3\right]\right) + 2k - 3\right\}, \qquad 0 \leq k \leq 1, \tag{3.4}$$

which just depends on the first invariant $I_1(\boldsymbol{C})$. The parameter $k \in [0,1]$ quantifies to which degree the function W_{iso} reveals neo-Hookean or Demiray characteristics. If $k = 0$, then the material shows purely neo-Hookean behavior,

$$W_{\text{iso}}(I_1)|_{k=0} = \frac{\mu}{2}\left[I_1 - 3\right], \tag{3.5}$$

in which μ is the shear modulus. Different works such as [86] have shown that despite its relatively simple form, a neo-Hookean strain energy form may be sufficient to describe the mechanical behavior of an elastinous ground substance in biological soft tissue. If $k = 1$, then the ground substance shows a purely Demiray behavior,

$$W_{\text{iso}}(I_1)|_{k=1} = \frac{\mu}{2\alpha}\left\{\exp\left(\alpha\left[I_1-3\right]\right) - 1\right\}, \tag{3.6}$$

in which α is a dimensionless parameter, which is usually taken to be positive.

Notice that in the limit $\alpha \to 0$ the Demiray model (3.6) shows a neo-Hookean behavior (3.5),

$$\lim_{\alpha\to 0}\left[W_{\text{iso}}(I_1)|_{k=1}\right] = W_{\text{iso}}(I_1)|_{k=0}\,. \tag{3.7}$$

After the substitution of (3.3) and (3.4) into (2.7), we obtain a swellable version of (3.4),

$$W(I_1, v) = \frac{\mu v^q}{2\left[1-k+k\alpha\right]}\left\{\left[1-k\right]\frac{I_1}{v^{\frac{2}{3}}} + k\exp\left(\alpha\left[\frac{I_1}{v^{\frac{2}{3}}} - 3\right]\right) + 2k - 3\right\}, \quad 0 \leq k \leq 1. \tag{3.8}$$

In (3.8), the term μv^q can be interpreted as a swelling-dependent shear modulus. If $q < 2/3$, then the ground substance stiffness decreases with increasing values for v; if $q = 2/3$, then μ describes the swelling-independent shear modulus; if $q > 2/3$, then the ground substance stiffness increases with increasing values for v. Analogous to (3.7), we obtain

$$\lim_{\alpha\to 0}\left[W(I_1, v)|_{k=1}\right] = W(I_1, v)|_{k=0}\,. \tag{3.9}$$

Special cases of $W(I_1, v)$ in (3.9) have been considered in different articles. For example, the works by Topol et al [87] apply (3.8) for $k = 0$, which results into a swellable neo-Hookean material that is sometimes referred to as the Treloar model [88]. A modification of a nearly in-compressible behavior has been applied in the numerical cervical soft tissue studied by Gou et al. [85]. Further models exist that account for swelling. For example, Zamani et al. [89] apply a swellable version of the Gent model, that accounts for the limited extensibility of the material. Incompressible swellable models that depend on the first two invariants I_1 and I_2 of $\boldsymbol{C}$ have also been applied in different works. For example, Zamani et al. [89] and Topol et al. [78] apply a swellable version of the Mooney-Rivlin material.

Soft tissue may reveal an anisotropic behavior due to fibers, which are embedded in the ground substance. It has been suggested that swelling may mediate remodeling processes in embedded fibers [85, 87]. Nevertheless, due to the complex bifurcation response of the isotropic ground substance itself, especially in the context of swelling, the contribution of fibers is ignored in this research.

While our work follows the approach in [73, 90] in order to describe swelling, there exist other approaches, for example, those that apply the Donnan osmosis in the framework of the theory of porous media [91–93].

In in-compressible and swellable materials, the relation between the Cauchy stress tensor $\boldsymbol{\sigma}$ and the deformation can be expressed in the form (see, e.g. [83] for details):

$$\boldsymbol{\sigma} = -p\boldsymbol{I} + \frac{1}{v}\frac{\partial W}{\partial \boldsymbol{F}}\boldsymbol{F}^{\mathrm{T}}, \tag{3.10}$$

where p is a scalar that results from the in-compressibility constraint and $\boldsymbol{I}$ is the second order identity tensor. Equation (3.10) must satisfy the equilibrium condition $\mathrm{div}\boldsymbol{\sigma} = \boldsymbol{0}$.

We consider a thin-walled tube, where $H \ll [B - A]$ is the wall thickness, which is taken to be much smaller than the radius R of the tube, $H \ll R$. In this membrane treatment, the radial normal Cauchy stress component in (3.10) is negligible and the azimuthal and axial normal stresses take the forms [32, 94]

$$\sigma_{\theta\theta} = \frac{\lambda_\theta}{v}\frac{\partial \hat{W}}{\partial \lambda_\theta}, \qquad \sigma_{zz} = \frac{\lambda_z}{v}\frac{\partial \hat{W}}{\partial \lambda_z}, \tag{3.11}$$

respectively, where for convenience, we have applied the change of variables $\hat{W}(\lambda_\theta, \lambda_z) = W$ in the strain energy density function. Notice that in (3.11) the scalar p has already been eliminated by the condition $\sigma_{rr} = 0$ that results from the membrane approximation of the cylinder geometry. Then the relation between the inflation pressure P, axial normal force N, and the deformation is given by the equations

$$P = \frac{1}{\lambda_\theta \lambda_z}\frac{H}{R}\frac{\partial \hat{W}}{\partial \lambda_\theta}, \qquad N = \frac{\partial \hat{W}}{\partial \lambda_z}, \tag{3.12}$$

which have been presented, for example, in [16, 95]. In our considerations, the axial stretch λ_z and the swelling v are taken to be constant throughout the application of the inner pressure P, i.e., we assume that the axial stretch and any material volume changes have been applied prior to the pressurization. In this purely elastic modeling without any time-dependent effects in the material behavior, the development of the pressure-inflation relationship is solely due to a change in the pressure.

3.3 Bifurcation Modes of the Isotropic Membrane

It has been shown in various experiments and numerical studies that inflated cylinders may face different forms of instabilities, namely, bulging bifurcation, prismatic bifurcation, and bending bifurcation.

3.3.1 Bulging Bifurcation

For the swellable and isotropic strain energy density form (3.8), the function $f(\hat{W},\lambda,\lambda_z)$ in (2.20) takes the form:

$$\begin{aligned} f &= -\mu^2 v^{2q}\left\{\left(\lambda_\theta \frac{[A(k-1)-AE\alpha k]}{v^{\frac{2}{3}}(2\alpha k-2k+2)}\right.\right. \\ &\quad \left.+\frac{\lambda_\theta\lambda_z}{2\alpha k-2k+2}\left[\frac{ACE\alpha^2 k}{v^{\frac{4}{3}}}-\frac{4v^{\frac{4}{3}}(k-1)}{\lambda_\theta^3\lambda_z^3}+\frac{(4E\alpha k v^{\frac{4}{3}})}{(\lambda_\theta^3\lambda_z^3)}\right]\right)^2 \\ &\quad -\left\{\lambda_z^2\left[\left(\frac{A^2E\alpha^2k}{v^{\frac{4}{3}}}-\frac{B(k-1)}{v^{\frac{2}{3}}}+\frac{BE\alpha k}{v^{\frac{2}{3}}}\right)\frac{\lambda_\theta^2}{2\alpha k-2k+2}\right.\right. \\ &\quad \left.+\left(\frac{A(k-1)}{v^{\frac{2}{3}}}-\frac{AE\alpha k}{v^{\frac{2}{3}}}\right)\frac{\lambda_\theta}{2\alpha k-2k+2}\right] \\ &\quad \left.\times\left(\frac{C^2E\alpha^2k}{v^{\frac{4}{3}}}-\frac{D(k-1)}{v^{\frac{2}{3}}}+\frac{DE\alpha k}{v^{\frac{2}{3}}}\right)\right\}\frac{1}{2\alpha k-2k+2}\Bigg\}, \end{aligned} \tag{3.13}$$

where we have used the abbreviations

$$\begin{aligned} A &= 2\lambda_\theta-\frac{2v^2}{\lambda_\theta^3\lambda_z^2}, & B &= \frac{6v^2}{\lambda_\theta^4\lambda_z^2}+2, \\ C &= 2\lambda_z-\frac{2v^2}{\lambda_\theta^2\lambda_z^3}, & D &= \frac{6v^2}{\lambda_\theta^2\lambda_z^4}+2, \\ E &= \exp\left(\alpha\left[\frac{I_1}{v^{\frac{2}{3}}}-3\right]\right). \end{aligned} \tag{3.14}$$

Bulging bifurcation of the neo-Hookean membrane

For $k=0$, the strain energy density function W takes the neo-Hookean form, for which the bulging condition function becomes:

$$f=\frac{\left[\mu v^{q-2/3}\right]^2(-\lambda_z^4\lambda_\theta^8+4\lambda_z^4\lambda_\theta^2v^2+6\lambda_z^2\lambda_\theta^4v^2+3v^4)}{(\lambda_z^4\lambda^4)}. \tag{3.15}$$

From (3.15) one can conclude that the inflation of a swellable neo-Hookean membrane remains stable to bulging bifurcation under the condition

$$4\lambda_z^4\lambda_\theta^2v^2+6\lambda_z^2\lambda_\theta^4v^2+3v^4>\lambda_z^4\lambda_\theta^8. \tag{3.16}$$

Notice that all terms that depend on v have been collected in the left side. By considering the role of swelling on bulging bifurcation, we conclude from (3.16) that swelling ($v>1$) tends to stabilize a neo-Hookean membrane, whereas deswelling ($0<v<1$) together with larger values of the azimuthal stretch λ_θ tend to trigger bulging.

Swellable neo-Hookean membranes have been extensively studied for bulging bifurcation, and we refer to [75–78] that treat this type of material with and without fiber reinforcement.

Bulging bifurcation of the Demiray membrane

Contrary to the neo-Hookean treatment, the Demiray model has not been applied in many works that explore bulging bifurcation of isotropic materials. An exception is the article by Alhayani et al. [82,96], which shows that the condition $\alpha \geq \frac{1}{6}$ is necessary for an un-swollen material ($v = 1$) to maintain the stability condition $f > 0$ so that no bulging is expected for $\lambda_z \geq 1$ during inflation.

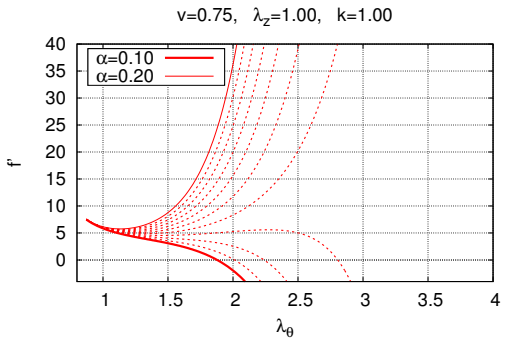

(a)

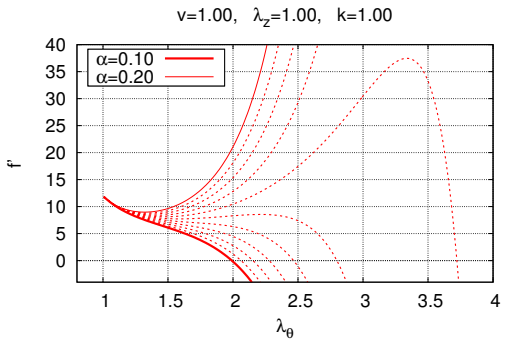

(b)

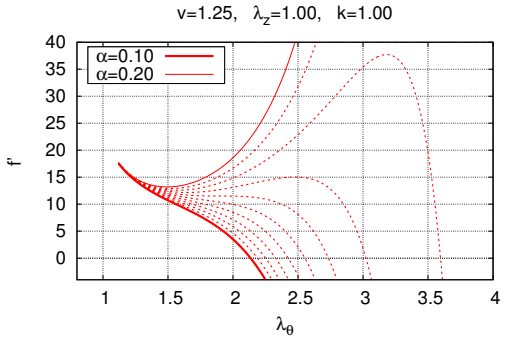

(c)

Figure 3.1: Values of $f' = f/\mu^2$ (f as given by (3.13).) vs λ_θ for the Demiray model ($k = 1$) with $q = \frac{2}{3}$, which provides the sensitivity of this model against bulging. Values $f' = 0$ are associated with the onset of bulging. Panel (a) is for a un-swollen material ($v = 0.75$); panel (b) is for an un-swollen material ($v = 1$); panel (c) is for a swollen material ($v = 1.25$). The thick solid curves correspond to $\alpha = 0.10$, and the thin solid curves to $\alpha = 0.20$. The dotted lines between these curves represent increments of $\Delta\alpha = 0.01$ between $\alpha = 0.10$ and $\alpha = 0.20$. The changes in the azimuthal stretch λ_θ result from the increase in the pressure $P \geq 0$.

For $k = 1$, the bulging condition function for the swellable version of the Demiray model becomes:

$$\begin{aligned} f &= \mu^2 v^{2q} \frac{\exp\left(2\alpha\left[\frac{I_1}{v^{\frac{2}{3}}} - 3\right]\right)}{\lambda_\theta^6 \lambda_z^6 v^2} \Big[(6\alpha\lambda_z^8 - \lambda_z^6 v^{\frac{2}{3}})\lambda_\theta^{10} \\ &\quad + (2\alpha\lambda_z^4 v^2)\lambda_\theta^8 + (6\lambda_z^4 v^{\frac{8}{3}} - 20\alpha\lambda_z^6 v^2)\lambda_\theta^6 \\ &\quad + (4\lambda_z^6 v^{\frac{8}{3}} + 4\alpha\lambda_z^2 v^4 + 8\alpha\lambda_z^8 v^2)\lambda_\theta^4 \\ &\quad + (3\lambda_z^2 v^{\frac{14}{3}} - 2\alpha\lambda_z^4 v^4)\lambda_\theta^2 + 2\alpha v^6\Big], \end{aligned} \tag{3.17}$$

which generalizes the results by Alhayani et al. [82] by including the consideration of volume changes.

From the highest order term of the azimuthal stretch λ_θ in (3.17) we can conclude that for inflation to remain stable throughout the inflation with regards to bulging bifurcation (i.e., $f > 0$) the condition

$$\alpha \geq \frac{1}{6} v^{\frac{2}{3}} \qquad \text{for} \qquad \lambda_z \geq 1 \tag{3.18}$$

has to be fulfilled.

In order to illustrate the effect of swelling and deswelling on the initiation of bulging in the Demiray model in (3.17), we introduce an example in Fig. 3.1. The three panels show for $\lambda_z = 1$ the normalized bulging condition function $f' = f/\mu^2$ vs azimuthal stretch λ_θ for $q = \frac{2}{3}$, taking f in (3.17) for different values of α in the range $0.1 \leq \alpha \leq 0.2$, using increments of $\Delta\alpha = 0.01$. Figure 3.1 (a) is for a de-swollen membrane, taking $v = 0.75$; the cylinder remains stable with respect to bulging($f > 0$) for $\alpha \geq 0.1376$. Fig. 3.1 (b) is for an un-swollen membrane ($v = 1$) that requires $\alpha \geq 0.1\bar{6}$ for the cylinder to remain stable; Fig. 3.1 (c) is for a swollen membrane, taking $v = 1.25$; the cylinder remains stable for $\alpha \geq 0.1934$.

3.3.2 Prismatic Bifurcation

In the prismatic bifurcation mode, the inflated cylinder bifurcates into a prismatic shape with a non-circular cross-section. The bifurcation condition for the lowest (most likely) mode is given by [1]:

$$g \equiv \hat{W}_{\lambda_\theta \lambda_\theta} = 0. \tag{3.19}$$

The membrane remains stable with regards to prismatic bifurcation if g remains positive, and unstable if g becomes negative. This condition has also been derived in [15] and in its follow-up work [15], the study has been extended to thick-walled cylinders. For the strain energy density function, the function g in (3.19) becomes:

$$\begin{aligned} g &= \frac{\mu v^q}{\lambda_\theta^6 \lambda_z^4 v^{\frac{4}{3}}(\alpha k - k + 1)} \Big[(2\alpha^2 v^4 + 2\alpha^2 \lambda_\theta^8 \lambda_z^4 + 3\alpha\lambda_\theta^2 \lambda_z^2 v^{\frac{8}{3}} + \alpha\lambda_\theta^6 \lambda_z^4 v^{\frac{2}{3}} - 4\alpha^2 \lambda_\theta^4 \lambda_z^2 v^2)k \\ &\quad \times \exp\left(\alpha\left[\frac{I_1}{v^{\frac{2}{3}}} - 3\right]\right) + 3\lambda_\theta^2 \lambda_z^2 v^{\frac{8}{3}}(1 - k) + \lambda_\theta^6 \lambda_z^4 v^{\frac{2}{3}}(1 - k)\Big]. \end{aligned} \tag{3.20}$$

Prismatic bifurcation of the neo-Hookean membrane

In the neo-Hookean treatment ($k = 0$) the prismatic bifurcation function becomes:

$$g = \frac{\mu v^q}{\lambda_\theta^6 \lambda_z^4 v^{\frac{4}{3}}} \left[3\lambda_\theta^2 \lambda_z^2 v^{\frac{8}{3}} + \lambda_\theta^6 \lambda_z^4 v^{\frac{2}{3}} \right]. \tag{3.21}$$

The shear modulus μ and the swelling field v are positive, so that (3.21) is zero if

$$3\lambda_\theta^2 \lambda_z^2 v^{\frac{8}{3}} + \lambda_\theta^6 \lambda_z^4 v^{\frac{2}{3}} = 0. \tag{3.22}$$

Condition (3.22) cannot be fulfilled for positive values of the stretches λ_θ, λ_z, $\lambda_\theta > 0$, so that we can conclude that the neo-Hookean cylinder remains stable with regards to prismatic bifurcation. This result has also been obtained, for example, by Al-Chlaihawi et al. [77].

Prismatic bifurcation of the Demiray membrane

In the Demiray treatment ($k = 1$), the prismatic bifurcation function becomes:

$$\begin{aligned} g = & \frac{\mu v^q \exp\left(\alpha \left[\frac{I_1}{v^{\frac{2}{3}}} - 3\right]\right)}{\lambda_\theta^6 \lambda_z^4 v^{\frac{4}{3}} \alpha} \left[2\alpha^2 v^4 + 2\alpha^2 \lambda_\theta^8 \lambda_z^4 \right. \\ & \left. + 3\alpha \lambda_\theta^2 \lambda_z^2 v^{\frac{8}{3}} + \alpha \lambda_\theta^6 \lambda_z^4 v^{\frac{2}{3}} - 4\alpha^2 \lambda_\theta^4 \lambda_z^2 v^2 \right], \end{aligned} \tag{3.23}$$

which is zero if

$$\lambda_\theta^8 + \frac{1}{2}\frac{v^{\frac{2}{3}}}{\alpha}\lambda_\theta^6 - 2\frac{v^2}{\lambda_z^2}\lambda_\theta^4 + \frac{3}{2}\frac{v^{\frac{8}{3}}}{\alpha \lambda_z^2}\lambda_\theta^2 + \frac{v^4}{\lambda_z^4} = 0. \tag{3.24}$$

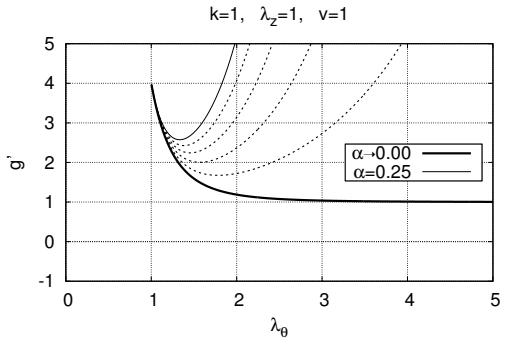

Figure 3.2: Values of the normalized prismatic bifurcation function $g' = g/\mu$ as given by (3.23) vs λ_θ, for $\lambda_z = 1$, $q = \frac{2}{3}$, and $v = 1$. This diagram shows results that, in turn, are associated with values $P \geq 0$ as given by the pressure inflation relation (3.9). The bold curve corresponds to $\alpha \to 0.00$ (neo-Hookean response), and the thin solid curve to $\alpha = 0.25$. The dotted lines between these two curves are associated with increments $\Delta\alpha = 0.05$.

Figure 3.2 depicts normalized values of g, $g' = g/\mu$, as given by (3.17) versus λ_θ for $q = \frac{2}{3}$, $\lambda_z = 1$ and $v = 1$. The values given by the curves obey $P \geq 0$ in the pressure inflation relation

(3.9). The curves remain positive for $\alpha > 0$, and the azimuthal stretch λ_θ takes values that are larger than one. In the limit $\alpha \to 0$, the prismatic bifurcation function (3.23) for the Demiray model approaches the prismatic bifurcation function of the neo-Hookean given in (3.21), and one can conclude that

$$\lim_{\lambda_\theta \to \infty} \left[\lim_{\alpha \to 0} \frac{g}{\mu} \right] = 1. \tag{3.25}$$

It follows that prismatic bifurcation is not feasible for Demiray model. The results from this section show that prismatic bifurcation does not occur for the herein-considered type of loading, and therefore this instability mode will not be further studied in this research (also see the discussion in [69] regarding a neo-Hookean solid).

3.3.3 Bending Bifurcation

It has been shown that the bending bifurcation occurs in the limit when [1],

$$h \equiv \sigma_{\theta\theta} - 2\sigma_{zz} = 0, \tag{3.26}$$

where $\sigma_{\theta\theta}$ and σ_{zz} are the normal Cauchy stresses in azimuthal and axial directions that have been presented in (3.8). If $h < 0$, then the membrane remains stable, whereas for $h > 0$ the membrane is unstable. For the strain energy density function W in (3.10), the function h in (3.26) becomes:

$$h = \mu v^q \frac{(\lambda_\theta^4 \lambda_z^2 - 2\lambda_\theta^2 \lambda_z^4 + v^2)}{\lambda_\theta^2 \lambda_z^2 v^{\frac{5}{3}} (\alpha k - k + 1)} \left(\alpha k \exp\left(\alpha \left[\frac{I_1}{v^{\frac{2}{3}}} - 3 \right] \right) - k + 1 \right). \tag{3.27}$$

Because

$$\begin{aligned} &\alpha k - k + 1 > 0 \qquad \text{and} \\ &\alpha k \exp\left(\alpha \left[\frac{I_1}{v^{\frac{2}{3}}} - 3 \right] \right) - k + 1 > 0 \quad \text{if} \quad \alpha > 0 \end{aligned} \tag{3.28}$$

we can conclude that the bifurcation limit $h = 0$ in (3.27) is obtained when the condition:

$$\lambda_\theta^4 \lambda_z^2 - 2\lambda_\theta^2 \lambda_z^4 + v^2 = 0 \tag{3.29}$$

is fulfilled. This condition (3.29) depends on the azimuthal stretch λ_θ, the axial stretch λ_z and the swelling field v, but it is independent of both α and k. It is interesting to note the following conditions for the onset of bending: if the axial stretch remains constant at $\lambda_z = 1$ and the cylinder inflates ($\lambda_\theta \geq 1$), then the material has to deswell ($0 < v < 1$) to remain stable; while if $\lambda_z > 1$, then the material may also remain stable for slightly swollen materials ($v > 1$).

3.4 Competition between the Onsets of the Different Bifurcation Modes

Articles that treat the bifurcation of inflated cylinders are often devoted to a single instability mode, and they often ignore that a certain type of bifurcation may trigger other bifurcation

modes. Desena-Galarza et al. [97] study the competition of bulging and bending bifurcation in residually stressed tubes under inflation and extension, but swelling effects are not part of that work.

In this section, we consider the isotropic energy density form W in (3.5) that accounts for swelling, and we compare different conditions that trigger the onsets of the different bifurcation modes that have been discussed in Section “Bifurcation Modes of the Isotropic Membrane".

3.4.1 Impact of Swelling on the Occurrence of Bifurcation Modes

We compare the conditions that lead to the onset of bulging bifurcation function $f = 0$ and the bending bifurcation function $h = 0$ for an inflated tube.

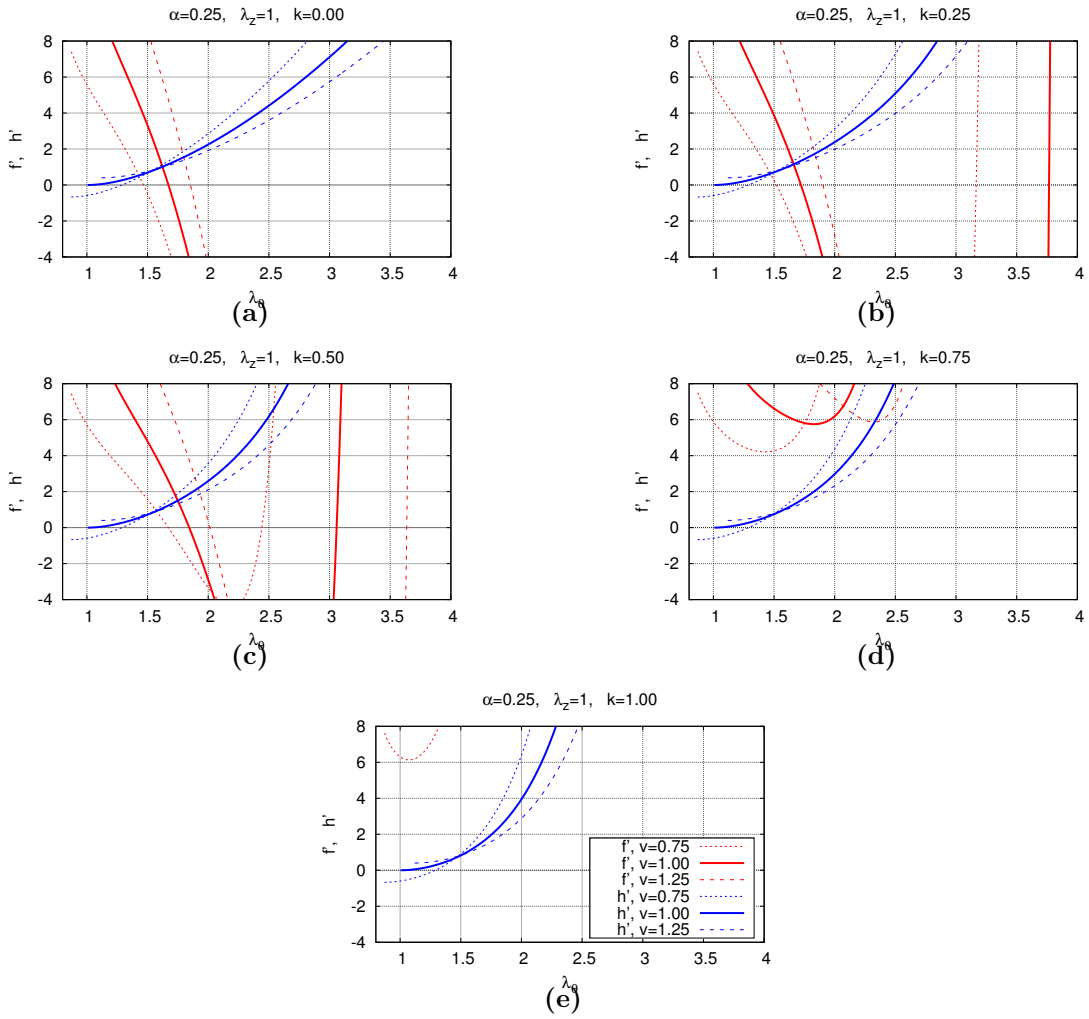

Figure 3.3: Competition between the onsets of the different bifurcation modes. The red curves depict the results for bulging bifurcation function f, where positive values indicate a stable inflation with regards to bulging. The blue curves depict the results for the bending bifurcation function h, where negative values represent stable inflation with respect to bending. Panel (a) is for $k = 0$ (neo-Hookean response); panel (b) is for $k = 0.25$; panel (c) is for $k = 0.50$; panel (d) is for $k = 0.75$; panel (e) is for $k = 1$ (Demiray model). The results are for an axial stretch of $\lambda_z = 1$ and for three values for the swelling parameter v, namely for $v = 0.75$ (deswollen material), for $v = 1$, and for $v = 1.25$ (swollen material). The curves are restricted to values for which the inflation pressure is non-negative, $P \geq 0$, with $\alpha = 0.25$, and $q = 2/3$. The legend in panel (e) applies to all other panels of this figure, too.

Figure 3.3 depicts some results for an inflated tube with $\lambda_z = 1$ and three values of v, namely, $v = 0.75$ (deswollen material), $v = 1$ (unswollen material), and $v = 1.25$ (swollen material). The panels in this figure consider $q = \frac{2}{3}$ and different values for k. As before, we apply the normalizations $f' = \frac{f}{\mu^2}$ and $h' = \frac{h}{\mu}$.Note that the thresholds between stable and unstable inflation, $f = 0$ and $h = 0$, are independent of q for a given v and μ. This scenario would change for other constituents such as fibers, for instance. The results for the different

bifurcation modes can be summarized as follows: There are two values for $f = 0$ in the depicted range for the azimuthal stretch λ_θ. The one associated with the smaller value of λ_θ gives the onset of bulging. With respect to that solution, results show that increasing values for swelling v may shift the bulging bifurcation condition $f = 0$ to larger and potentially less relevant values of the azimuthal stretch λ_θ. This means that swelling may stabilize the tube against bulging bifurcation. The other solution of $f = 0$ just indicates that there are configurations for greater values of λ_θ that are stable with regard to bulging, which means that propagation of this instabilty mode maybe axial (see also [77, 78]). When larger values of k are taken so that the Demiray material characteristics dominate bulging bifurcation will not occur, i.e., the function f is positive. The bending bifurcation function h shows that for swelling ($v \geq 1$) the tube becomes unstable, whereas deswelling ($v < 1$) stabilizes the tube to bending bifurcation. This result has also been obtained for a neo-Hookean material in [69]. This observation can be made for all values of k. If we compare the behavior of the bifurcation functions for increasing values of k so that the Demiray characteristics dominate the elastic behavior, then bending bifurcation for a swollen material ($v > 1$) remains the only relevant instability mode. This observation allows us to pay attention to bending and bulging bifurcation modes only.

3.4.2 Simultaneous Occurrence of Bulging and Bending Bifurcation

Results from the previous section show that swelling stabilizes the material to bulging bifurcation, whereas deswelling stabilizes the material to bending bifurcation. This implies that for certain volume changes both the bulging bifurcation condition $f = 0$ and the bending bifurcation limit $h = 0$ may occur simultaneously at the same instant of the inflation process. This phenomenon will be studied in the present section, where attention is paid to the role of λ_z. Figure 3.4 shows values for the swelling v and the azimuthal stretch λ_θ that fulfill $f = 0$ (bulging bifurcation, red curves) and $h = 0$ (bending bifurcation, blue curves), taking $\alpha = 0.25$, and different values for k. Results are restricted to the smallest value of λ_θ that together with a particular value of swelling v obey $f = 0$. The different panels present the results for different values of the axial stretches. If a red and a blue curve intersect, then $f = h = 0$ so that both bulging and bending occur simultaneously. For $k = 0$ and $k = 0.25$, one can find intersections of red and blue curves, whereas for $k = 0.5$ such intersections do not occur. Note that bending bifurcation $h = 0$ is independent of k. When blue curves are compared in the different panels, one can summarize the following observations regarding stability with regard to bending: Greater values of λ_z are associated with greater values of v for bending to occur. In addition, values of v can be greater than $v = 1$ for values of the axial stretch greater than $\lambda_z = 1$. Greater values of λ_z are associated with greater values of λ_θ for bending to occur. These greater values of λ_θ may have lower relevance for practical applications.

3.4.3 Bulging and Bending Bifurcation for Different values of Axial Stretch and Swelling

In the previous section, the axial stretch λ_z has been held fixed in each example in order to illustrate the impact of swelling on the initiation of the different bifurcation modes.

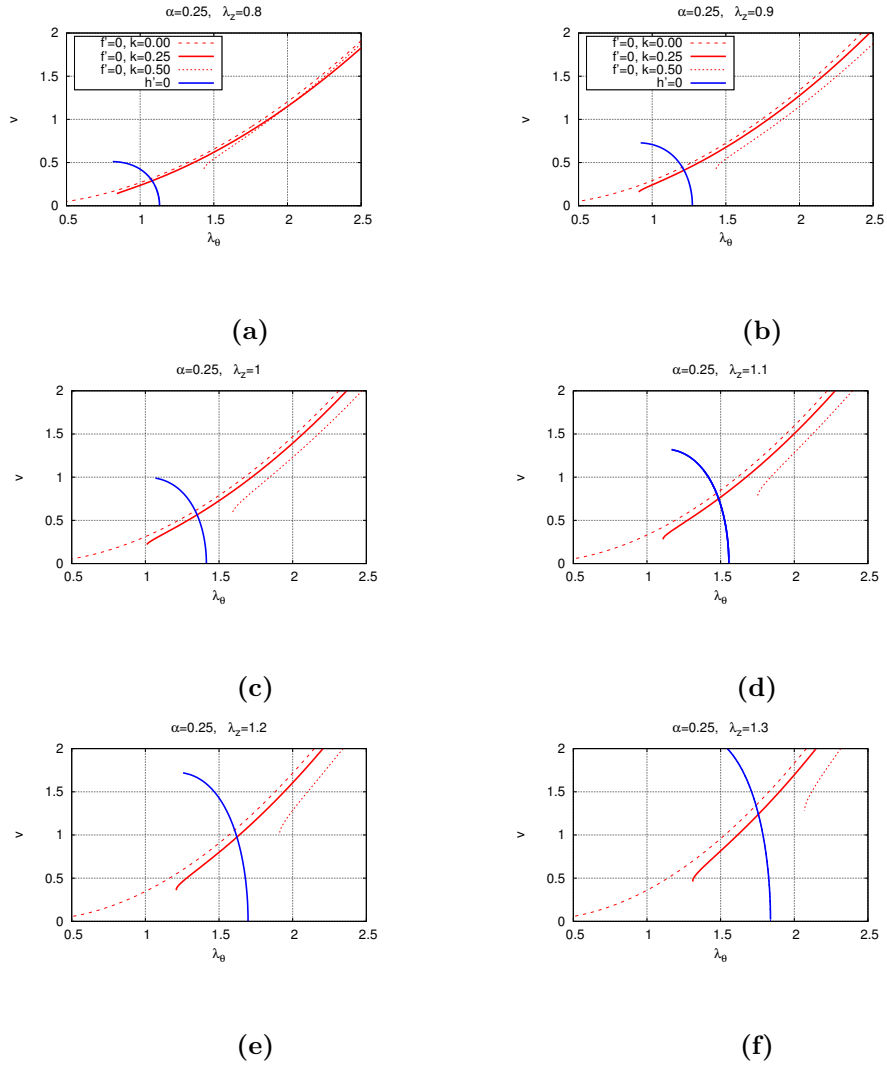

Figure 3.4: Locus of (λ_θ, v) pairs that obey $f = 0$ and $h = 0$ for $\alpha = 0.25$, and different values of k, which in turn obey that $P > 0$. Panel (a) is for $\lambda_z = 0.8$; panel (b) is for $\lambda_z = 0.9$; panel (c) is for $\lambda_z = 1$; panel (d) is for $\lambda_z = 1.1$; panel (e) is for $\lambda_z = 1.2$; panel (f) is for $\lambda_z = 1.3$. Notice that the bending bifurcation limit $h = 0$ is independent from k.

This section explores combinations of values of the azimuthal stretch λ_θ and the axial stretch λ_z for which bulging bifurcation and bending bifurcation are possible for a given value of v. Figure 3.5 depicts λ_z vs. λ_θ for different values of v that fulfill the bulging bifurcation condition $f = 0$ (red curves) and the bending condition $h = 0$ (blue curves). Panel (a) is for $k = 0$ (neo-Hookean response); panel (b) is for $k = 0.25$; while panel (c) is for $k = 0.50$, in all panels with $\alpha = 0.25$. Some red curves for bulging bifurcation, $f = 0$, show that there can be up to two azimuthal stretch values λ_θ that correspond to an axial stretch λ_z in the selected range of the parameter values. The interpretation of this result has been given previously. As it has been shown in (3.29), the bending bifurcation limit $h = 0$ is independent of k, whence, all panels show the same results for $h = 0$. If red and blue curves in the same linestyle intersect, then, both, bulging and bending, occur simultaneously.

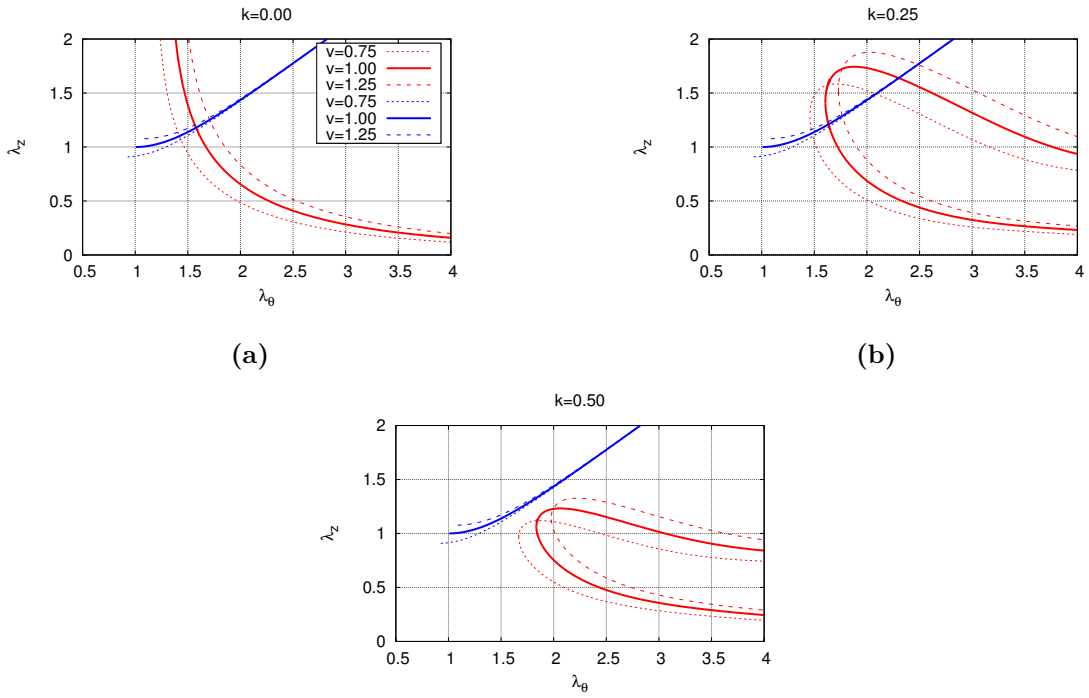

Figure 3.5: Locus of $(\lambda_\theta, \lambda_z)$ pairs that fulfill the bulging bifurcation condition $f = 0$, red curves, and the bending condition $h = 0$, blue curves. Panel (a) is for $k = 0$ (neo-Hookean response); panel (b) is for $k = 0.25$; panel (c) is for $k = 0.50$; in all panels with $\alpha = 0.25$ and for different values of v, among them $v = 0.75$ (deswollen material), $v = 1$, and $v = 1.25$ (swollen) material. Results are restricted to values for which the inflation pressure is non-negative, $P \geq 0$.

For values of k sufficiently large, red and blue curves do not intersect. It follows that bulging and bending do not occur simultaneously.

3.5 Stable Inflation of Pressurized Cylinders

The previous examples have identified different combinations of cylinder deformation and material parameters for which the inflation remains stable with regard to the herein-considered bifurcation modes. Nevertheless, different scenarios can be viewed and just a few examples can be: (a) a cylinder may have been subjected to an increasing inner pressure while all other parameters remain constant; (b) the material parameters may be changed due to remodeling processes in the material; (c) the cylinder may have been subjected to swelling; (d) a combination of these phenomena may occur, for example, during remodeling processes inside a mechano-sensitive material (see, e.g. Topol et al. [98]) or in swelling-regulated processes (see, e.g. Gou et al. [85, 87]).

In this section, we consider inflation of a swollen (or deswollen) cylinder, in which the change in the material volume has taken place before pressurization is considered. The

different examples illustrate how changes in the specifications for the material parameters and swelling may affect either bulging or bending as the relevant bifurcation mode that disrupts the stable inflation. The role of the axial stretch in the pressure-inflation relation is illustrated for $\lambda_z = 1$ and $\lambda_z = 1.1$.

3.5.1 Stable Inflation for $\lambda_z = 1$

Figure 3.6 depicts the relation between (normalized) inflation pressure P and azimuthal stretch λ_θ, for $\lambda_z = 1$, $q = 2/3$, and $\alpha = 0.25$. Each curve in each panel is for a given value of v, which is $v = 0.05$ (most left curves) and $v = 0.95$ (most right curves), and in between with increments $\Delta v = 0.05$. A red curve indicates that the stable inflation is interrupted by bulging bifurcation, whereas a blue curve indicates that the stable inflation is interrupted by bending bifurcation. The values of k are selected to illustrate the sensitivity of bifurcation to slight changes in the material constitutive parameters. Panel (a) is for $k = 0.0$ (neo-Hookean response), and it shows that for small values of swelling the inflation process is interrupted by bulging bifurcation, whereas for larger values of v it is likely that bending occurs. For $k = 0.1$, $k = 0.2$, and $k = 0.3$ in the panels (b)-(d), bending bifurcation occurs at the smaller and greater values of v, whereas for values of v in between bulging bifurcation occurs. For sufficiently large values of k bending bifurcation is the relevant instability mode. This is in agreement with Fig. 3.3.

3.5.2 Stable Inflation for $\lambda_z = 1.1$

Figure 3.7 depicts the relation between (normalized) inflation pressure P and azimuthal stretch λ_θ, for $\lambda_z = 1.1$, $q = 2/3$, and $\alpha = 0.25$. Again, a red curve illustrates that stable inflation is interrupted by bulging bifurcation and a blue curve indicates that stable inflation is interrupted by bending bifurcation. One can note some differences between the results shown in Fig. 3.6 and the ones given in Figure 3.7. For $\lambda_z = 1.1$, the inflation can be stable with regard to bending and bulging for a swollen material ($v > 1$), as opposed to the situation in which $\lambda_z = 1$. In particular, this is shown with different curves of v, which we remind is in the range of $v = 0.05$ (most left curves) and $v = 1.30$ (most right curves), with increments of $\Delta v = 0.05$ between the different curves. The curve for the unswollen material $v = 1$ is highlighted by the use of a dashed linestyle. In addition, in Fig. 3.7, the curves are associated with larger values of λ_θ than the ones shown in Fig. 3.6, i.e. a stable inflation can take larger values of λ_θ for $\lambda_z = 1.1$.A closer look at both Fig. 3.6 and Fig. 3.7 allows to establishing the following:

In Fig. 3.7 (c) the (first four) curves for $v = 0.05$, $v = 0.1$, $v = 0.15$, and $v = 0.2$ are interrupted by bending before bulging becomes the relevant instability mode while in Fig. 3.6 (c), the (first three) curves for $v = 0.05$, $v = 0.1$, and $v = 0.15$ are interrupted by bending. In Fig. 3.7 (c) for sufficiently large values of v the stable inflation is again disrupted by bending bifurcation. In Fig. 3.7 (c), the swelling field may take values that are larger than $v = 1$ during a stable inflation, whereas in Fig. 3.6 a stable inflation is just possible for a deswollen material ($0 < v < 1$).

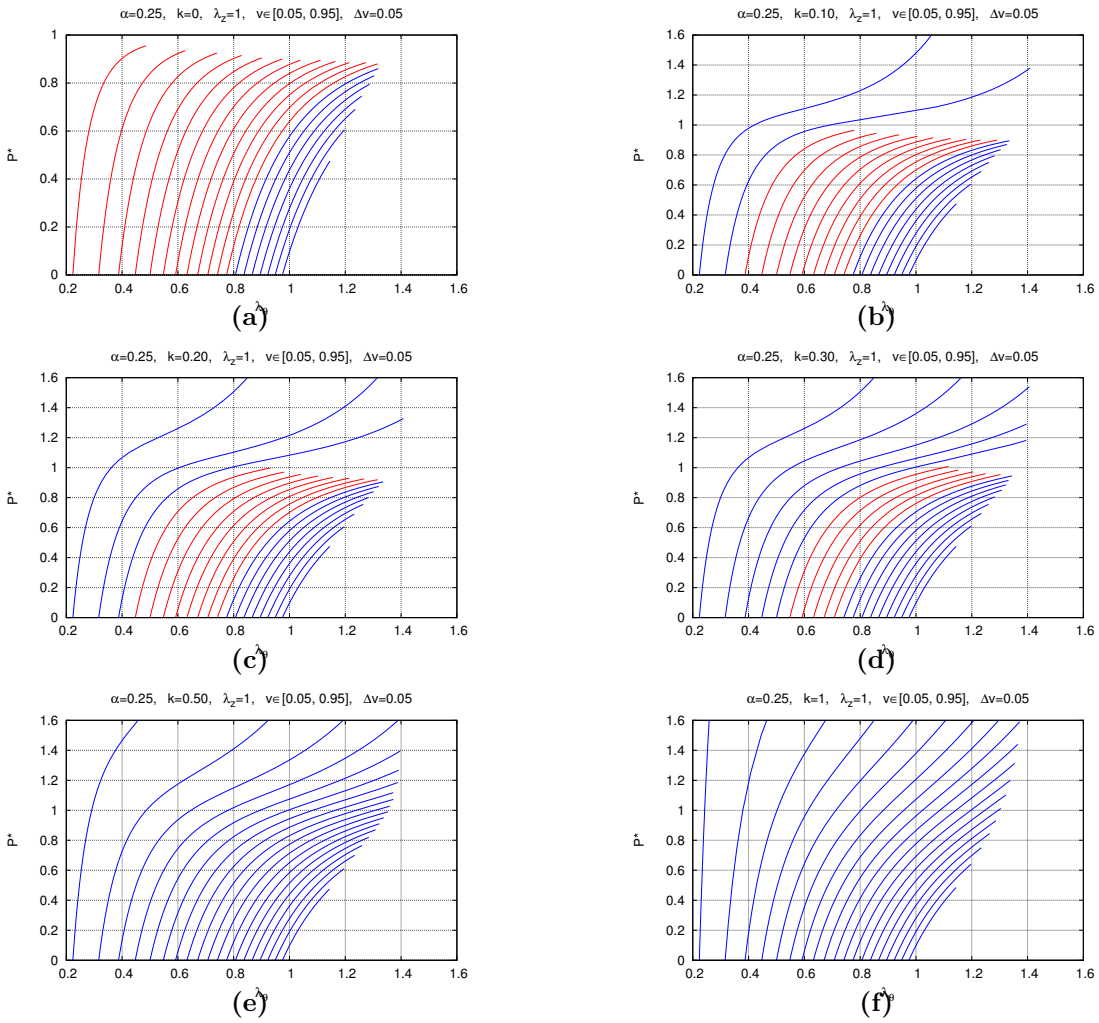

Figure 3.6: Curves give values between pressure P (normalized to $P^* = PR/[H\mu]$) and azimuthal stretch λ_θ for $\lambda_z = 1$, $q = 2/3$, $\alpha = 0.25$, and selected values of k: panel (a) $k = 0.0$, panel (b) $k = 0.1$, panel (c) $k = 0.2$, panel (d) $k = 0.3$, panel (e) $k = 0.5$, panel (f) $k = 1.0$. The different curves are for v in the range of 0.05 (most left curve in each panel) and 0.95 (most right curve in each panel), taking increments of $\Delta v = 0.05$. The curves are restricted to conditions that ensure stability with regard to bulging and bending. A red curve illustrates that stable inflation is interrupted by bulging bifurcation and a blue curve indicates that stable inflation is interrupted by bending bifurcation.

In Fig. 3.7 (d) the (first five) curves for $v = 0.05$, $v = 0.1$, $v = 0.15$, $v = 0.2$, and $v = 0.25$ are interrupted by bending before bulging becomes the relevant instability mode, whereas in Fig. 3.6 (d), the (first four) curves for $v = 0.05$, $v = 0.1$, $v = 0.15$, and $v = 0.2$ are interrupted by bending. In the bottom panels (e) and (f) of both Fig. 3.6 and Fig. 3.7, the Demiray characteristics become sufficiently dominant so that the illustrated stable inflation processes are disrupted by bending bifurcation.

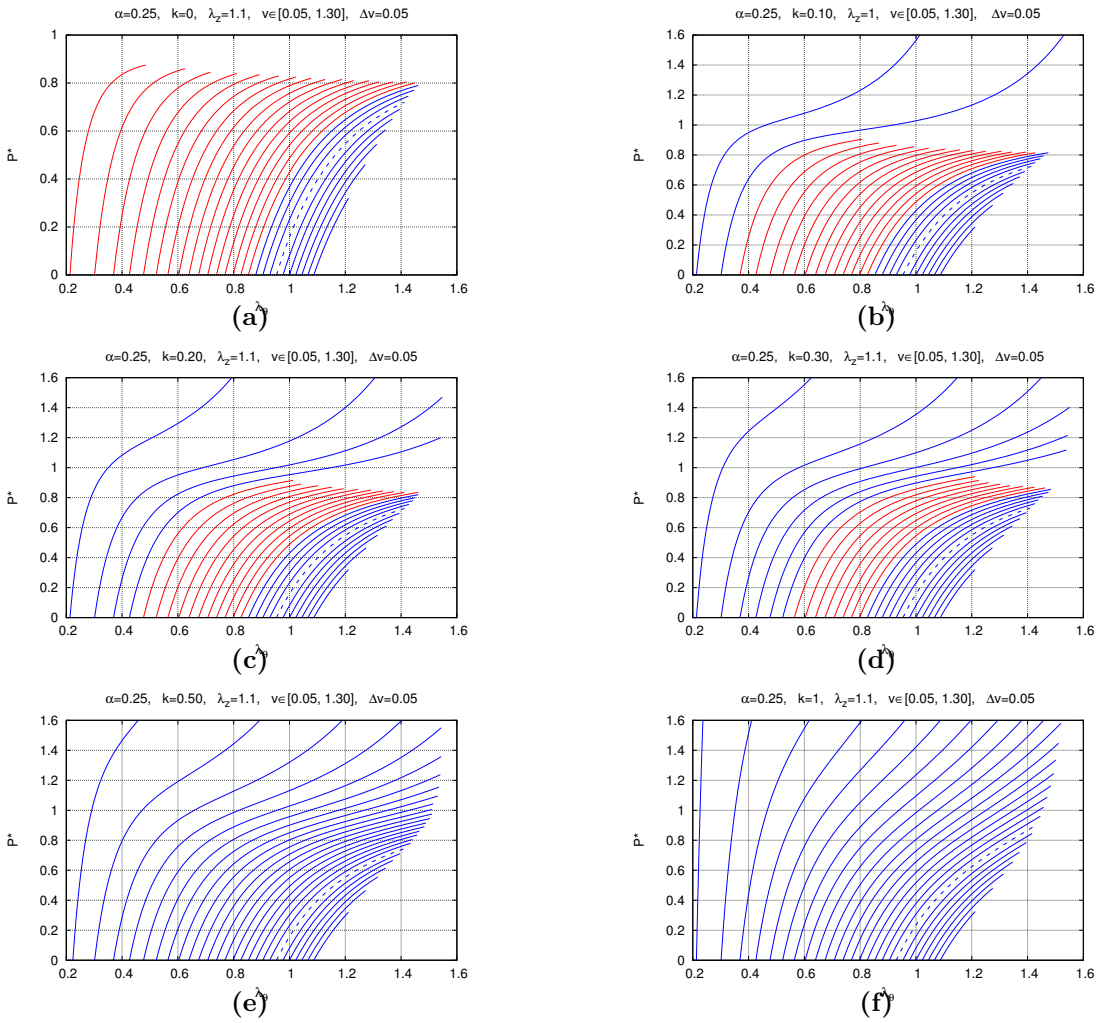

Figure 3.7: Relation between the normalized inflation pressure $P^* = PR/[H\mu]$) and λ_θ. All parameters are the same ones taken previously in Fig. 3.6, except that now the axial stretch is $\lambda_z = 1.1$. The different curves are for v in the range of 0.05 (most left curves) and 1.30 (most right curves), taking increments of $\Delta v = 0.05$. The curve for $v = 1$ is highlighted using a dashed linestyle. A red curve illustrates that stable inflation is interrupted by bulging bifurcation and a blue curve indicates that stable inflation is interrupted by bending bifurcation.

3.5.3 Normal Stress Distribution for $\lambda_z = 1.1$

We turn our attention to the Cauchy normal stresses $\sigma_{\theta\theta}$ in azimuthal direction and σ_{zz} in axial direction during inflation of the cylinder in its stable phase (prior to bifurcation). The substitution of W into (3.8) gives:

$$\begin{aligned}\sigma_{\theta\theta} &= \frac{\lambda_\theta \mu v^{q-2/3}}{2v[1-k+\alpha k]}\left[2\lambda_\theta - \frac{2v^2}{\lambda_\theta^3\lambda_z^2}\right]\left\{[1-k]+\alpha k \exp\left(\alpha\left[\frac{I_1}{v^{\frac{2}{3}}}-3\right]\right)\right\}\\ \sigma_{zz} &= \frac{\lambda_z \mu v^{q-2/3}}{2v[1-k+\alpha k]}\left[2\lambda_z - \frac{2v^2}{\lambda_\theta^2\lambda_z^3}\right]\left\{[1-k]+\alpha k \exp\left(\alpha\left[\frac{I_1}{v^{\frac{2}{3}}}-3\right]\right)\right\}.\end{aligned} \tag{3.30}$$

The cylinder is inflated due to an inner pressure while it remains stable with regards to bulging and bending for $\lambda_z = 1.1$. Figure 3.8 shows values of $\sigma_{\theta\theta}/\mu$ (blue curves) vs. λ_θ and values of σ_{zz}/μ vs. λ_θ (red curves) for different values of α and v.

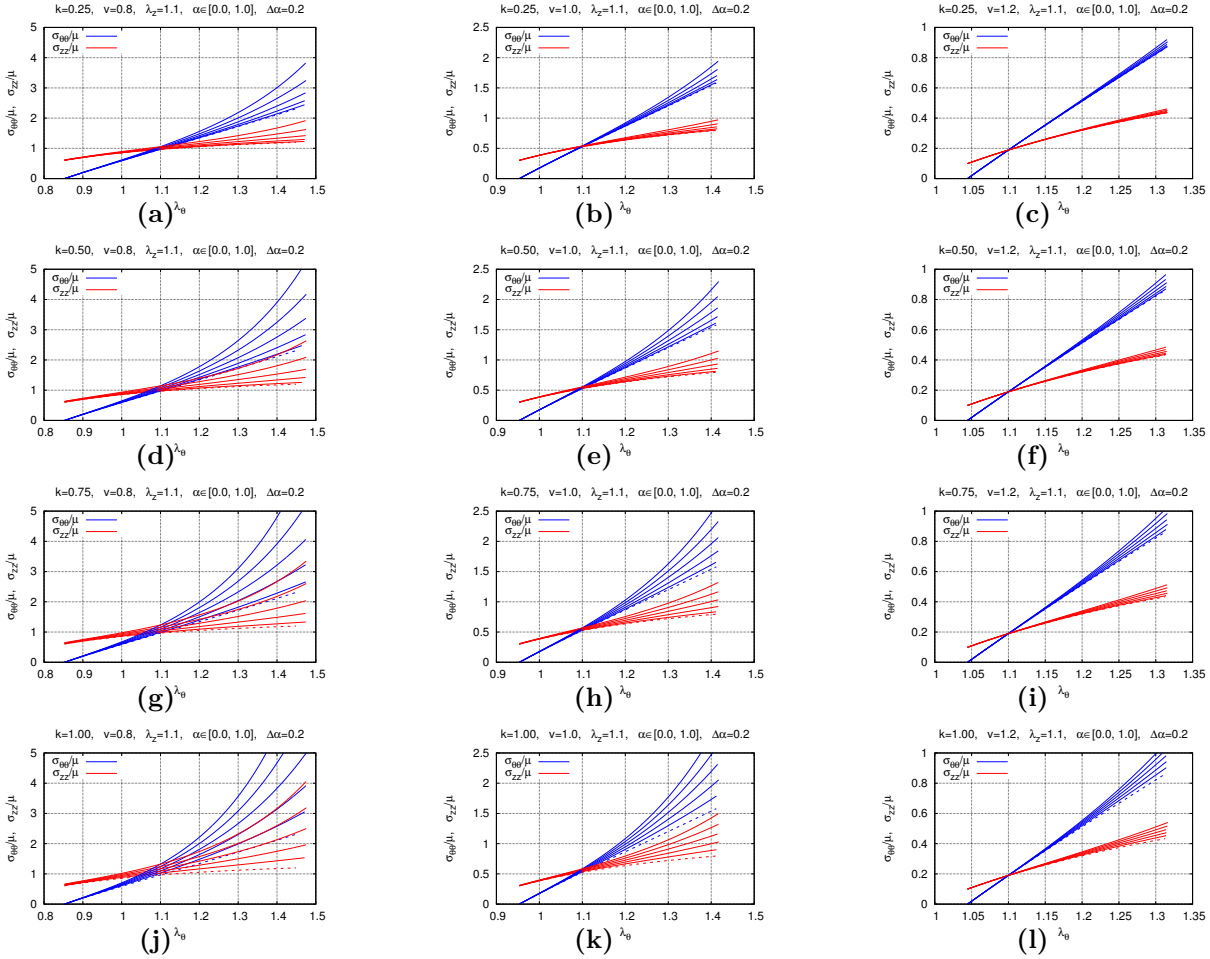

Figure 3.8: The cylinder is inflated due to an inner pressure and it is axially stretched with $\lambda_z = 1.1$ while it remains stable with regard to bulging and bending. Results show values of $\sigma_{\theta\theta}/\mu$ (blue curves) vs. λ_θ and σ_{zz}/μ vs. λ_θ (red curves) for different values of α and v together with $q = 2/3$. In particular, each curve is for a value of α: dashed curves are for $\alpha = 0$, neo-Hookean behavior, while the other curves are for different values of (increasing) $\alpha \in [0, 1]$, with increments $\Delta\alpha = 0.2$. The curves for larger stresses are for larger values in α. The top panels (a), (b), (c) are for $k = 0.25$, the second row (d), (e), (f) is for $k = 0.5$, the third row (g), (h), (i) is for $k = 0.75$. The left panels (a), (d), (g), (j) are for $v = 0.8$ (deswollen material), the center panels (b), (e), (h), (k) are for $v = 1$, and the right panels (c), (f), (i), (l) are for $v = 1.2$ (swollen material).

Note that the curves for the azimuthal stresses have the initial value $\sigma_{\theta\theta} = 0$, whereas the initial value for the axial stresses will vary due to the axial stretch λ_z and the parameters α, k. Due to the isotropic material characteristics we obtain $\sigma_{\theta\theta} = \sigma_{zz}$ when $\lambda_\theta = \lambda_z = 1.1$. From these panels we can make the following observations: The results show that the largest

stress values in stable inflation are obtained for the deswollen material (left panels (a), (d), (g), (j)), whereas in the swollen material, the normal stresses remain relatively small (right panels (c), (f), (i), (l)). By taking larger values for k, larger values of the normal stress may occur. This effect becomes obvious when results from top panels (a), (b), (c) are compared with results shown in the other panels.

3.6 Chapter summary

This chapter focuses on the bifurcation of an inflated and extended swellable isotropic cylindrical membrane, in particular, the material is a combination of the neo-Hookean and the Demiray models. This model, or special cases, found its use in the modeling of various types of soft tissue in which swelling is important but was not considered. Here, the models have been modified to account for swelling and this has important implications in biomechanics, among other applications. Anisotropic effects, for example, due to embedded fibers, have been ignored to highlight the complex bifurcation response of just the purely isotropic material during inflation. It is interesting to note that for the herein considered isotropic model the limiting values $f = 0$, $g = 0$, and $h = 0$, are independent of q. Nevertheless, if fibers would reinforce the isotropic component, then the ratio of the material stiffness of the different components (ground substance and fibers) and therefore the parameter q would influence the bifurcation of the overall material. This analysis is a preliminary step prior to considering fibers that are embedded in an isotropic ground substance, which may lead to a large variety of bifurcation phenomena due to the elastic fiber properties and the fiber arrangement in the ground material [99,100]. In the framework of this chapter, a change in mechanical properties with time has been neglected. In the context of biological tissue, such time-dependent phenomena may be the results of viscoelastic effects and remodeling effects. Such remodeling effects, for example in the collagen structure, may be mechano-sensitive [98, 101]. Some current reviews discuss the underlying phenomena that lead to tissue remodeling in detail (see, e.g., [102–104]). The considered material model is purely elastic, an idealization is applicable when for example the dissipation of energy is negligible for the considered time-scale. Soft tissue consists of a solid and liquid phase so that the material behavior will reveal viscoelastic behavior [105, 106]. Ehlers and Markert [107] present a model that is based on the theory of porous media for the modeling of soft hydrated tissues. It is clear that many parameters affect the behavior of soft tissue and this paper has shown the complexity and the variety of results related to bifurcation with some of these parameters for an isotropic material. The herein-applied membrane treatment often allows for studying bifurcation phenomena analytically. Nevertheless, different comprehensive understanding of the different bifurcation modes can only be studied in the context of thick-walled tubes, for example, when residual stresses are considered [67, 68]. The presented results may be helpful in the planning of more complex numerical treatments, which will invoke larger computational resources. These results can also be useful for the design and planning of experiments that aim to investigate the initiation of bulging and bending in inflated tubular structures [8, 108].

Chapter 4

Computational modeling of bulging and bending bifurcation of residually-stressed cylindrical tubes

4.1 Introduction

Geometric instabilities of under-stressed thin- and thick-walled cylindrical tubes have drawn the attention of researchers in the last few years. In this regard, numerous studies have been done on the application of such structures to the constitution and propagation of aneurysms in arterial wall tissues [109–123]. Stress is expected to be a homoeostatic objective of the standard vessel. However, an aneurysm has a highly degenerative wall, and the biological mechanisms to re-model towards homoeostatic stress are damaged, resulting in a pathological re-modeling of the structural proteins. Apart from the geometrical characteristics of the tubes, the formation of aneurysms contains various biomechanical factors, namely, cell degradation, age, heterogeneity of the material, biochemical reactions, and anisotropy. Nevertheless, the mechanical modulation of this process should be profoundly investigated to be included later in biochemical applications.

Furthermore, geometric nonlinearities of hyperelastic cylindrical extended tubes subjected to internal pressure lead to a bifurcation phenomenon corresponding to a critical state of stability. These instabilities develop various shape modes, the most important of which are bending and bulging modes, and cannot be described by any linear theorem. The development in providing solutions to bifurcation and post-bifurcation problems is a framework that demands attention to prompt new perspectives in scientific and professional fields. The investigation into the behavior of cylindrical tubes during bifurcation and post-bifurcation has attracted significant attention in many biomechanical application fields and other sectors of practical interest. Analytical solutions for the bifurcation are proven to provide insight into the physical interpretation of the problem. Various studies in this direction have concluded that the modes of bifurcation are the so-called prismatic mode, bulging mode, and composite mode [1, 15, 31].

It has been shown that bulging in tubes is usually the result of load instability [82,124,125]. In addition, should the ends of the tube be open transversely, localized bulging can happen even without a pressure limit [126,127]. Generally, localized bulging is related to the bifurcation phenomenon, often commenced prior to or at the onset of the limit load. Furthermore, the stability limit is always associated with the onset of a localized bulge for an infinite or long tube. Several authors have investigated a bifurcation phenomenon [15,50], in which the zero mode is considered to be sinusoidal with axisymmetric deformations, contrary to the findings of Fu et al. [127] that considered the zero modes not to be sinusoidal.

Multiple experiments have concluded that a non-loaded artery is still stressed, see [128,129] and references therein. Thus, conditions such as homeostasis, which is a biological procedure that conserves key regulated variables near different preferred values maintained by living systems, are affected by residual stresses. Also, it is well known that residual stresses in arterial walls arise due to growth and development [109,130].

In this regard, precise representations of the theoretical models are required to fully capture the behavior of residually-stressed cylindrical tubes [31,131]. Investigation of the behavior of an inflated and extended tube without the existence of residual stresses in the context of periodic perturbations is reported in [15,127,128,132]. Unfortunately, analytical approaches demand complex mathematical machinery and are only available for relatively simple cases.

Moreover, there is no analytical method for predicting the mechanical behavior of the tubes undergoing bifurcation, highlighting the necessity to consider alternative approaches. Thus, numerical procedures using the finite element method (FEM) were developed. However, the occurrence of the bifurcation phenomenon within the context of the finite element method (FEM) results in a convergence issue. To overcome such problems, the Riks-based approach was efficiently employed [19], through which the instabilities are modeled as an unknown variable, and the solution is developed using the so-called arc length parameter. In this approach, the load-displacement path is considered as a constraint. Following [9,97], in this paper, ABAQUS finite element software is used with the built-in arc-length method.

Recently, an invariant-based free energy approach has been utilized to model the effects of residual stresses in different analyses [31,97,133]. By exploiting the advantages of this framework, the bulging and bending bifurcation, as well as post-bifurcation of cylindrical tubes under inflation, extension, and torsion were analyzed in [7,9,128,134]. The initial stresses imposed inside the tubes in the mentioned studies were independent of the axial location, while there was no residual shear stress. Regarding the fact that the axial stretch is taken to be constant for the tube, the location of the bulge along the axial direction cannot be defined, indicating that the status of the bulge is independent of the altitude in the given tube.

4.2 Equilibrium equations

It is considered that the material is composed of an in-compressible isotropic hyperelastic material, whose mechanical behavior is described by a strain-energy function. The nominal stress in the reference configuration is provided by (2.5) and the Cauchy stress in the current configuration is provided by (2.6). Moreover, the mechanical response of the body is considered to be according the standard neo-Hookean material law by:

$$\psi = \frac{\mu}{2}\left(\lambda_r^2 + \lambda_\theta^2 + \lambda_z^2 - 3\right) = \frac{\mu}{2}\left(I_1 - 3\right) \tag{4.1}$$

where μ is the material's shear modulus, and $I_1 = \lambda_r^2 + \lambda_\theta^2 + \lambda_z^2$ is the first invariant of the right Cauchy-Green deformation tensor $\boldsymbol{C}$. To take the effects of residual stresses into account, it is assumed that residual stress field exists inside the material body $\boldsymbol{B}_t$ in the absence of body forces and surface tractions on the boundary $\partial\boldsymbol{B}_t$. Concretely, a non-uniform, symmetric second order tensor $\boldsymbol{\sigma}_0$, satisfying the linear and angular equilibrium, is considered to characterize the residual stress field, i.e.,

$$\boldsymbol{\sigma}_0 = \boldsymbol{\sigma}_0^T \tag{4.2}$$

Note that it is assumed that the residual field is a prescribed quantity. Furthermore, a feasible generalization of the strain-energy function of the body that encompasses both the deformation gradient and the residual stress field is given by:

$$\psi_g = \psi(F) + \psi_{rs}(F, \sigma_0) \tag{4.3}$$

in which $\psi_{rs}(\boldsymbol{\sigma}_0)$ presents the residual counterpart of strain-energy. To constitute ψ_{rs} using the invariant formulation, we use invariant I_9 with the following expression:

$$\psi_{rs}(\boldsymbol{\sigma}_0) = \frac{f}{2}\left(I_9 - tr(\boldsymbol{\sigma}_0)\right) \tag{4.4}$$

in which $I_9 = tr(\boldsymbol{\sigma}_0\boldsymbol{C})$. The Cauchy stress tensor takes the form of:

$$\boldsymbol{\sigma} = 2W_1\boldsymbol{B} + 2W_9\boldsymbol{\Sigma}_0 - p\boldsymbol{I}$$
$$\boldsymbol{W}_i = \frac{\partial\psi}{\partial I_i} \qquad i = 1, 9 \tag{4.5}$$

in which $\boldsymbol{B} = \boldsymbol{F}\boldsymbol{F}^T$ is the left Cauchy-Green deformation tensor, and $\boldsymbol{\Sigma}_0 = \boldsymbol{F}\boldsymbol{\sigma}_0\boldsymbol{F}^T$ is the push-forward Eulerian form for $\boldsymbol{\sigma}_0$. Generally, these conditions imply that the residual stress field induces anisotropy on the mechanical response. In literature [7, 135], it is presumed that for a given circular cylindrical geometry, only azimuthal $\boldsymbol{\sigma}_{0\theta\theta}$ and radial $\boldsymbol{\sigma}_{0RR}$ components of the residual stress tensor have a significant effect on the deformation of the body. Under those circumstances, the boundary conditions and the equilibrium in the cylindrical coordinate system take the forms:

$$\sigma_{0RR} = 0 \quad \text{on} \quad R = A, B \tag{4.6}$$

$$\frac{\partial \sigma_{0RR}}{\partial R} + \frac{1}{R}\left(\sigma_{0RR} - \sigma_{0\theta\theta}\right) = 0. \tag{4.7}$$

Furthermore,

$$\sigma_{0RR} = \alpha_r \left(R - A\right)\left(R - B\right) \tag{4.8}$$

is chosen for the radial normal components of the residual stress tensor, which satisfies (4.6); the residual strength parameter α_r has the units of stress per length squared. Equation (4.7) can be utilized to determine the azimuthal component of residual stress field $\sigma_{0\theta\theta}$.

A three-dimensional residual stress distribution has been applied in [97], which is symmetric along the axial orientation of the cylinder with respect to the middle surface of the tube. The present work adopts the phenomenological general three-dimensional residual stress tensor models in [7] and [97]. The residual stress components in the cylindrical coordinate system have the form of:

$$\begin{aligned}
&\sigma_{0RR} = \alpha_r \left(R - A\right)\left(R - B\right) \\
&\sigma_{0\theta\theta} = \alpha_r \left[3R^2 - 2(A+B)R + AB\right] + \alpha_d \left[(R-A)(R-B)(12Z^2 - 12ZL + 2L^2)\right] \\
&\sigma_{0RZ} = \frac{\alpha_d}{R}\left[(R-A)(R-B)(4Z^3 - 6Z^2L + 2ZL^2)\right] \\
&\sigma_{0ZZ} = -\frac{\alpha_d}{R}\left[(2R - A - B)(Z(L-Z))^2)\right] \\
&\sigma_{0R\theta} = \sigma_{0\theta Z} = 0
\end{aligned} \tag{4.9}$$

in which the (second) residual stress parameter α_d has the units of stress per length to the power of four. The two coefficients α_r and α_d will be applied in terms of two non-dimensional parameters $\bar{\alpha}_r$ and $\bar{\alpha}_d$,

$$\begin{aligned}
\alpha_d &= \frac{\mu \bar{\alpha}_d}{2L^4} \\
\alpha_r &= \frac{\mu \bar{\alpha}_r}{2BT}
\end{aligned} \tag{4.10}$$

where μ is a material parameter in the units of stress that can be understood as a shear modulus.

Fig. 4.1. depict the variation of the residual stress components against the dimensionless radius ξ assuming that $\bar{\alpha}_r = 2\xi$, $\bar{\alpha}_d = 40$, and $Z = L/3 = 50$.

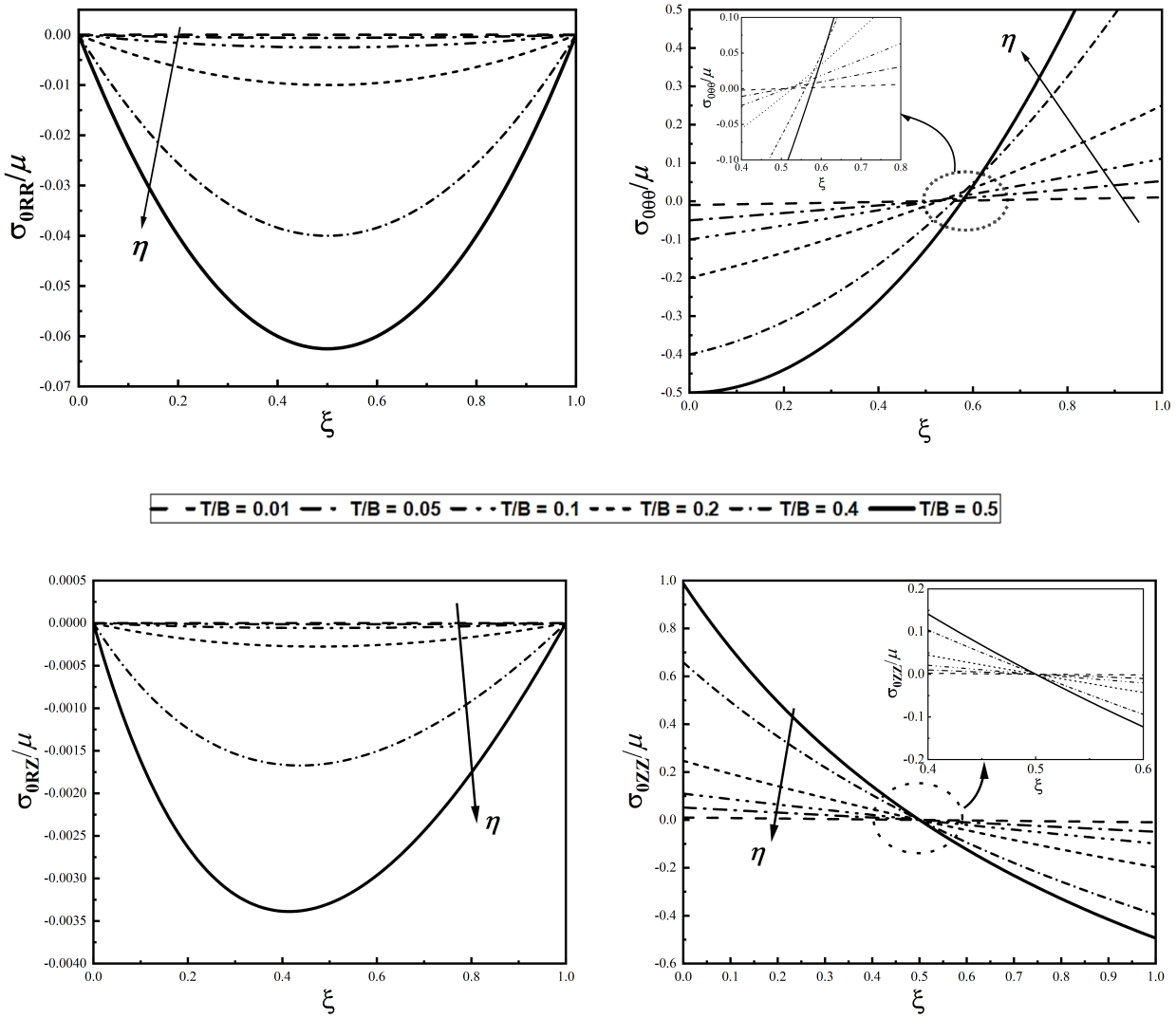

Figure 4.1: Residual stress components against radius ξ; the legend shows the value of thickness ratio $\eta = T/B$; the arrow indicates the increasing value of η.

4.3 Initiation of bifurcation in thick-walled inflated tubes

We recall that the bifurcation modes are categorized in three modes: 1) the prismatic form, in which the increments of displacement are independent of the longitudinal movements, 2) the bulging form, which assumes that $\delta\boldsymbol{u}$ is independent of θ, leading to a axisymmetric displacement retaining the circular shape of the cross-section. 3) the bending mode, also called the composite form, which is a general case with no assumptions interpreted as the combination of bulging and prismatic modes. To capture the bending bifurcation mode, an

analogy between a membrane and tube is used. For a membrane bending bifurcation, the following equilibrium is assumed:

$$\sigma_{\theta\theta} = 2\sigma_{zz} \tag{4.11}$$

In the case of tube with a thickness, the average values of σ_{zz} and $\sigma_{\theta\theta}$ are used. Concretely, the unstable state of bending bifurcation starts with $\sigma_{\theta\theta} > 2\sigma_{zz}$ [9].

4.4 Finite element analysis

In recent years, numerous analyses have explored boundary value problems within the realm of stability theory [1, 15, 126, 127]. More recently, attention has turned to the bifurcation of isotropic thick-walled cylinders [25]. Among the instability modes observed in stretched pressurized cylinders, bulging typically emerges as the primary mode [25]. This bulging bifurcation mode is determined by examining axisymmetric incremental displacements relative to a deformed configuration, all of which maintain equilibrium. Consequently, incremental displacements are negligible along the hoop direction and remain independent of the azimuthal angle.

In this chapter, we employ a numerical approach to investigate the bifurcation and post-bifurcation behavior of hyperelastic thick-walled cylinders inflated under pressure, utilizing the modified Riks method. While analytical solutions have been established in literature for particular scenarios involving specific material models, applied loads, and often idealized geometries, our aim here is to present a unified methodology applicable to more general conditions for predicting both bifurcation and post-bifurcation propagation. We demonstrate that under the considered conditions, bulging instability propagates longitudinally. For this purpose, the framework presented in section 4.2 is implemented into the finite element (FE) package ABAQUS/standard through a user-defined material subroutine (UMAT), incorporating the initial residual stress state and hybrid almost-in-compressible formulation. For the analysis, the deformation of the tube is considered as a function of various axial stretches λ_z and different residual stress state categorized by $\bar{\alpha}_r$ and $\bar{\alpha}_d$ parameters.

4.4.1 Riks analysis: classic and modified method

In finite element analysis (FEA), both the Riks method and the modified Riks method are numerical techniques used to solve nonlinear structural problems. While they share similarities in their underlying principles, they also exhibit distinct characteristics that make each method suitable for different types of nonlinear analyses. The Riks method, also known as the arc-length method or the displacement control method, is a powerful numerical technique used to solve nonlinear structural problems. It is particularly effective for analyzing structures undergoing large deformations, buckling, or instability phenomena. Traditional methods for solving nonlinear problems in FEA, such as the Newton-Raphson method, often encounter difficulties when dealing with highly nonlinear or geometrically unstable systems. These methods may struggle to converge or become computationally expensive, especially when the structure undergoes large displacements or experiences snap-through behavior.

The Riks method addresses these challenges by introducing an arc-length parameter into the solution process. This parameter acts as a constraint on the incremental displacement vector, ensuring that the solution path follows a smooth trajectory along the load-displacement curve. By controlling the arc-length parameter, the Riks method can effectively trace the equilibrium path of the structure, even in the presence of large deformations or geometric instability. One of the key features of the Riks method is its ability to handle both stable and unstable equilibrium paths. In cases where the structure undergoes buckling or snap-through behavior, the Riks method can continue to trace the equilibrium path beyond these critical points, providing valuable insights into the post-buckling behavior of the system.

On the other hand, the modified Riks method builds upon the foundation of the classic Riks method but incorporates additional features to address certain limitations and enhance computational efficiency. One key difference is that the modified Riks method employs a more sophisticated arc-length control strategy, such as adaptive time-stepping or predictor-corrector algorithms, to improve convergence and stability. This allows for more robust and efficient simulation of highly nonlinear problems, especially those involving complex geometries or material behaviors. Another important distinction is that the modified Riks method often includes enhancements to handle contact, friction, or other types of nonlinear boundary conditions commonly encountered in practical engineering applications. By incorporating specialized algorithms for handling these boundary conditions, the modified Riks method can accurately simulate the behavior of contact interfaces or frictional surfaces, which are crucial in many structural analyses. Furthermore, the modified Riks method may offer additional options for controlling convergence criteria or adjusting solution parameters, providing greater flexibility in tailoring the analysis to specific engineering requirements. These refinements make the modified Riks method a valuable tool for simulating a wide range of nonlinear problems with improved accuracy and efficiency compared to the classic Riks method. Overall, the Riks methods are particularly well-suited for analyzing structures subjected to static or quasi-static loading conditions. It has been widely used in various engineering disciplines, including aerospace, civil engineering, mechanical engineering, and bio-mechanics, to simulate the behavior of complex structures under realistic loading scenarios.

In our approach, we begin by subjecting the cylindrical model to axial displacements, effectively stretching it while maintaining its cylindrical shape by imposing hoop constraints. Next, pressure is applied to observe both instability and post-critical behavior. The modified Riks method incorporates two key elements: the load proportional factor (LPF) and the arc length, which are further detailed in [2]. The arc length represents a measure of the structure's evolution, combining displacements and loads. Meanwhile, the load proportional factor governs the applied load and has the potential to decrease. Notably, the Riks method becomes less effective when the load proportional factor exhibits a monotonic increase.The Riks scheme generates two parameters, namely, the load proportionality factor (LPF) and the arc length. The former is a factor of the applied pressure such the total amount of applied load is equal to the magnitude of internal pressure multiplied by the LPF. In an analysis, the value of LPF rises until an instability occurs, causing a decrease in the LPF value. The arc length parameter shows the evolution of the load-displacement path.

4.4.2 Geometry, material model, and loading conditions

A double-layered cylindrical tube with the length of 150 mm and total thickness of 1 mm is considered. The two layers have identical thickness and different inner and outer radius. The inside layer has the inner and outer radius of 4.5 mm and 5.0 mm, respectively, while and outer one has the inner and outer radius of 5.0 mm and 5.5 mm, respectively. The material used for the tubes is the neo-Hookean isotropic hyperelastic constitutive model. To ensure a smooth solution during loading, a minor imperfection must be introduced into the geometry, as elaborated in the subsequent section. The pressure displacement formulation (hybrid) is recommended when material behavior is in-compressible or close to in-compressible [136]. This is because the hybrid elements combine the advantages of different types of finite elements to provide enhanced accuracy, efficiency, and versatility in solving a broader range of engineering problems. The concept of hybrid elements involves incorporating multiple types of interpolation functions within a single element, allowing for more flexible representations of the solution field. This enables the element to adapt to various material behaviors. In addition to their versatility, hybrid elements offer advantages in terms of computational efficiency. By tailoring the element formulation to the specific characteristics of the problem, hybrid elements can reduce the computational cost while maintaining high accuracy. Thus, three-dimensional eight-node reduced integration solid elements with hybrid formulation C3D8RH were used for the geometry discretization. Based on the previous investigations, various meshing discretization were utilized in this study ranging from 200 to 300 elements in the axial direction depending. For bending and bulging (i.e., restricted azimuthal displacements) analyses, 64 elements in the circumferential direction in 4 layers are considered for each tube, making it a total of 256 elements in the circumferential direction. Fig. 4.2 presents the details of the meshing of the tubes.

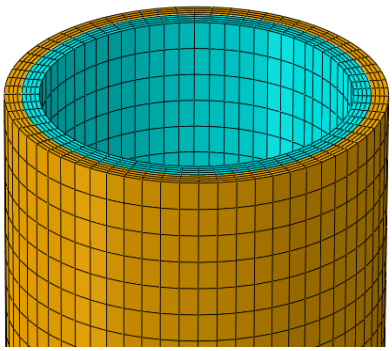

Figure 4.2: Mesh discretization of the finite element model.

4.4.3 Analysis scheme

In the analyses, longitudinal displacements (axial stretch) constraints at the ends of the cylinder are imposed. To capture the bulging instability, hoop displacements are prevented during the analysis. One the other hand, no hoop restriction were imposed for bending bifurcation. The bending and bulging analyses consist of three stages. First, the residual

(initial) stresses are introduced to the finite element model utilizing the SDVINI subroutine. The subroutine defines the initial stress values to the model using (4.9). For convenience, the dimensionless parameter $\bar{\alpha}_r$ and $\bar{\alpha}_d$ are used to define the initial values. Based on the previous literature [97], the values are set to $\bar{\alpha}_d \in \{-40, 0, 40\}$ and $\bar{\alpha}_r \in \{-0.5, 0, 0.5\}$, see Table 4.1.

Table 4.1: Values of residual stress parameters $\bar{\alpha}_d$ and $\bar{\alpha}_r$ for the analyses

case	$\bar{\alpha}_R$	$\bar{\alpha}_d$
1	0.5	40
2	-0.5	40
3	0.5	-40
4	-0.5	-40
5	0	40
6	0	-40
7	0	0
8	0.5	0
9	-0.5	0

These values are adjusted such that their effects do not cause any instability. Fig. 4.3 depicts the stress components across the thickness of the cylinder at $Z = L/4$.

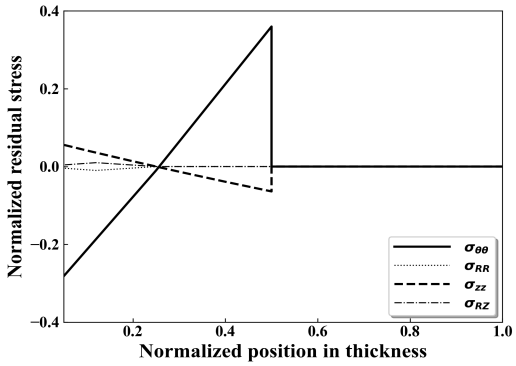

Figure 4.3: Stress components along the thickness at $Z = L/4$ (Case 1)

Moreover, Fig. 4.4 shows the von Mises stress for the inner and outer layer of double-layered cylinder. In the second stage, axial displacements are applied to one end, while restricting the other end. It should be noted that in order to retain the circular cylindrical cross-section, hoop displacements are prohibited. This process will introduce axial stretch to the mode. Finally, an internal pressure is applied directly to the inner layer of the tube using Riks analysis.

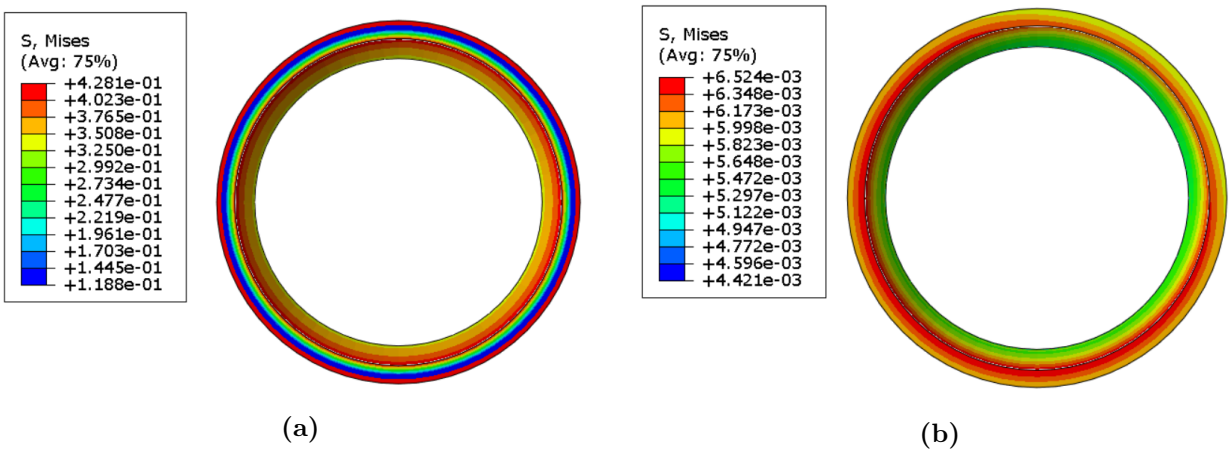

Figure 4.4: Von Mises stress for (a) the inner and (b) the outer layer, respectively, for a prestressed double-layered cylindrical

To identify the bulging mode, the variation in hoop displacements (stretches) are monitored in two points, one point inside the bulge and the other outside. The bulging mode identifies when the profile of displacement of these two points differs more than 1% [97]. The azimuthal displacement of the inside point increases as bulging progresses, while azimuthal displacement of the other point decreases. In the case of bending mode, no restrictions are applied along the length of the tube. Moreover, to identify the initiation of bending mode, a combination of radial and azimuthal stretches is calculated to capture the lateral displacement, pointing out the onset of bending mode. In this study, the first bending mode is captured, according to Fig. 4.5.

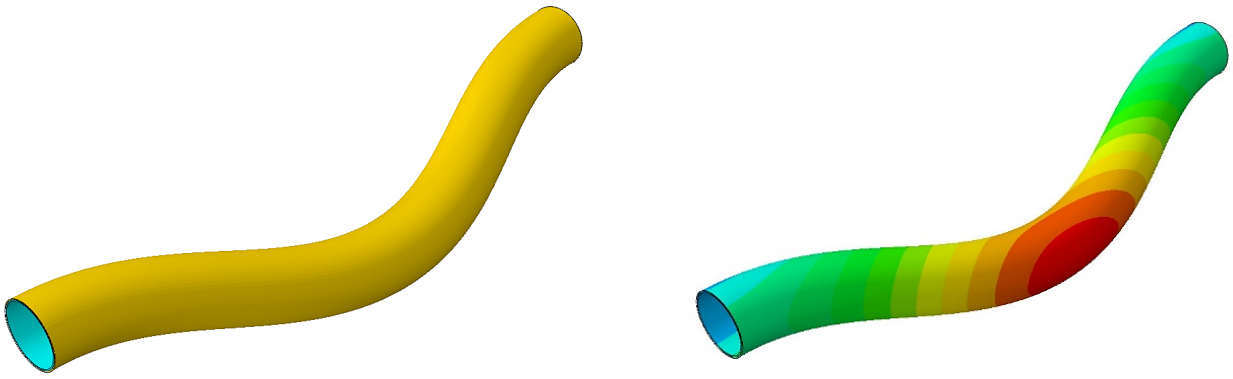

Figure 4.5: First mode of bending bifurcation for double-layered cylindrical tube.

For each case, various internal pressure and axial stretches in the range of $1 \leq \lambda_z \leq 1.8$ is applied and studied. Also, the results are normalized for material constant $\mu/2$.

4.5 Finite element results

As stated in literature, the membrane conditions are identified for capturing the bifurcation phenomenon. Also, it is stated that the instability mode is heavily based on the amount of axial stretch [7, 9]. Starting from the Case 1 in Table 4.1, where both $\bar{\alpha}_r$ and $\bar{\alpha}_d$ have positive values, the values for Eq. 4.9, where the values are average stresses in the cross-section, are shown in Fig. 4.6 against the arc length for (I) $\lambda_z = 1$ (dashed line), (II) $\lambda_z = 1.4$ (solid line).

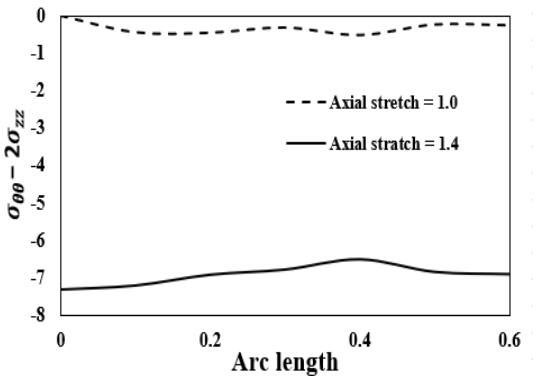

Figure 4.6: Values of $\sigma_{\theta\theta} - 2\sigma_{zz}$ against the arc length for Case 1 for $\lambda_z = 1.4$ and $\lambda_z = 1$

Similar to the findings of [97], the values are negative for both, leading to the fact that the bulging bifurcation is the main instability that is to be expected. In [97], the values of $\sigma_{\theta\theta} - 2\sigma_{zz}$ where slightly positive for $\lambda_z = 1$ for a one-layered tube. However, in this study, the effect of having an extra layer produces negative results for $\sigma_{\theta\theta} - 2\sigma_{zz}$, thus ensuring a bulging bifurcation. Fig. 4.7 depicts step-by-step deformation history of the bulging bifurcation associated with Case 1 for $\lambda_z = 1.2$.

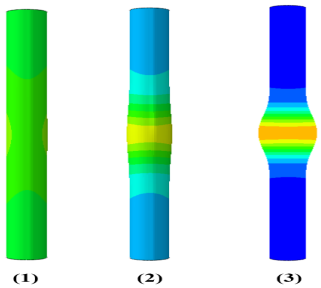

Figure 4.7: Deformation history of the bulging mode for $\lambda_z = 1.2$ for Case 1

As it can be seen, the early stages the configuration of the tube is stable. On the other hand, the initiation of bulging bifurcation is seen in stage 2. Stage 3 shows the post-bifurcation configuration of the tube, which is radial propagation of the bulging. Furthermore, we turn our attention to interesting bulging modes that is associated with a combination of the modes. Our simulations pointed out that in double-layered cylinders, two other bulging phenomena can appear in a simulation. It was shown in the findings of [7, 97] for one-layered tubes that

bulging mode can appear at the ends of cylinder. In this study, similar results were extracted as shown in Fig. 4.8, which is similar to [97]. Nevertheless, combinations of bulging modes appear in the analyses of double-layered cylinders. The first combination is generated with two radial expansions, Fig 4.9. The other is combination of the bulging in the middle of the tube in the form of radial expansion and bulging modes at the ends, Fig 4.10. Interestingly, the stated modes appear for $\lambda_z = 1.2$ with different values of $\bar{\alpha}_r$ but $\bar{\alpha}_d = 0$. Also, Fig. 4.11 shows the values of LPF vs arc length for three bulging modes stated before for $\lambda_z = 1.2$ with Cases 3, 8, and 9.

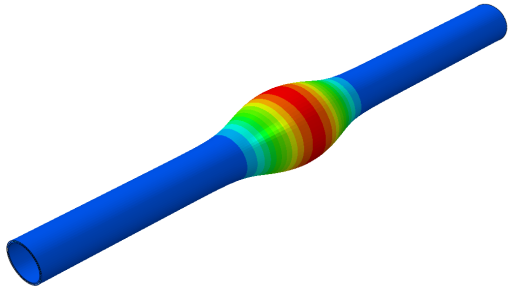

Figure 4.8: Bulging mode appearing at the ends of the tube for $\lambda_z = 1.2$ for Case 3

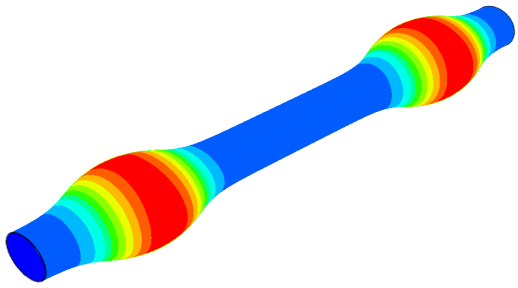

Figure 4.9: Combined bulging mode of the tube for $\lambda_z = 1.2$ for Case 8

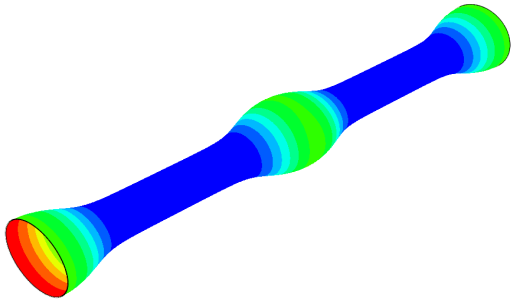

Figure 4.10: Combined bulging mode of the tube for $\lambda_z = 1.2$ for Case 9

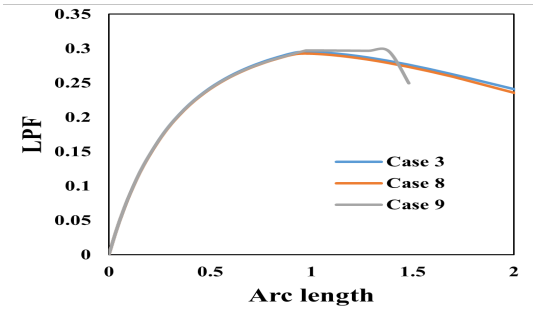

Figure 4.11: Values of the LPF vs arc length for $\lambda_z = 1.2$ for Case 3, 8, and 9. Case 3 leads radial bulging at the middle of cylinder, while Case 8 is associated with bulging at the ends of cylinder. Case 9 is a combination of the two modes.

We turn our attention to the effects of $\bar{\alpha}_r$ and $\bar{\alpha}_d$, and their sign on the location of bulging bifurcation. For the sake of brevity, only notable results are given for double-layered cylinders as follows. It was seen that the when $\bar{\alpha}_d$ is negative, bulges develop at the ends of cylinder. Moreover, when $\bar{\alpha}_d$ is zero, combined bulges occur. Other results are in accord with the findings of [97] for one-layered cylinders. Focusing on lower amount of axial stretch in order to capture the bending bifurcation, we use the identical model with $\lambda_z = 1.5$ having the same value for $\bar{\alpha}_r$ but different values for $\bar{\alpha}_d$ (Cases 1 and 3). Our analyses show that for lower values of axial stretches, the bending instability happens first and then bulging bifurcations follow. Fig. 4.12 shows the results obtained for these cases in terms of deformation instability and $\sigma_{\theta\theta} - 2\sigma_{zz}$ along the tube's length.

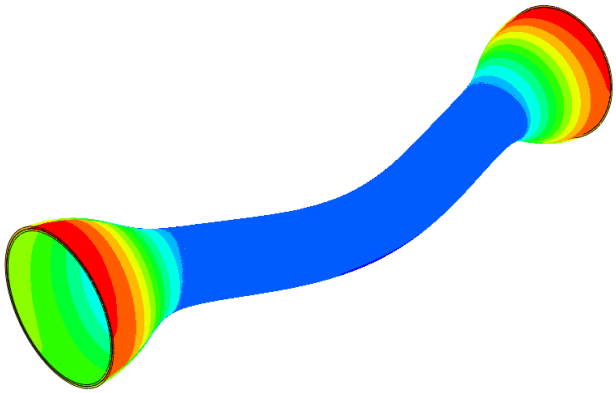

(a) Bending bifurcation followed by bulging at the ends for Case 1

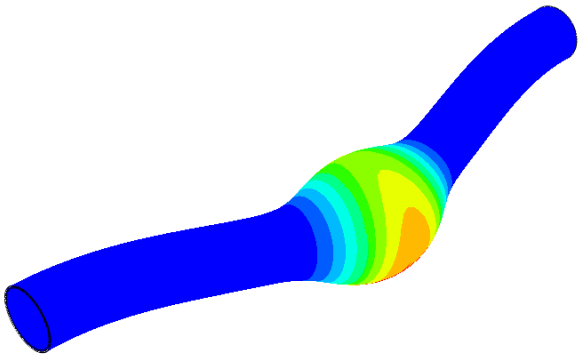

(b) Bending bifurcation followed by bulging at the ends for Case 3

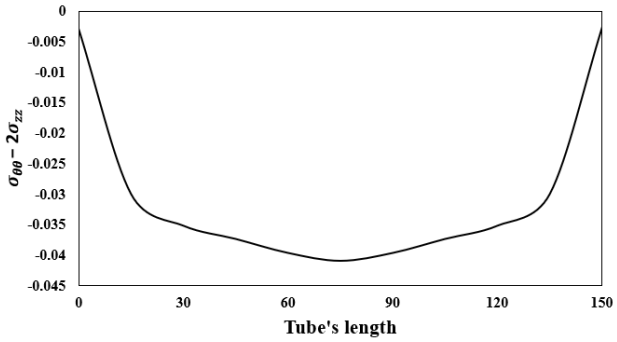

(c) The value of $\sigma_{\theta\theta} - 2\sigma_{zz}$ along the tube's length for Case 1, representing the moment along the length

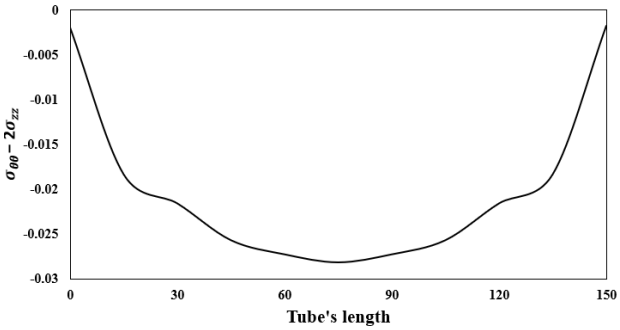

(d) The value of $\sigma_{\theta\theta} - 2\sigma_{zz}$ along the tube's length for Case 3, representing the moment along the length

Figure 4.12: Bending bifurcation mode for $\lambda_z = 1.15$

In Fig. 4.12a and Fig. 4.12b, the bifurcation instabilities of the cylinders are shown. Concretely, the sign of $\bar{\alpha}_d$ alters the instability location. Also, Fig. 4.12c and Fig. 4.12d implicate the value of $\sigma_{\theta\theta} - 2\sigma_{zz}$ representing the bending moment causing the bending bifurcation to peak in the middle of the tube's length just before the bulging. Furthermore, for the model associated with $\lambda_z = 1.15$ and $\bar{\alpha}_r = 0.5$ but $\bar{\alpha}_d = 0$, bulging instability occurred after bending bifurcation, as shown in Fig. 4.13a and Fig. 4.13b. This is in accord with the findings of [16, 76, 97], where it is stated that the $\bar{\alpha}_r$ dominantly controls the bulging bifurcation. Also, a history of $\sigma_{\theta\theta} - 2\sigma_{zz}$ along the tube's length after bending bifurcation and prior to bulging is shown in Fig. 4.13c and Fig. 4.13d.

Moreover, numerous analyses were conducted to draw a correlation between the different cases presented in Table 4.1 and bulging bifurcation (in which the azimuthal displacements are restricted) in variation with different axial stretches. The results of the analyses are depicted in Fig. 4.14, showing the normalized inner pressure vs axial stretch (λ_z) at the initiation of bulging instabilities for all the nine cases. As was stated in literature, the values of inner pressure decrease as the axial stretches rise. Also, analyses with no displacement restrictions were carried out to obtain the values of normalized inflation pressure against the axial stretches resulting in bending bifurcations, see Fig. 4.15. Similar to one-layered cylinders, $\bar{\alpha}_r$ mainly control the instabilities, while the sign of $\bar{\alpha}_d$ do not possess a significant

impact on the bending bifurcation. Concentrating on the small values of axial stretch (λ_z), it can be deferred that small values of (λ_z) leads to bending. For axial stretches higher than 1.2, a bulging bifurcation is expected to occur.

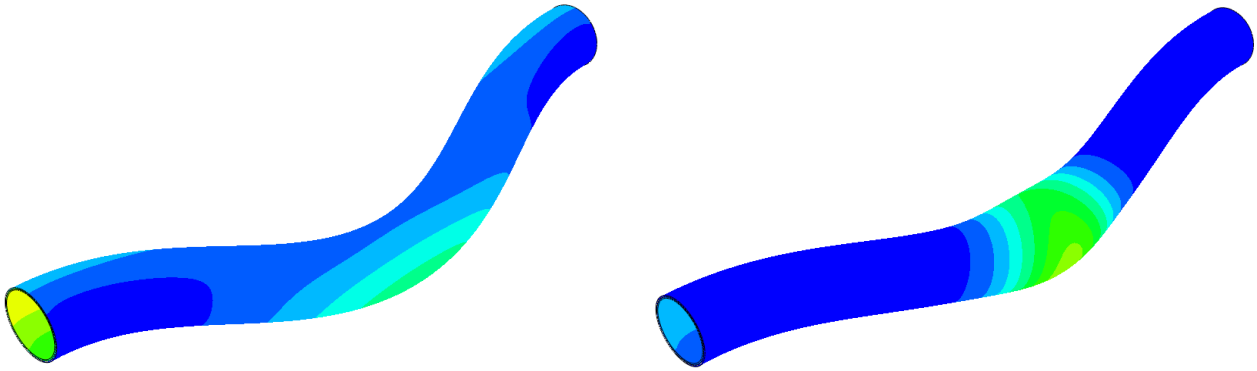

(a) Deformation after bending bifurcation and prior to bulging

(b) Deformation after bending bifurcation and at the initiation of bulging

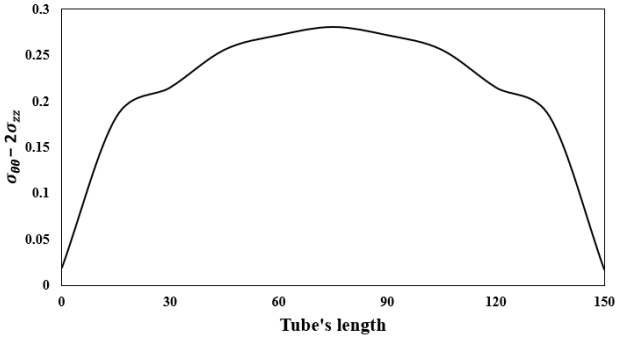

(c) The value of $\sigma_{\theta\theta} - 2\sigma_{zz}$ along the tube's length prior to bulging

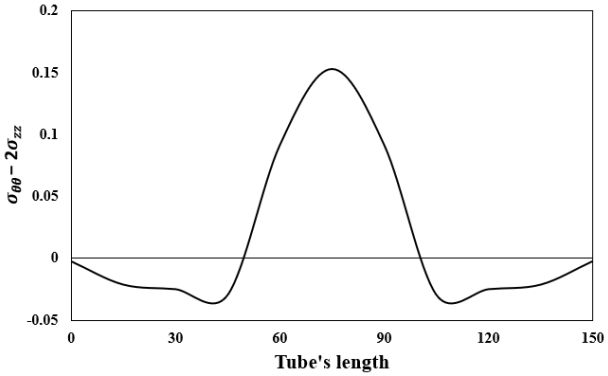

(d) The value of $\sigma_{\theta\theta} - 2\sigma_{zz}$ along the tube's length after bending bifurcation and at the initiation of bulging

Figure 4.13: Bifurcation mode for $\lambda_z = 1.15$ with $\bar{\alpha}_r = 0.5$ but $\bar{\alpha}_d = 0$

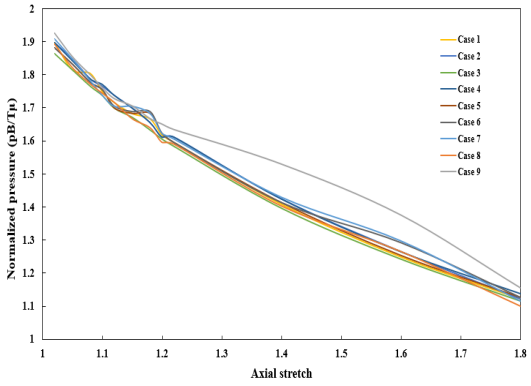

Figure 4.14: Values of normalized pressure $pB/T\mu$ vs axial stretch. For cases with zero $\bar{\alpha}_d$, the decrease in normalized pressure is lower compared with that of the other cases.

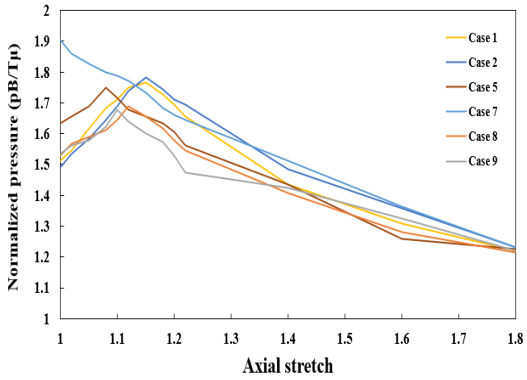

Figure 4.15: Normalized pressure $pB/T\mu$ vs axial stretches for different cases. Only the cases with positive value of $\bar{\alpha}_d$ is shown. Concretely, bending bifurcation is expected to occur when the axial stretch is below 1.2.

Based on prior research in the literature, the abnormal deformations associated with bulging or bending instabilities could results in developing abdominal aortic aneurysms (AAA) and aneurysm rupture. Moreover, combined bulging instabilities as shown in Fig. 4.9 and Fig. 4.10 were seen in double-layered cylinders. It is also seen that aneurysm would occur if azimuthal displacements are prohibited. Furthermore, a transition from bending bifurcation to bulging instability was observed for lower values of axial stretches, while higher values of axial stretches lead to bulging instabilities.

4.6 Chapter summary

In this chapter, non-linear finite element analysis of double-layered cylindrical tubes including residual stresses subjected to axial stretch and internal pressure were carried out to investigate the application of mechanical and material aspect in developing abdominal aortic aneurysms (AAA) and aneurysm rupture. In this regard, user-defined subroutines associated with initial field conditions (SDVINI) and a strain energy function were utilized to incorporate initial residual stresses into three-dimensional analysis. Moreover, the framework presented in [97] were used that considers the axial and azimuthal stresses. Also, bulging and bending instabilities regarding the axial stretches and initial condition were investigated. It was shown that:

I) For large values of axial stretch, the axial stress is sufficiently large to produce bulging instability rather than bending instabilities. Moreover, combined modes of bulging bifurcations were observed for double-layered cylindrical tubes, which can aggravate the possibility of developing of abdominal aortic aneurysms (AAA).

II) For axial stretches lower than 1.2, bending bifurcations were captured. Nevertheless, for some initial conditions, bulging instabilities in the form of radial expansions follow after the bending bifurcation occurs. This kind of behavior also leads to aneurysm rupture.

III) In the cases where the initial condition $\bar{\alpha}_d = 0$, the internal pressure that causes the instabilities decrease more rapidly when the axial stretch is higher λ_z than 1.2. Moreover, it was deduced that the internal pressure is associated with both the initial condition and axial stretch for $\lambda_z \leq 1.2$. However, when $\lambda_z > 1.2$, the internal pressure is more related to the axial stretch.

IV) It was seen that the location of bulging bifurcation is dependent on the sign of $\bar{\alpha}_d$, whereas in bending instabilities the sign $\bar{\alpha}_r$ is the main role.

Chapter 5

Helical buckling of anisotropic tubes with application to arteries

5.1 Introduction

The identification of such instability modes with tubes under a finite torsion has attracted a great deal of clinical attention in bio-medical fields. The onset of bifurcation and instability patterns has been a recurrent topic which led to several different types of constitutive models. Majorly, these investigations (on uncoupled problems) have been dealing with non-linear aspects considering constitutive models that are defined in terms of invariants of the right Cauchy–Green deformation tensor. Very recently, some studies incorporate pre-stress. The distribution of initial stress plays an important role in driving the instability at hand [7, 9, 97, 128, 134, 137–140, 140, 141, 141–144]. The influence of fiber orientation, pre-stretch, and dispersion, as well as the interplay between these factors on the initiation of buckling in a pressurized cylinder, has been studied in [145, 146]. Buckling of an artery using a fiber-reinforced model is of interest here in this chapter [82, 147–149]. In particular, we investigate the helical bifurcation and post-bifurcation for a tube made of an anisotropic hyperelastic model [150], which is supposed to behave like arterial tissue [151]. We augment the strain energy of an isotropic material (in this case neo-Hookean model) with the reinforcing model that depends on higher-order invariants denoted in the literature as I_5 and I_7 [150]. These invariants are related to fiber stretch and fiber shearing and have not been used under the present circumstances. The free energy of our reinforcing model is taken as a quadratic model. The constitutive model is implemented in a commercial finite element code ABAQUS via user subroutine UANISOHYPER-INV. With the help of this routine, it is possible to define the strain energy function of anisotropic materials as a function of an irreducible set of scalar invariants. The model at hand is shown to describe the mechanics underlying the propagation of the helical instability under various mechanical loading conditions. Nevertheless, the proposed modeling framework is easily extendable to alternative material models and applications. For example, as a straightforward extension, residual stresses and damage variables can be included in future studies. The effect of inflation pressure on the stretched and twisted tube is of primary interest here. This is a significant challenge to overcome when

analyzing this problem. Mainly, boundary value problems can rarely be solved in a closed form, and hence no analytical solution is available for the onset of bifurcation for a given finite deformation boundary-value problem. Consequently, the self-contact interaction at the outer surface and coupling between inflation, extension and twist must be solved using numerical schemes with specified model parameters. In this communication, we focus on the buckling of thick tubes under a finite torsion using the commercial finite element code ABAQUS using Riks and quasi-static procedure. The present research builds on the research work cited previously with a twofold objective: (1) the identification of critical pressure and torque for a given loading; (2) the interplay of pressure, axial loading, and twist on buckling modes and identification of the shape of (intermediate) deformation patterns. In this chapter, the details of main equations including the constitutive framework consisting of the energy contribution from the neo-Hookean and the reinforcing model in the spirit of [150] is presented. The material model follows the invariant-based phenomenological approach, which allows writing the constitutive model in a simple manner. Next, a critical pressure and torque following the static analysis procedure are identified under different loading conditions. After introducing the geometric imperfection to facilitate the propagation of the buckling mode we analyze post-bifurcation for different values of the axial stretch. Moreover, a presentation of the quasi-static numerical analysis for the extension–inflation–twist at a value of pressure to capture the critical bifurcation torque is shown. Different scenarios considering internal pressure and axial stretch are investigated as parameters to understand the effect of lumen pressure on bifurcation modes and post-bifurcation. The dependence of bifurcation on different loading and chosen constitutive and geometrical parameters are illustrated and compared.

5.2 Description of the problem: Material, geometry, and kinematics

Here we introduce the main equations and the description of the problem at hand (see [152] and [153] for further details).

Consider a cylindrical tube made of hyperelastic material with an initial inner radius A, outer radius B, and axial length L. The wall thickness is $T = B - A$. A representative material point in the reference $\boldsymbol{B}_0$ and deformed configurations $\boldsymbol{B}_t$ has the cylindrical polar coordinates $\boldsymbol{X} = (R, \Theta, Z)$ and $\boldsymbol{x} = (r, \theta, z)$, respectively.

$$\begin{aligned} &\boldsymbol{X} = R\boldsymbol{E}_R(\Theta) + Z\boldsymbol{E}_Z \\ &A \leq R \leq B \\ &0 \leq \Theta \leq 2\pi \\ &0 \leq Z \leq L \end{aligned} \tag{5.1}$$

in which $\boldsymbol{E}_R$, $\boldsymbol{E}_\Theta$ and $\boldsymbol{E}_Z$ are unit vectors in the indicated direction. The tube deforms

keeping its cylindrical geometry. In $\boldsymbol{x} \in \boldsymbol{B}_t$, the general form of the tube can be expressed as:

$$\begin{aligned} &\boldsymbol{x} = r\boldsymbol{E}_r(\theta) + z\boldsymbol{E}_z \\ &a \leq r \leq b \\ &0 \leq \theta \leq 2\pi \\ &0 \leq z \leq l \end{aligned} \tag{5.2}$$

where e_r, e_θ, and e_z are unit vectors in the deformed configuration and the deformed length of the cylinder is identified by l.

Consider firstly just inflation and extension of the tube. Under the conditions at hand, one can consider an in-compressible, anisotropic, and nonlinear elastic material with two preferred directions, defined by unit vectors $\boldsymbol{M}$ and $\boldsymbol{M'}$, in which one fiber is distributed with unit vector $\boldsymbol{M}$ given by the orientation ϕ relative to the Z-axis whereas the other fiber is distributed with unit vector $\boldsymbol{M'}$ given by the orientation $-\phi$. In vector form, it takes the following form $\boldsymbol{M} = (0, \sin(\phi), \cos(\phi)$ and $\boldsymbol{M'} = (0, \sin(-\phi), \cos(\phi)$. For simplicity, we assume that the free energy function depends on I_1, I_5, and I_7, and it is represented mathematically as:

$$W(I_1, I_5, I_7) = c(I_1 - 3) + \frac{g}{2} \sum_{i=5,7} (I_i - 1)^2 \tag{5.3}$$

with c and g as constitutive parameters of the model while the deformation invariants are defined as:

$$I_1 = (tr)\boldsymbol{C} \quad , \quad I_5 = \boldsymbol{M}(\boldsymbol{C}^2\boldsymbol{M}) \quad , \quad I_7 = \boldsymbol{M'}(\boldsymbol{C}^2\boldsymbol{M'}) \tag{5.4}$$

The invariants I_5 and I_7 are related to both fiber stretch and shearing [28]. In terms of stretches, these invariants are expressed as:

$$I_5 = I_7 = \lambda_z^4 \cos^2(\phi) + \lambda_\theta^4 \sin^2(\phi) \tag{5.5}$$

The Cauchy stress tensor for the chosen model is given by:

$$\begin{aligned} \sigma = &-q\boldsymbol{I} + 2W_1\boldsymbol{b} \\ &+ 2W_5(\boldsymbol{FM} \otimes \boldsymbol{bFM} + \boldsymbol{bFM} \otimes \boldsymbol{FM}) \\ &+ 2W_7(\boldsymbol{FM'} \otimes \boldsymbol{bFM'} + \boldsymbol{bFM'} \otimes \boldsymbol{FM'}) \end{aligned} \tag{5.6}$$

where $W_i = \frac{\partial W}{\partial I_i}$,$(i = 1, 5, 7)$ and q is the hydrostatic pressure under the assumption of incompressibility. For completeness, we indicate that when torsion is additionally applied (see [138, 154]), the deformation gradient is calculated explicitly (as long as the cylindrical geometry is kept with the deformation) as:

$$\boldsymbol{F} = \lambda_r e_r \otimes \boldsymbol{E}_R + \lambda_\theta e_\theta \otimes \boldsymbol{E}_\Theta + \lambda_z e_z \otimes \boldsymbol{E}_Z + \lambda_z \gamma e_\theta \otimes \boldsymbol{E}_Z \tag{5.7}$$

where we have defined $\gamma = \psi r$, in which ψ is the torsional deformation per unit deformed length, and λ_r, λ_θ. and λ_z are the principal stretches in the radial, azimuthal and axial

directions prior to application of the torsion. It is easy to check that under extension, inflation, and positive shearing the invariants I_5 and I_7 are greater than one. Once the torsion is applied λ_θ and λ_z are no longer principal stretches. Indeed, the application of the torsion will change the cylindrical geometry, but in those analytical analyses (see [138]) several parameters are adjusted accordingly to ensure that the circular cylindrical configuration is maintained with appropriate pressure, axial load, and torsional moment. In our numerical analysis that follows the purpose is indeed to get deformed configurations associated with bifurcation and post-bifurcation considering different scenarios of the problem at hand and not to keep the perfect circular cylindrical geometry. Results show a rich and great variety of solutions that are captured with the analysis provided. Nevertheless, in our simulations, the (initial) deformation prior to bifurcation is described and understood with the variables that have been provided in this Section. Alternative hyperelastic energy density forms for the modeling of soft biological tissue behavior are reviewed in [155]. Works such as [156–158]account for fibers in their works, but their considerations are restricted to fibers whose energy forms are modeled in terms of the invariants I_4 and I_6 that do account only for fiber elongation. In this chapter, the fibers account for both stretch and shear deformations, and we show how this mechanical behavior affects helical buckling of the considered tube.

5.3 Numerical application to extension, inflation, and torsion

In order to illustrate our modeling, we consider loading of the incompressible free energy function described before. We focus our attention on the structural system that consists of a cylindrical tube subjected to different loading cases. It is examined to understand the effects of axial loading, pressure, and twist angle on buckling patterns.

5.3.1 Geometry and discretization

We consider a thick-walled cylindrical tube of length $L = 43$ mm, diameter $D = 7.24$ mm and thickness T of 2 mm. This geometry is adapted from some initial dimensions of normal porcine carotid arteries that have been reported in [152, 159]. We employ reduced three-dimensional linear hybrid solid elements (C3D8RH in the ABAQUS notation) for the spatial discretization of the cylindrical geometry. The total number of finite elements in the thickness, azimuthal and axial direction are considered as 4, 32, and 200 respectively. A detailed view of the mesh can be seen in Fig. 5.1. We impose a fixed boundary in the axial direction at one end of the cylinder whereas at the other end, it is stretched and twisted axially using a kinematic coupling constraint. The rotation angle is applied gradually. The self-contact is also applied at the outer wall to avoid any surface penetration. More, in particular, the numerical simulation dealing with extension, inflation, and torsion of the tube is carried out in three steps with the following boundary conditions at the ends of the tube:

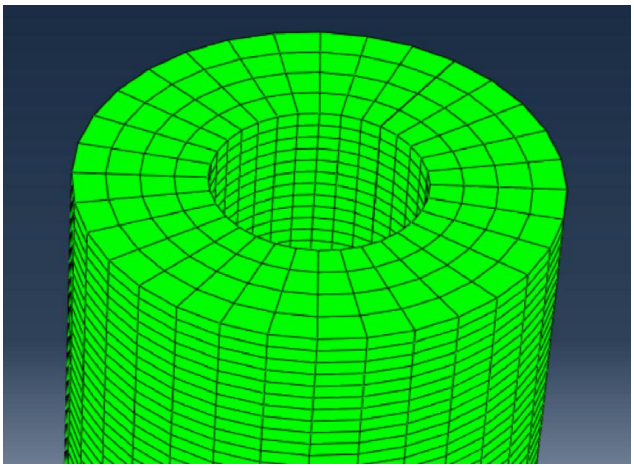

Figure 5.1: Spatial discretization of the tube.

1) In the first step of the simulation, the axial stretch (λ_z) is applied by imposing axial displacements at one end keeping zero axial displacements (pinned) at the other end while azimuthal displacement at both ends of the tube is not allowed. This is to obtain a deformed circular cylindrical geometry.

2) In the second step, internal pressure is gradually applied to the inner surface of the cylinder. Axial and azimuthal displacements at both ends of the tube are not allowed.

3) In the last step, an azimuthal rotation α is applied at one end of the tube (where stretch was applied in step 1 along z direction) keeping zero rotations in other directions. The other end of the tube is pinned. Kinematic coupling is enforced at the end of the cylinder in which rotation is allowed to eliminate any additional longitudinal extension of the cylinder. This is controlled by a node at the center of that end of the cylinder. Constraints are imposed on this particular node that prevents all its degrees of freedom except an imposed rotation about the cylinder axis. The constitutive parameters for the simulations have been taken accordingly from [152] and are summarized in Table 5.1.

Table 5.1: Constitutive parameters of an anisotropic model.

Parameters	Values	[Unit]
Density	1020	$kg.m^{-3}$
Neo-Hookean (c)	2.50	kPa
Anisotropic (g, ψ)	0.53, 38.3	kPa , degrees

This loading scenario gives rise to multiple bifurcation configurations depending on the amount of loading as well as the path of loading. Given the broad scope of the computational framework, we consider two main situations in this section. Firstly, bifurcation is captured under just extension and inflation. A critical buckling pressure is associated with bifurcation, which is bending. Secondly, bifurcation is captured under extension inflation and torsion for a value of pressure less than the so-called Critical Buckling Pressure. Under these conditions,

a Critical Torque is associated with bifurcation, which is mainly helical buckling. After the analysis of these two cases, a more complex loading situation is studied,which gives rise to shapes such as looping and wringing.

5.3.2 Identification of critical buckling pressure and torque

We now detail the numerical strategies to identify the critical buckling pressure and critical buckling torque. The analysis procedure is explained in what follows.

Critical pressure under extension and inflation - curving scenario

The critical pressure is identified by using the modified Riks analysis procedure (ABAQUS terminology for the arc length method) [160]. It is a very efficient method for solving non-linear systems of equations when the problem under consideration exhibits snapping behavior. The concept of time is replaced by arc length in this procedure. This method postulates a simultaneous variation in both the displacements and the load proportional factor (LPF) and is an indicator of the applied load and the evolution of deformation respectively. It is a two-step simulation process. First, we apply an axial stretch λ_z, followed by internal pressure P at the inner surface. The critical pressure (P_{cr} is established by following the initiation of lateral movement of the tube. Subsequently, post-bifurcation analysis is done introducing a geometric imperfection. This is necessary to obtain a smooth solution path. The scale of imperfection is applied based on the first eigen-mode and the factor is a maximum magnitude of 5×10^{-3} times the radius. The numerical calculations are for different axial stretch values in the domain $\lambda_z \in [1.1, 1.7]$ at a final pressure of 50 mm of Hg pressure. Deformed configurations in post-bifurcation analysis at the last converged time step are shown in Fig. 5.2.

For all values of λ_z bifurcation is given by bending (curving). Furthermore, the onset of bending is associated with the mode $n = 1$. This is consistent with our previous studies on the bifurcation of tubes [7]. For $\lambda_z = 1.1$ our computations show that the pressure associated with bifurcation is 34 mm of Hg. Values of the LPF vs. arc length in Fig. 5.2 indicate that greater values of λ_z are associated with greater values of pressure for bifurcation.

Critical Torque (for $P < P_{cr}$)

In addition to stretch and inflation, we apply twist and quantify its effect on the mode of bifurcation. This is performed now for pressure values less than the critical pressure. Two representative cases are detailed:

1) Case I - No pressure of inflation.

2) Case II - A pressure value of 20 mm Hg (less than the critical pressure value associated with bifurcation for the axial stretches considered).

In general, the application of the torsion will change the initial circular cylindrical geometry, but, as it is recognized in [138], the length and internal radius of the tube during torsion at zero pressure can be tuned based on the application.

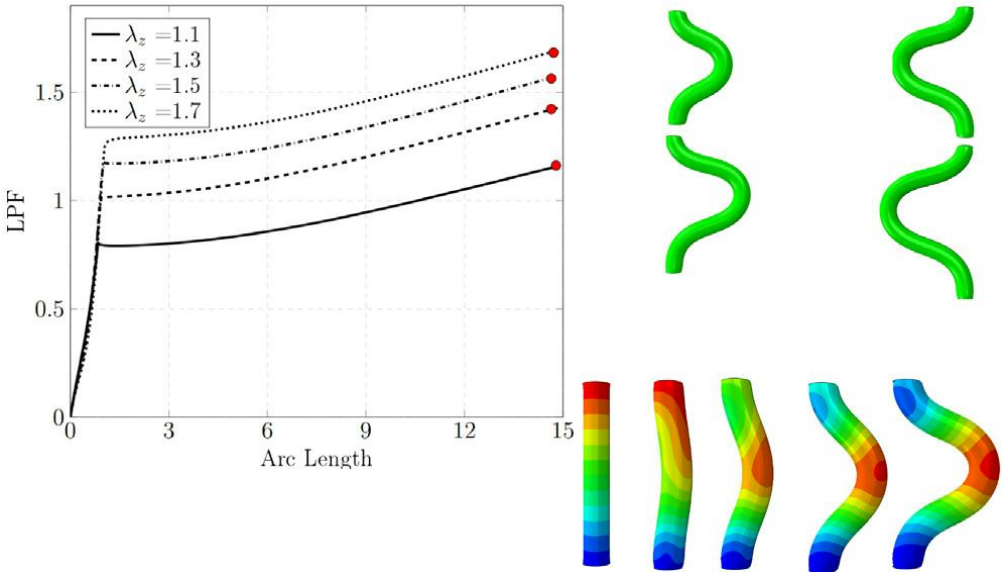

Figure 5.2: Values of the LPF vs. arc length showing the inflection point after which the tube starts to move in a lateral direction (bending bifurcation). The deformed states at the last converged time step are shown at the top right of the Figure along with the history of configurations (colors showing the displacement magnitude with red as maximum and blue as minimum) for $\lambda_z = 1.1$ at the bottom right.

It is clear that while we do not try now to keep the perfect circular cylindrical geometry, it is important to understand the coupling of torsion and pressure with the length of the tube. The analyses of these two cases (1 and 2) open a variety of results, as it is shown in what follows, that unravel the mechanisms at hand. There are three simulation steps to identify the critical twisting moment. An axial stretch λ_z at one end is first applied followed by an internal pressure P in the second step. In the last step, we apply rotation gradually as it was explained previously. Values of the torque vs. rotation are shown in Fig. 5.3 for all cases.

The torque is obtained using ABAQUS as a field output where rotation is applied. The value of rotation for (helical) buckling in each case is presented in Table 5.2.

Table 5.2: Normalized moment and critical rotation associated with (helical) bifurcation at the peak point (just before the softening) for the plots shown in Fig. 5.3.

Case 1	$\lambda_z = 1.1$	$\lambda_z = 1.3$	$\lambda_z = 1.5$	$\lambda_z = 1.7$
$M_z/(2cTD^2)$	0.59	0.53	.0.47	0.43
$\alpha D/L$	2.05	2.28	2.43	2.53
Case 2	$\lambda_z = 1.1$	$\lambda_z = 1.3$	$\lambda_z = 1.5$	$\lambda_z = 1.7$
$M_z/(2cTD^2)$	0.72	0.78	.0.71	0.62
$\alpha D/L$	2.70	3.21	3.51	3.74

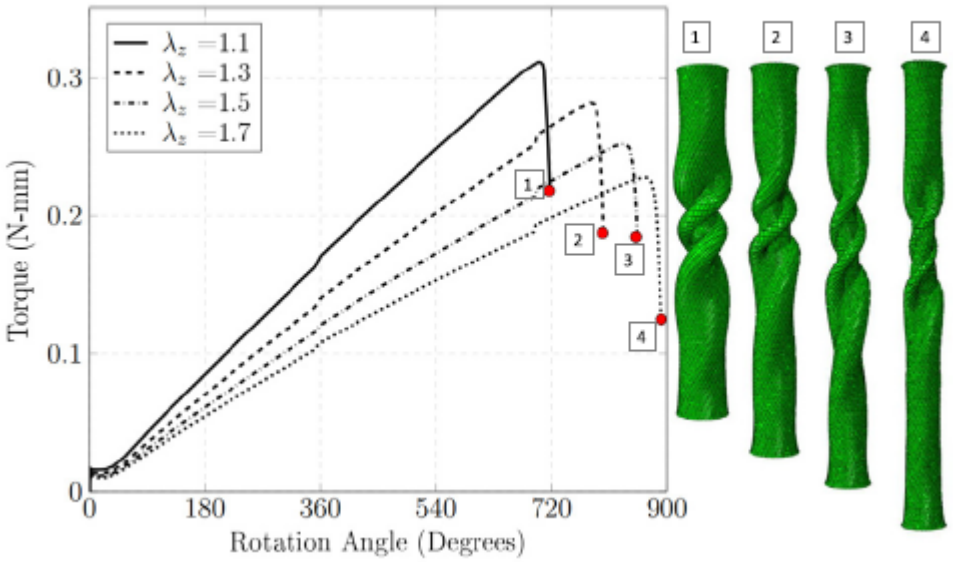

(a) Case 1: Torque vs. rotation angle for $\lambda_z = 1.1 - 1.7$

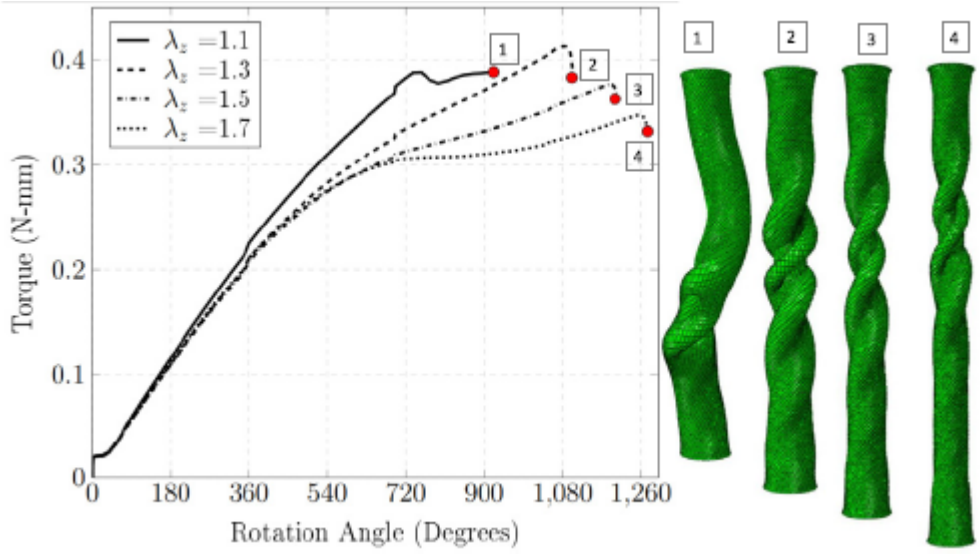

(b) Case 2: Torque vs. rotation angle for $\lambda_z = 1.1 - 1.7$

Figure 5.3: Variations of axial torque and the deformed configurations with rotation angle for a given pressure (a) at a pressure of 0 mm Hg and (b) 20 mm Hg for different values of the axial stretch. The deformed states at the last converged time step are shown at the right of the Figure for both cases.

We find for Case I that the torque increases linearly with rotation angle until a sudden drop occurs, see Fig. 5.3a, which gives the onset of helical bifurcation in accordance with parallel analyses. The deformed configuration is summarized in Fig. 5.3a (top) where twisted kink can be seen approximately at the middle location of the model for values $\lambda_z in [1.1, 1.7]$. The critical buckling torque decreases whereas the critical twist angle increases by increasing the axial stretch. For Case 2, we observe the bending of the tube for $\lambda_z = 1.1$, which results

in kinking together with bending, whereas just helical buckling follows for the other stretch values ($\lambda_z = 1.3, 1.5, 1.7$) as it is depicted in Fig. 5.3b (bottom). Furthermore, as it is given in Fig. 5.3 for Case 2, values of torque vs rotation are nonlinear. The new situation is found for $\lambda_z = 1.1$ of Case 2. Two bifurcation modes are coupled as the twist angle is applied: bending follows helical buckling. It is clear that the combination of pressure and axial stretch has a significant effect on both critical buckling torque and twist angle.

Helical buckling (for $P > P_{cr}$)

When a tube is stretched, pressurized and sufficiently twisted, it becomes unstable, coils up helically and generates a range of localized and self-contacting structures. Such tortuous shapes can be observed in clinical patients [151]. While this behavior has been well characterized experimentally, numerical modeling of in vivo mechanical loading is not so straightforward. In this section, localized buckling modes that arise due to large amounts of twisting are captured. These morphologies are characterized by simulating several loading conditions for a cylindrical tube. With respect to the inflation pressure. Results under the combined loading of extension, pressure, and torsion demonstrate various buckling patterns such as kinking, coiling, looping, and winding. More in particular, these localized deformations are simulated using a pressure value of 50 mm Hg and a range of axial stretches ($\lambda_z \in [1.1, 1.7]$). Results are shown for in Figures 5.4 to 5.7.

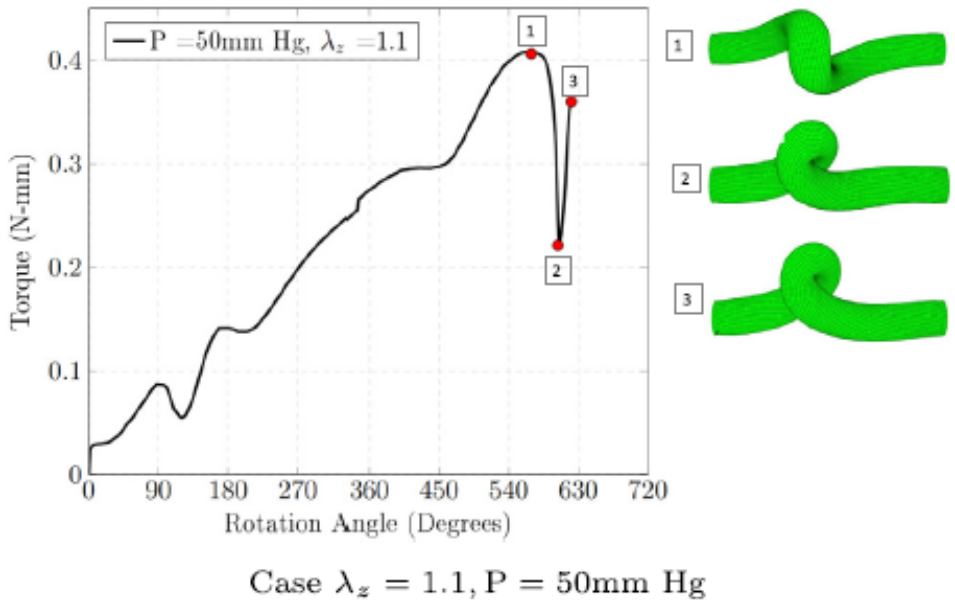

Figure 5.4: Variations of axial torque and the deformed configurations with rotation angle for a given axial stretch ratio of 1.1 in an artery at a pressure of 50 mm Hg. The deformed states are shown at the right of the Figure.

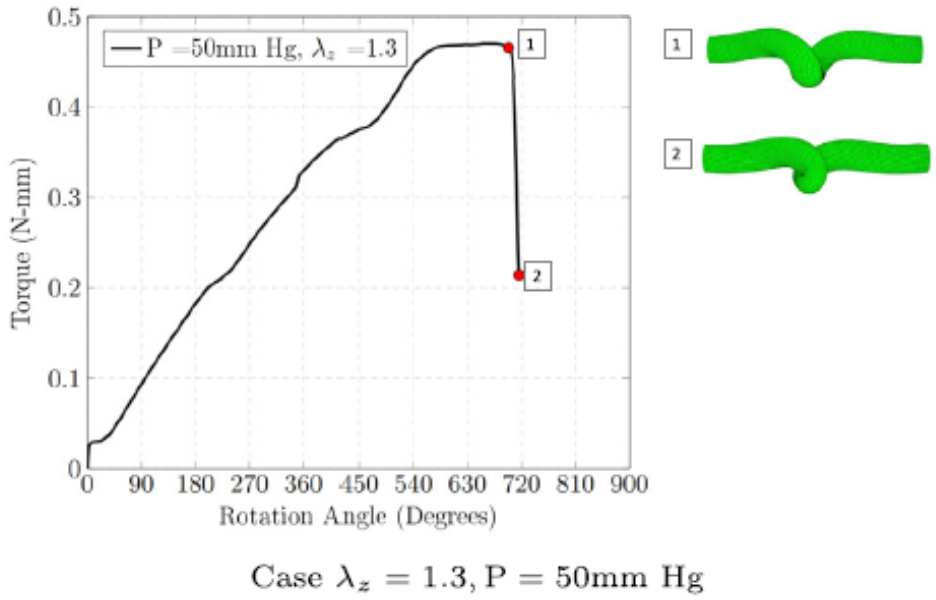

Figure 5.5: Variations of axial torque and the deformed configurations with rotation angle for a given axial stretch ratio of 1.3 in an artery at a pressure of 50 mm Hg. The deformed states are shown at the right of the Figure.

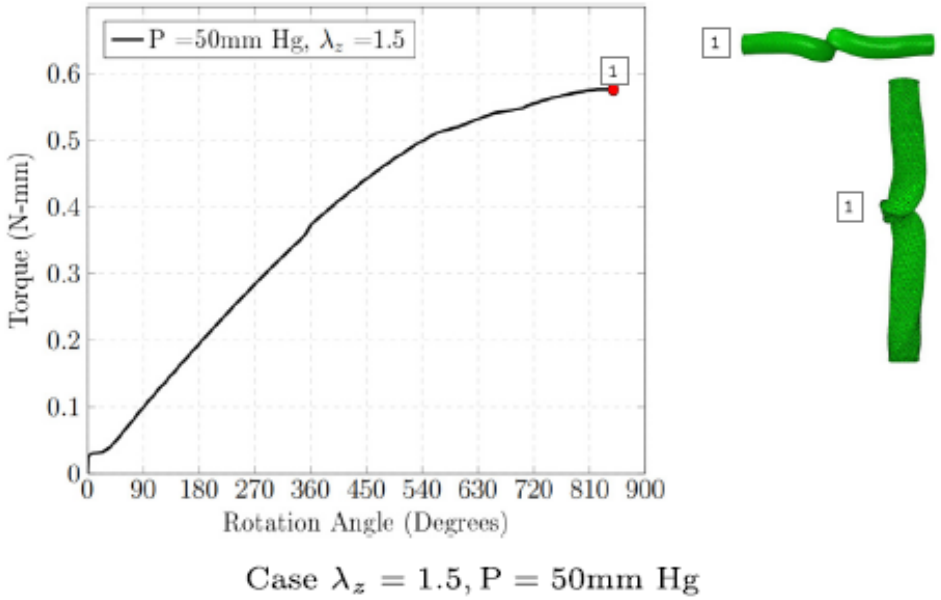

Figure 5.6: Variations of axial torque and the deformed configurations with rotation angle for a given axial stretch ratio of 1.5 in an artery at a pressure of 50 mm Hg. The deformed states are shown at the right of the Figure.

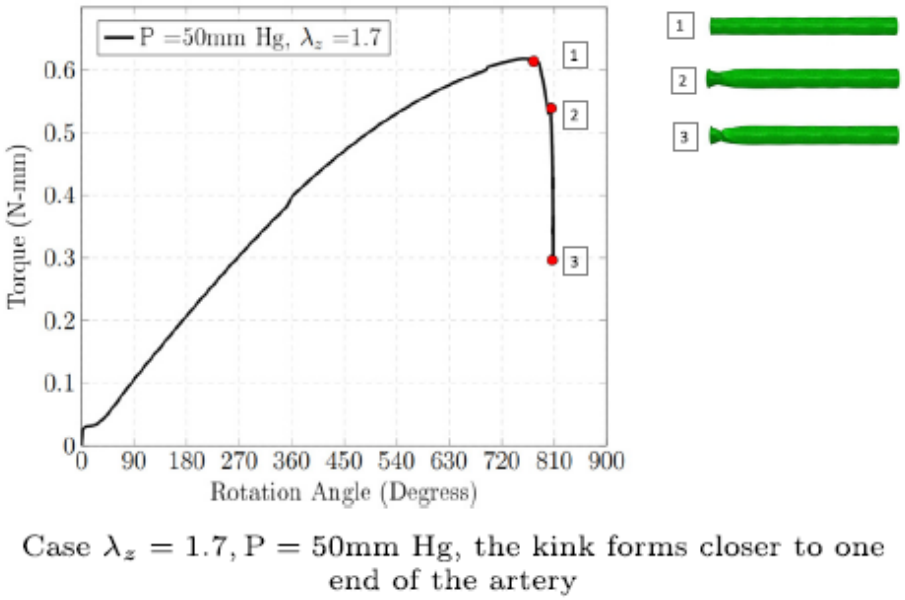

Figure 5.7: Variations of axial torque and the deformed configurations with rotation angle for a given axial stretch ratio of 1.7 in an artery at a pressure of 50 mm Hg. The deformed states are shown at the right of the Figure.

The history of configurations given by 1 to 3 in Fig. 5.4 for $\lambda_z = 1.1$ shows that helical coiling is developed (configuration 1), firstly, as a result of bending bifurcation due to pressure, followed by a twist. The helical coiling develops into looping and winding, configurations 2 and 3, respectively. This is the situation for $\lambda_z = 1.3$ as it is shown in Fig. 5.5. But for greater values of the axial stretch, the bifurcation scenario changes. In Fig. 5.7 the configurations show (helical) kinking bifurcation. An intermediate situation between the case $lambda_z = 1.3$and the case $\lambda_z = 1.7$ is shown in Fig. 5.6 for $\lambda_z = 1.5$

5.3.3 Chapter summary

Helical buckling in arteries is extremely unstable. This has profound biomedical implications because these findings relate directly to arteries. Our study provides a numerical methodology to explain the complex geometrical patterns of a tube when it is stretched, inflated, and twisted. The applicability of the current formulation has been examined using a series of numerical simulations focused on the analysis of the effect of several loading conditions. We depict the localized bifurcation modes for a range of applied axial stretches, torques, and inflation pressures. Helical buckling is considered to be one cause of arterial rupture and it is important to understand tortuosity and associated mechanisms. Regarding tortuosity, it is considered that twisting could contribute to some vessels such as carotids and superficial femoral. It remains for future work to explore further the parametric space of cylindrical structures to capture, among other things, the transition from bifurcation to rupture, which can be useful for future vascular implant designs and disease treatments. Instability modeling works often restrict their considerations to a time-independent material behavior. Nevertheless, soft tissue components may undergo changes that depend on various complex biological, chemical, and physical

processes that result, for example, in the degradation of constituents [161], growths [158] or in tissue renewal [162]. The article [163] has shown that mechano-sensitive fiber-remodeling affects the inflation behavior of a pressurized cylinder. The stable inflation under fiber remodeling in [163] ignores the initiation of instabilities, which remains a challenge for future modeling approaches. Several works have been done on nonlinear elasticity instabilities of cylinders (see [164, 165, 165, 165–177]) and fiber reinforced cylinders (refer to [33, 46, 77, 116, 178–182]). Future directions for the investigation of instabilities in soft tissue models may also invoke the consideration of porous media and the influence of the liquid phase [107].

Chapter 6

Conclusions

In this thesis, mechanical modeling of residually stressed hyperelastic materials is carried out. Numerical frameworks for this objective are developed. This work is divided into three categories according to their principal application to Aneurysm.

To determine the onset of bifurcation instabilities is generally a challenge in soft structures since Bifurcation and post bifurcation results show a very different qualitative behavior for the structures. Moreover, the use of strain-softening models may lead to snap-back behavior on a structural level. This observation, which has probably been made first by Crisfield [2], implies that structures composed of strain-softening material cannot always be analyzed using standard displacement control. In this work, a methodology to study bulging and bending of stretched and inflated cylinders was utilized based on the modified Riks finite element analysis that assumes three-dimensional residual stress field in which there exist axial, as well as shear components.

Furthermore, numerical analyses were carried out to capture bifurcation and post-bifurcation of residually stressed double layered thick-walled tubes subjected to axial pre-stretch combined with inflation pressure. Moreover, helical stability experienced by elastic cylinders was investigated using numerical methods. A numerical framework to implement residual stresses that are in equilibrium in the reference configuration and absence of external loads has been utilized by means of a commercial finite element code. It has been shown that residual stresses have considerable qualitative effects on the results compared to the model with no residual stress. It seems of great importance to consider residual stresses to model biological tissues such as arteries and their associated cardiovascular diseases such as aneurysms. It is expected that other residual stress fields and boundary conditions may give rise to other modes of bifurcation. The presented framework here can be easily modified include other conditions.

Various factors influence the critical pressure and axial stretch associated with mechanical buckling. Initially, the impact of residual stresses on the bifurcation behavior of tubes under the applied load has been examined. Two bifurcation modes, Bending and Bulging, have been identified. Bending occurs in scenarios with minimal axial pre-stretches, while Bulging is anticipated when significant axial pre-stretch values are applied. Investigations into the

bulging bifurcation and post-bifurcation phenomena have been conducted. It has been noted that increasing axial pre-stretch leads to a decrease in the pressure associated with bulging bifurcation. Additionally, the positive strength of residual stress, inducing tensile stresses on the outer surface and compressive stresses on the inner surface of the cylinder's wall, results in reduced pressure at the bulging instability, whereas negative strength has the opposite effect. The impact of the weight parameter on residual stress invariants reveals that when it is zero, residual stresses exert more influence on model behavior. Post-bifurcation analysis of bulging reveals a catastrophic instability where the model cannot sustain additional pressure. The bulge is observed to uniformly and symmetrically expand radially, akin to fusiform aneurysm rupture. Moreover, stress analysis at bulging bifurcation points out stress concentration in the bulging area. In cases of Bending, graphs illustrate that while residual stresses play a role in triggering bending instability, their effect on the associated pressure is not significant. It is also demonstrated that by imposing azimuthal constraints on displacements on the outer/inner surface of the cylinder, bifurcation can be restricted solely to bulging, thereby avoiding bending. This excerpt highlights the significant impact of bending bifurcation. Increasing the axial pre-stretch results in this bifurcation occurring at higher pressures, extending to a transitional range where bending occurs at pressures very close to bulging. Within this transitional range, a change in the bulge's shape is observed, but there is no significant effect on the associated pressure, resembling the characteristics of a saccular aneurysm of the aorta. Analysis of the post-bifurcation phase of this instability reveals a ductile behavior, indicating that the structure can withstand higher pressures in subsequent motion after bifurcation onset. Loading persists until a one-sided bulge, consistent with a saccular aneurysm, is formed. Furthermore, the maximum inflation pressure associated with this scenario is lower than that of similar cases where bending is prevented (through azimuthal displacement restrictions). This suggests the potential for delayed aneurysm formation if bending is not allowed.

Furthermore, the study addressed the helical stability in inelastic cylinders. A doubly fiber-reinforced, in-compressible, nonlinear elastic tube subjected to axial loading, internal pressure, and twist was examined using a numerical approach based on the modified Riks (quasi-static) procedure. When subjected to such loading, which qualitatively resemble physiological conditions for arteries, vessels exhibit tortuous shapes and a variety of topologically and geometrically complex morphologies. These configurations can become highly unstable due to the nonlinear interaction among multiple bifurcation modes, encompassing geometry, material properties, and self-contact phenomena. This study aimed to simulate such intricate configurations using a thick-walled cylindrical tube. In the bio-mechanics community, these complex morphologies are commonly referred to as helical coiling, looping, and winding. It was demonstrated that these bifurcations are highly sensitive to applied pressure, axial stretch, and the degree of twist. The illustration of helical buckling was further provided by considering an anisotropic constitutive model incorporating both fiber stretching and fiber shearing, which extends previous analyses that solely accounted for fiber stretching. Lastly, the investigation of axial and azimuthal stresses along the cylinder's length demonstrates excellent concordance with the criterion established by analytical analysis. The residual stress field in this study comprises solely azimuthal and radial components.

Bibliography

[1] J. Rodríguez and J. Merodio. A new derivation of the bifurcation conditions of inflated cylindrical membranes of elastic material under axial loading. application to aneurysm formation. *Mech. Res. Commun.*, 38:203–210, 2010.

[2] M. A. Crisfield. An arc-length method including line searches and accelerations. *International Journal for Numerical Methods in Engineering*, 19(9):1269–1289, September 1983.

[3] Hasan Demirkoparan and Thomas J. Pence. Swelling of an internally pressurized nonlinearly elastic tube with fiber reinforcing. *International Journal of Solids and Structures*, 44(11):4009–4029, 2007.

[4] Thomas J. Pence and Hungyu Tsai. Swelling-induced microchannel formation in nonlinear elasticity*. *IMA Journal of Applied Mathematics*, 70(1):173–189, 02 2005.

[5] Raymond William Ogden. Large deformation isotropic elasticity – on the correlation of theory and experiment for incompressible rubberlike solids. *Proceedings of the Royal Society of London. A. Mathematical and Physical Sciences*, 326(1567):565–584, February 1972.

[6] Majid Shahzad, Ali Kamran, Muhammad Zeeshan Siddiqui, and Muhammad Farhan. Mechanical characterization and fe modelling of a hyperelastic material. *Materials Research*, 18(5):918–924, October 2015.

[7] H. Dehghani, D. Desena-Galarza, N.K. Jha, J. Reinoso, and J. Merodio. Bifurcation and post-bifurcation of an inflated and extended residually-stressed circular cylindrical tube with application to aneurysms initiation and propagation in arterial wall tissue. *Finite Elements in Analysis and Design*, 161:51–60, September 2019.

[8] Masoud Hejazi, York Hsiang, and A. Srikantha Phani. Fate of a bulge in an inflated hyperelastic tube: theory and experiment. *Proceedings of the Royal Society A: Mathematical, Physical and Engineering Sciences*, 477(2247), March 2021.

[9] A. Font, N. K. Jha, H. Dehghani, J. Reinoso, and J. Merodio. Modelling of residually stressed, extended and inflated cylinders with application to aneurysms. *Mech. Res. Commun.*, 111:103643, 2021.

[10] Sohan Singh Hayreh, Gary E. Servais, and Prem Singh Virdi. Retinal arteriolar changes in malignant arterial hypertension. *Ophthalmologica*, 198(4):178–196, 1989.

[11] N C B B Taarnhj, I C Munch, B Sander, L Kessel, J L Hougaard, K Kyvik, T I A Sørensen, and M Larsen. Straight versus tortuous retinal arteries in relation to blood pressure and genetics. *British Journal of Ophthalmology*, 92(8):1055–1060, 2008.

[12] Zane S. Jackson, Dorota Dajnowiec, Avrum I. Gotlieb, and B. Lowell Langille. Partial off-loading of longitudinal tension induces arterial tortuosity. *Arteriosclerosis, Thrombosis, and Vascular Biology*, 25(5):957–962, May 2005.

[13] Zhiqiang Fan, Peter Eichhubl, and Julia F. W. Gale. Geomechanical analysis of fluid injection and seismic fault slip for the mw4.8 timpson, texas, earthquake sequence. *Journal of Geophysical Research: Solid Earth*, 121(4):2798–2812, April 2016.

[14] A. H. Corneliussen and R. T. Shield. Finite deformation of elastic membranes with application to the stability of an inflated and extended tube. *Archive for Rational Mechanics and Analysis*, 7(1):273–304, January 1961.

[15] D. Haughton and R. Ogden. Bifurcation of inflated circular cylinders of elastic material under axial loading-II. exact theory for thick-walled tubes. *J. Mech. Phys. Solids*, 27:489–512, 1979.

[16] A. A. Alhayani, J. A. Giraldo, J. Rodriguez, and J. Merodio. Computational modelling of bulging of inflated cylindrical shells applicable to aneurysm formation and propagation in arterial wall tissue. *Finite Elem. Anal. Des.*, 73:20–29, 2013.

[17] M. El Hamdaoui, J. Merodio, R. W. Ogden, and J. Rodríguez. Finite elastic deformations of transversely isotropic circular cylindrical tubes. *Int. J. Solids Struct.*, 51:1188–1196, 2014.

[18] M. El Hamdaoui and J. Merodio. Azimuthal shear of doubly fibre-reinforced, non-linearly elastic cylindrical tubes. *J. Eng. Math.*, 95:347–357, 2015.

[19] Y. B. Fu, J. L. Liu, and G. S. Francisco. Localized bulging in an inflated cylindrical tube of arbitrary thickness: the effect of bending stiffness. *J. Mech. Phys. Solids*, 90:45–60, 2016.

[20] Y. Ye, Y. Liu, and Y. Fu. Weakly nonlinear analysis of localized bulging of an inflated hyperelastic tube of arbitrary wall thickness. *J. Mech. Phys. Solids*, 135:103804, 2020.

[21] Anne Hoger. On the residual stress possible in an elastic body with material symmetry. *Arch. Ration. Mech. Anal.*, 88(3):271–289, 1985.

[22] J Merodio. On constitutive equations for fiber-reinforced nonlinearly viscoelastic solids. *Mech. Res. Commun.*, 33(6):764–770, November 2006.

[23] José Merodio, Giuseppe Saccomandi, and Ivonne Sgura. The rectilinear shear of fiber-reinforced incompressible non-linearly elastic solids. *Int. J. Non Linear Mech.*, 42(2):342–354, March 2007.

[24] J Merodio and J M Goicolea. On thermodynamically consistent constitutive equations for fiber-reinforced nonlinearly viscoelastic solids with application to biomechanics. *Mech. Res. Commun.*, 34(7-8):561–571, October 2007.

[25] J. Merodio and D.M. Haughton. Bifurcation of thick-walled cylindrical shells and the mechanical response of arterial tissue affected by marfan's syndrome. *Mechanics Research Communications*, 37(1):1–6, January 2010.

[26] J Merodio. A note on strong ellipticity for transversely isotropic linearly elastic solids. *Quart. J. Mech. Appl. Math.*, 56(4):589–591, November 2003.

[27] J Merodio and R W Ogden. Instabilities and loss of ellipticity in fiber-reinforced compressible non-linearly elastic solids under plane deformation. *Int. J. Solids Struct.*, 40(18):4707–4727, September 2003.

[28] J. Merodio and R. W. Ogden. Mechanical response of fiber-reinforced incompressible non-linearly elastic solids. *Int. J. Non Linear Mech.*, 40:213–227, 2005.

[29] J Merodio and R W Ogden. On tensile instabilities and ellipticity loss in fiber-reinforced incompressible non-linearly elastic solids. *Mech. Res. Commun.*, 32(3):290–299, May 2005.

[30] J Merodio and R W Ogden. The influence of the invariant on the stress–deformation and ellipticity characteristics of doubly fiber-reinforced non-linearly elastic solids. *Int. J. Non Linear Mech.*, 41(4):556–563, May 2006.

[31] José Merodio and Ray W. Ogden. Extension, inflation and torsion of a residually stressed circular cylindrical tube. *Continuum Mechanics and Thermodynamics*, 28(1–2):157–174, January 2015.

[32] José Merodio and Raymond Ogden. Finite deformation elasticity theory. In *Constitutive Modelling of Solid Continua*, Solid mechanics and its applications, pages 17–52. Springer International Publishing, Cham, 2020.

[33] José Merodio and Ray W Ogden. Instabilities associated with loss of ellipticity in fiber-reinforced nonlinearly elastic solids. In *Computational and Experimental Methods in Structures*, Computational and experimental methods in structures, pages 295–332. WORLD SCIENTIFIC (EUROPE), April 2023.

[34] J Merodio and K R Rajagopal. On constitutive equations for anisotropic nonlinearly viscoelastic solids. *Math. Mech. Solids*, 12(2):131–147, April 2007.

[35] Jose Merodio and Giuseppe Saccomandi. Remarks on cavity formation in fiber-reinforced incompressible non-linearly elastic solids. *Eur. J. Mech. A Solids*, 25(5):778–792, September 2006.

[36] José Merodio, Ray W Ogden, and Javier Rodríguez. The influence of residual stress on finite deformation elastic response. *Int. J. Non Linear Mech.*, 56:43–49, November 2013.

[37] J Merodio and R W Ogden. Remarks on instabilities and ellipticity for a fiber-reinforced compressible nonlinearly elastic solid under plane deformation. *Quart. Appl. Math.*, 63(2):325–333, February 2005.

[38] J Merodio and R W Ogden. On the equivalence of strong ellipticity in the material and spatial settings of finite elasticity. *Z. Angew. Math. Phys.*, 57(6):1096–1101, November 2006.

[39] J Merodio and R W Ogden. Tensile instabilities and ellipticity in fiber-reinforced compressible nonlinearly elastic solids. *Int. J. Eng. Sci.*, 43(8-9):697–706, May 2005.

[40] M H B M Shariff and J Merodio. Nonlinear rate-dependent spectral constitutive equation for viscoelastic solids with residual stresses. *J. Eng. Math.*, 129(1), August 2021.

[41] M H B M Shariff, R Bustamante, and J Merodio. Rate type constitutive equations for fiber reinforced nonlinearly vicoelastic solids using spectral invariants. *Mech. Res. Commun.*, 84:60–64, September 2017.

[42] M H B M Shariff, R Bustamante, and J Merodio. Nonlinear electro-elastic bodies with residual stresses: spectral formulation. *Quart. J. Mech. Appl. Math.*, 71(4):485–504, November 2018.

[43] M H B M Shariff, R Bustamante, and J Merodio. A nonlinear constitutive model for a two preferred direction electro-elastic body with residual stresses. *Int. J. Non Linear Mech.*, 119(103352):103352, March 2020.

[44] Mhbm Shariff, Roger Bustamante, and Jose Merodio. A nonlinear electro-elastic model with residual stresses and a preferred direction. *Math. Mech. Solids*, 25(3):838–865, March 2020.

[45] M H B M Shariff, J Merodio, and R Bustamante. Nonlinear elastic constitutive relations of residually stressed composites with stiff curved fibres. *Appl. Math. Mech.*, 43(10):1515–1530, October 2022.

[46] Mohd Halim Bin Mohd Shariff, Jose Merodio, Roger Bustamante, and Aymen Laadhari. A non-second-gradient model for nonlinear electroelastic bodies with fibre stiffness. *Symmetry (Basel)*, 15(5):1065, May 2023.

[47] Mohd Halim Bin Mohd Shariff and Jose Merodio. Residually stressed fiber reinforced solids: A spectral approach. *Materials (Basel)*, 13(18):4076, September 2020.

[48] I Sevostianov, A Trofimov, J Merodio, R Penta, and R Rodriguez-Ramos. Connection between electrical conductivity and diffusion coefficient of a conductive porous material filled with electrolyte. *Int. J. Eng. Sci.*, 121:108–117, December 2017.

[49] Jose Merodio and Thomas J Pence. Kink surfaces in a directionally reinforced neo-hookean material under plane deformation: I. mechanical equilibrium. *Journal of elasticity and the physical science of solids*, 62(2):119–144, February 2001.

[50] D. M. Haughton and J. Merodio. The elasticity of arterial tissue affected by Marfan's syndrome. *Mech. Res. Commun.*, 36:659–668, 2009.

[51] O L Cruz-González, D Guinovart-Sanjuán, R Rodríguez-Ramos, J Bravo-Castillero, R Guinovart-Díaz, J Merodio, R Penta, José A Otero, S Dumont, F Lebon, and F J Sabina. An approach for modeling non-ageing linear viscoelastic composites with general periodicity. *Compos. Struct.*, 223(110927):110927, September 2019.

[52] R I Cukier, C M Fortuin, K E Shuler, A G Petschek, and J H Schaibly. Study of the sensitivity of coupled reaction systems to uncertainties in rate coefficients. I theory. *J. Chem. Phys.*, 59(8):3873–3878, October 1973.

[53] R I Cukier, H B Levine, and K E Shuler. Nonlinear sensitivity analysis of multiparameter model systems. *J. Comput. Phys.*, 26(1):1–42, January 1978.

[54] H Dehghani, R Penta, and J Merodio. The role of porosity and solid matrix compressibility on the mechanical behavior of poroelastic tissues. *Mater. Res. Express*, 6(3):035404, December 2018.

[55] H Dehghani, I Noll, R Penta, A Menzel, and J Merodio. The role of microscale solid matrix compressibility on the mechanical behaviour of poroelastic materials. *Eur. J. Mech. A Solids*, 83(103996):103996, September 2020.

[56] Michel Destrade and Jose Merodio. Compression instabilities of tissues with localized strain softening. *Int. J. Appl. Mech.*, 03(01):69–83, March 2011.

[57] M El Hamdaoui, J Merodio, and R W Ogden. Two-phase piecewise homogeneous plane deformations of a fibre-reinforced neo-hookean material with application to fibre kinking and splitting. *J. Mech. Phys. Solids*, 143(104091):104091, October 2020.

[58] Aleksandra Fortier, Vikranth Gullapalli, and Reza A Mirshams. Review of biomechanical studies of arteries and their effect on stent performance. *Int. J. Cardiol. Heart Vessels*, 4:12–18, September 2014.

[59] D Fraedrich and A Goldberg. A methodological framework for the validation of predictive simulations. *Eur. J. Oper. Res.*, 124(1):55–62, July 2000.

[60] H Christopher Frey and Sumeet R Patil. Identification and review of sensitivity analysis methods. *Risk Anal.*, 22(3):553–578, June 2002.

[61] D Guinovart-Sanjuán, R Rodríguez-Ramos, R Guinovart-Díaz, J Bravo-Castillero, F J Sabina, J Merodio, F Lebon, S Dumont, and A Conci. Effective properties of regular elastic laminated shell composite. *Compos. B Eng.*, 87:12–20, February 2016.

[62] D Guinovart-Sanjuán, K Vajravelu, R Rodríguez-Ramos, R Guinovart-Díaz, J Bravo-Castillero, F Lebon, F J Sabina, and J Merodio. Effective predictions of heterogeneous flexoelectric multilayered composite with generalized periodicity. *Int. J. Mech. Sci.*, 181(105755):105755, September 2020.

[63] David Guinovart-Sanjuán, Kuppalapalle Vajravelu, Reinaldo Rodríguez-Ramos, Raúl Guinovart-Díaz, Federico J Sabina, and Jose Merodio. Simple closed-form expressions for the effective properties of multilaminated flexoelectric composites. *J. Eng. Math.*, 127(1), April 2021.

[64] David Guinovart-Sanjuán, Jose Merodio, Juan Carlos López-Realpozo, Kuppalapalle Vajravelu, Reinaldo Rodríguez-Ramos, Raúl Guinovart-Díaz, Julián Bravo-Castillero, and Federico J Sabina. Asymptotic homogenization applied to flexoelectric rods. *Materials (Basel)*, 12(2):232, January 2019.

[65] Jon C Helton. Uncertainty and sensitivity analysis techniques for use in performance assessment for radioactive waste disposal. *Reliab. Eng. Syst. Saf.*, 42(2-3):327–367, January 1993.

[66] L. Dorfmann and R. W. Ogden. The effect of residual stress on the stability of a circular cylindrical tube. *J. Eng. Math.*, 127:9, 2021.

[67] A. Melnikov, R. W. Ogden, L. Dorfmann, and J. Merodio. Bifurcation analysis of elastic residually-stressed circular cylindrical tubes. *Int. J. Solids Struct.*, 226-227:111062, 2021.

[68] A. Melnikov and J. Merodio. Stability analysis of an inflated, axially extended, residually stressed circular cylindrical tube. *J. Appl. Comput. Mech.*, 9:834–847, 2023.

[69] H. Topol, M. J. Al-Chlaihawi, H. Demirkoparan, and J. Merodio. Bifurcation of fiber-reinforced cylindrical membranes under extension, inflation, and swelling. *J. Appl. Comput. Mech.*, 9:113–128, 2023.

[70] P. Barzó, A. Marmarou, P. Fatouros, K. Hayasaki, and F. Corwin. Contribution of vasogenic and cellular edema to traumatic brain swelling measured by diffusion-weighted imaging. *J. Neurosurg.*, 87:900–907, 1997.

[71] D. D. D'Lima, S. Hashimoto, P. C. Chen, C. W. Colwell, Jr., and M. K. Lotz. Impact of mechanical trauma on matrix and cells. *Clin. Orthop. Relat. Res.*, 391:S90–S99, 2001.

[72] K. J. Tracey. The inflammatory reflex. *Nature*, 420:853–859, 2002.

[73] T. J. Pence and H. Tsai. Swelling-induced cavitation of elastic spheres. *Math. Mech. Solids*, 11:527–551, 2006.

[74] R. G. M. van der Sman. Hyperelastic models for hydration of cellular tissue. *Soft Matter*, 11:7579–7591, 2015.

[75] H. Demirkoparan and J. Merodio. Bulging bifurcation of inflated circular cylinders of doubly fiber-reinforced hyperelastic material under axial loading and swelling. *Math. Mech. Solids*, 22:666–682, 2017.

[76] H. Demirkoparan and J. Merodio. Swelling and axial propagation of bulging with application to aneurysm propagation in arteries. *Math. Mech. Solids*, 25:1459–1471, 2020.

[77] Murtadha J. Al-Chlaihawi, Heiko Topol, Hasan Demirkoparan, and José Merodio. On prismatic and bending bifurcations of fiber-reinforced elastic membranes under swelling with application to aortic aneurysms. *Mathematics and Mechanics of Solids*, 28(1):108–123, December 2021.

[78] H. Topol, M. J. Al-Chlaihawi, H. Demirkoparan, and J. Merodio. Bulging initiation and propagation in fiber-reinforced swellable Mooney-Rivlin membranes. *J. Eng. Math.*, 128:8, 2021.

[79] G. A. Holzapfel, T. C. Gasser, and R. W. Ogden. A new constitutive framework for arterial wall mechanics and a comparative study of material models. *J. Elast.*, 61:1–48, 2000.

[80] H. Demiray. A note on the elasticity of soft biological tissues. *J. Biomech.*, 5:309–311, 1972.

[81] Y. C. Fung. Elasticity of soft tissues in simple elongation. *Am. J. Physiol.*, 213:1532–1544, 1967.

[82] A. A. Alhayani, J. Rodriguez, and J. Merodio. Competition between radial expansion and axial propagation in bulging of inflated cylinders with application to aneurysms propagation in arterial wall tissue. *Int. J. Eng. Sci.*, 85:74–89, 2014.

[83] H. Tsai, T. J. Pence, and E. Kirkinis. Swelling induced finite strain flexure in a rectangular block of an isotropic elastic material. *J. Elast.*, 75:69–89, 2004.

[84] T. J. Pence and H. Tsai. Swelling induced microchannel formation in nonlinear elasticity. *IMA J. Appl. Math.*, 70:173–189, 2005.

[85] K. Gou, H. Topol, H. Demirkopraran, and T. J. Pence. Stress-swelling finite element modeling of cervical response with homeostatic collagen fiber distributions. *J. Biomech. Eng.*, 142:081002, 2020.

[86] N. Gundiah, M. B. Ratcliffe, and L. A. Pruitt. The biomechanics of arterial elastin. *J. Mech. Behav. Biomed. Mater.*, 2:288–296, 2009.

[87] H. Topol, K. Gou, H. Demirkoparan, and T. J. Pence. Hyperelastic modeling of the combined effects of tissue swelling and deformation-related collagen renewal in fibrous soft tissue. *Biomech. Model. Mechanobiol.*, 17:1543–1567, 2018.

[88] L. R. G. Treloar. *The Physics of Rubber Elasticity; Third Edition.* Clarendon Press, Oxford, 1975.

[89] V. Zamani, T. J. Pence, H. Demirkoparan, and H. Topol. Hyperelastic models for the swelling of soft material plugs in confined spaces. *Int. J. Nonlin. Mech.*, 106:297–309, 2018.

[90] Soheil Moradalizadeh, Hojjat Nazari, Heiko Topol, and José Merodio. Bulging bifurcation in residually stressed cylindrical double-layered thick-walled cylinders applicable to the modeling of arteries. *Journal of Applied and Computational Mechanics*, pages –, 2025.

[91] B. S. Elkin, M. A. Shaik, and B. Morrison. Fixed negative charge and the Donnan effect: a description of the driving forces associated with brain tissue swelling and oedema. *Phil. Trans. R. Soc. A.*, 368:585–603, 2010.

[92] W. M. Lai, J. S. Hou, and V. C. Mow. A triphasic theory for the swelling and deformation behavior of articular-cartilage. *J Biomech. Eng.*, 113:245–258, 1991.

[93] G. E. Lang, P. S. Stewart, D. Vella, S. L. Waters, and A. Goriely. Is the Donnan effect sufficient to explain swelling in brain tissue slices? *J. R. Soc. Interface*, 11:1120140123, 2014.

[94] N.K. Jha, J. Merodio, and J. Reinoso. A general non-local constitutive relation for residually stressed solids. *Mechanics Research Communications*, 101:103421, 2019.

[95] Andrey Melnikov, Jose Merodio, Roger Bustamante, and Luis Dorfmann. Bifurcation analysis of residually stressed neo-hookean and ogden electroelastic tubes. *Philos. Trans. A Math. Phys. Eng. Sci.*, 380(2234):20210331, October 2022.

[96] Murtadha J. Al-Chlaihawi, Dariel Desena-Galarza, Heiko Topol, and José Merodio. Computational modeling of a residually stressed thick-walled cylinder under the combined action of axial extension and inflation. *Finite Elements in Analysis and Design*, 244:104309, 2025.

[97] D. Desena-Galarza, H. Dehghani, N.K. Jha, J. Reinoso, and J. Merodio. Computational bifurcation analysis for hyperelastic residually stressed tubes under combined inflation and extension and aneurysms in arterial tissue. *Finite Elements in Analysis and Design*, 197:103636, December 2021.

[98] H. Topol, H. Demirkoparan, and T. J. Pence. On collagen fiber morphoelasticity and homeostatic remodeling tone. *J. Mech. Behav. Biomed. Mater.*, 113:104154, 2021.

[99] H. Topol, N. K. Jha, H. Demirkoparan, M. Stoffel, and J. Merodio. Bulging of inflated membranes made of fiber reinforced materials with different natural configurations. *Eur. J. Mech. A - Solids*, 96:104670, 2022.

[100] M.H.B.M. Shariff and J. Merodio. Residually stressed two fibre solids: A spectral approach. *International Journal of Engineering Science*, 148:103205, 2020.

[101] Jose Merodio and Anthony Rosato. *General Overview of Continuum Mechanics*, volume 51, pages 1–52. January 2012.

[102] A. Wineman and T. J. Pence. Fiber-reinforced composites: nonlinear elasticity and beyond. *J. Eng. Math.*, 127:30, 2021.

[103] H. Topol, H. Demirkoparan, and T. J. Pence. Fibrillar collagen: A review of the mechanical modeling of strain-mediated enzymatic turnover. *Appl. Mech. Rev.*, 73:050802, 2021.

[104] Mustapha El Hamdaoui, José Merodio, and Ray W. Ogden. Loss of ellipticity in the combined helical, axial and radial elastic deformations of a fibre-reinforced circular cylindrical tube. *International Journal of Solids and Structures*, 63:99–108, 2015.

[105] W. Zhang, G. Sommer, J. A. Niestrawska, G. A. Holzapfel, and D. Nordsletten. The effects of viscoelasticity on residual strain in aortic soft tissues. *Acta Biomater.*, 140:398–411, 2022.

[106] P.C. Vinh, V.T.N. Anh, J. Merodio, and L.T. Hue. Explicit transfer matrices of pre-stressed elastic layers. *International Journal of Non-Linear Mechanics*, 106:288–296, 2018.

[107] W. Ehlers and B. Markert. A linear viscoelastic biphasic model for soft tissues based on the theory of porous media. *J. Biomech. Eng.*, 123:418–424, 2001.

[108] Z. Guo, J. Gattas, S. Wang, L. Li, and F. Albermani. Experimental and numerical investigation of bulging behaviour of hyperelastic textured tubes. *Int. J. Mech. Sci.*, 115-116:665–675, 2016.

[109] J. D. Humphrey. Vascular adaptation and mechanical homeostasis at tissue, cellular, and sub-cellular levels. *Cell Biochemistry and Biophysics*, 50(2):53–78, October 2007.

[110] C. J. Cyron, R. C. Aydin, and J. D. Humphrey. A homogenized constrained mixture (and mechanical analog) model for growth and remodeling of soft tissue. *Biomechanics and Modeling in Mechanobiology*, 15(6):1389–1403, March 2016.

[111] Ataollah Ghavamian, S. Jamaleddin Mousavi, and Stéphane Avril. Computational study of growth and remodeling in ascending thoracic aortic aneurysms considering variations of smooth muscle cell basal tone. *Frontiers in Bioengineering and Biotechnology*, 8, November 2020.

[112] Andrii Grytsan, Thomas Eriksson, Paul Watton, and T. Gasser. Growth description for vessel wall adaptation: A thick-walled mixture model of abdominal aortic aneurysm evolution. *Materials*, 10(9):994, August 2017.

[113] S. Jamaleddin Mousavi, Solmaz Farzaneh, and Stéphane Avril. Patient-specific predictions of aneurysm growth and remodeling in the ascending thoracic aorta using the homogenized constrained mixture model. *Biomechanics and Modeling in Mechanobiology*, 18(6):1895–1913, June 2019.

[114] Floriane Anstett-Collin, Thierry Mara, and Michel Basset. Application of global sensitivity analysis to a tire model with correlated inputs. *Simul. Model. Pract. Theory*, 44:54–62, May 2014.

[115] G E B Archer, A Saltelli, and I M Sobol. Sensitivity measures,anova-like techniques and the use of bootstrap. *J. Stat. Comput. Simul.*, 58(2):99–120, May 1997.

[116] Hadi Asghari, Heiko Topol, Bernd Markert, and José Merodio. Application of sensitivity analysis in extension, inflation, and torsion of residually stressed circular cylindrical tubes. *Probabilistic Eng. Mech.*, 73(103469):103469, July 2023.

[117] D Balzani, J Schröder, and D Gross. Numerical simulation of residual stresses in arterial walls. *Comput. Mater. Sci.*, 39(1):117–123, March 2007.

[118] William Becker. Metafunctions for benchmarking in sensitivity analysis. *Reliab. Eng. Syst. Saf.*, 204(107189):107189, December 2020.

[119] R Bustamante and J Merodio. On simple constitutive restrictions for transversely isotropic nonlinearly elastic materials and isotropic magneto-sensitive elastomers. *J. Eng. Math.*, 68(1):15–26, September 2010.

[120] R Bustamante and J Merodio. Constitutive structure in coupled non-linear electro-elasticity: Invariant descriptions and constitutive restrictions. *Int. J. Non Linear Mech.*, 46(10):1315–1323, December 2011.

[121] R Bustamante and J Merodio. On weak formulations and their second variation in nonlinear electroelasticity. *Mech. Res. Commun.*, 46:15–19, December 2012.

[122] G Chagnon, M Rebouah, and D Favier. Hyperelastic energy densities for soft biological tissues: A review. *J. Elast.*, 120(2):129–160, August 2015.

[123] Oscar Luis Cruz-González, Ariel Ramírez-Torres, Reinaldo Rodríguez-Ramos, Raimondo Penta, Julián Bravo-Castillero, Raúl Guinovart-Díaz, José Merodio, Federico J Sabina, and Frederic Lebon. A hierarchical asymptotic homogenization approach for viscoelastic composites. *Mech. Adv. Mater. Struct.*, 28(21):2190–2201, November 2021.

[124] Stelios Kyriakides and Chang Yu-Chung. On the inflation of a long elastic tube in the presence of axial load. *International Journal of Solids and Structures*, 26(9–10):975–991, 1990.

[125] Stelios Kyriakides. Propagating instabilities in structures. page 67–189, 1993.

[126] Y.B. Fu, G.A. Rogerson, and Y.T. Zhang. Initiation of aneurysms as a mechanical bifurcation phenomenon. *International Journal of Non-Linear Mechanics*, 47(2):179–184, March 2012.

[127] Y.B. Fu, S.P. Pearce, and K.K. Liu. Post-bifurcation analysis of a thin-walled hyperelastic tube under inflation. *International Journal of Non-Linear Mechanics*, 43(8):697–706, October 2008.

[128] N.K. Jha, J. Reinoso, H. Dehghani, and J. Merodio. Constitutive modeling framework for residually stressed viscoelastic solids at finite strains. *Mechanics Research Communications*, 95:79–84, January 2019.

[129] Gerhard A. Holzapfel and Ray W. Ogden. Modelling the layer-specific three-dimensional residual stresses in arteries, with an application to the human aorta. *Journal of The Royal Society Interface*, 7(46):787–799, October 2009.

[130] A Dorfmann, J Merodio, and R W Ogden. Non-smooth solutions in the azimuthal shear of an anisotropic nonlinearly elastic material. *Journal of Engineering Mathematics*, 68(1):27–36, September 2010.

[131] Manuel Doblaré and José Merodio. An introduction to biomechanics and mechanobiology. 2017.

[132] K P Soldatos, M H B M Shariff, and J Merodio. On the constitution of polar fiber-reinforced materials. *Mech. Adv. Mater. Struct.*, 28(21):2255–2266, November 2021.

[133] N.T. Nam, J. Merodio, R.W. Ogden, and P.C. Vinh. The effect of initial stress on the propagation of surface waves in a layered half-space. *International Journal of Solids and Structures*, 88–89:88–100, June 2016.

[134] J. Rodríguez and J. Merodio. Helical buckling and postbuckling of pre-stressed cylindrical tubes under finite torsion. *Finite Elements in Analysis and Design*, 112:1–10, May 2016.

[135] T. Ahamed, L. Dorfmann, and R.W. Ogden. Modelling of residually stressed materials with application to aaa. *Journal of the Mechanical Behavior of Biomedical Materials*, 61:221–234, August 2016.

[136] Dassault Systemes Simulia Corp. *Abaqus Theory Manual, Abaqus 2016 Documentation.* SIMULIA (Dassault Systemes), 2016.

[137] N.-K. Jha, J. Reinoso, H. Dehghani, and J. Merodio. A computational model for fiber-reinforced composites: hyperelastic constitutive formulation including residual stresses and damage. *Computational Mechanics*, 63(5):931–948, September 2018.

[138] J. Merodio and R. W. Ogden. Extension, inflation and torsion of a residually-stressed circular cylindrical tube. *Continuum Mech. Thermodyn.*, 28:157–174, 2016.

[139] Valentina Balbi and Pasquale Ciarletta. Helical buckling of thick-walled, pre-stressed, cylindrical tubes under a finite torsion. *Math. Mech. Solids*, 20(6):625–642, July 2015.

[140] A John Bailer. Probabilistic techniques in exposure assessment. a handbook for dealing with variability and uncertainty in models and inputs. a. c. cullen and h. c. frey, plenum press, new york and london, 1999. no. of pages: Ix + 335. price: $99.50., isbn= 0-306-45956-6. *Stat. Med.*, 20(14):2211–2213, July 2001.

[141] Etienne de Rocquigny, Nicolas Devictor, and Stefano Tarantola, editors. *Uncertainty in industrial practice*. Wiley-Blackwell, Hoboken, NJ, May 2008.

[142] J. Merodio and R. W. Ogden. Material instabilities in fiber-reinforced nonlinearly elastic solids under plane deformation. *Archives of Mechanics*, 54:525–552, 2002.

[143] José Merodio and Raymond Ogden, editors. *Constitutive modelling of solid continua*. Solid mechanics and its applications. Springer Nature, Cham, Switzerland, 1 edition, November 2019.

[144] J. Merodio. *Equilibrium Shocks in a Directionally Reinforced Neo-Hookean Material Under Plane Deformation*. Michigan State University. Department of Materials Science and Mechanics, 1999.

[145] Heiko Topol, Niraj Kumar Jha, Hasan Demirkoparan, Marcus Stoffel, and José Merodio. Bulging of inflated membranes made of fiber reinforced materials with different natural configurations. *Eur. J. Mech. A Solids*, 96(104670):104670, November 2022.

[146] Heiko Topol, Hasan Demirkoparan, Marcus Stoffel, Bernd Markert, and José Merodio. Bifurcation of fiber reinforced inflated membranes with different natural configurations of the constituents. *Proc. Appl. Math. Mech.*, 22(1), March 2023.

[147] Cornelius O Horgan and Jeremiah G Murphy. Torsion of incompressible fiber-reinforced nonlinearly elastic circular cylinders. *J. Elast.*, 103(2):235–246, April 2011.

[148] Qin Liu, Qi Wen, Mohammad Mottahedi, and Hai-Chao Han. Artery buckling analysis using a four-fiber wall model. *J. Biomech.*, 47(11):2790–2796, August 2014.

[149] Mohammad Mottahedi and Hai-Chao Han. Artery buckling analysis using a two-layered wall model with collagen dispersion. *J. Mech. Behav. Biomed. Mater.*, 60:515–524, July 2016.

[150] A A Alhayani, J Rodríguez, and J Merodio. Numerical analysis of neck and bulge propagation in anisotropic tubes subject to axial loading and internal pressure. *Finite Elem. Anal. Des.*, 90:11–19, November 2014.

[151] Hai-Chao Han. Twisted blood vessels: symptoms, etiology and biomechanical mechanisms. *J. Vasc. Res.*, 49(3):185–197, March 2012.

[152] Mohammadali Sharzehee, Fatemeh Fatemifar, and Hai-Chao Han. Computational simulations of the helical buckling behavior of blood vessels. *Int. J. Numer. Method. Biomed. Eng.*, 35(12):e3277, December 2019.

[153] Mustapha El Hamdaoui, José Merodio, and Ray W Ogden. Deformation induced loss of ellipticity in an anisotropic circular cylindrical tube. *J. Eng. Math.*, 109(1):31–45, April 2018.

[154] M.EL Hamdaoui and J. Merodio. A note on finite elastic deformations of fiber-reinforced non-linearly elastic tubes. *Archives of Mechanics*, 67(1):95–109, 2015.

[155] G. Chagnon, M. Rebouah, and D. Favier. Hyperelastic energy densities for soft biological tissues: A review. *J. Elast.*, 120:129–160, 2015.

[156] Justin R Garcia, Arnav Sanyal, Fatemeh Fatemifar, Mohammad Mottahedi, and Hai-Chao Han. Twist buckling of veins under torsional loading. *J. Biomech.*, 58:123–130, June 2017.

[157] Pierre Badel, Christian Pierre-Yves Rohan, and Stéphane Avril. Finite element simulation of buckling-induced vein tortuosity and influence of the wall constitutive properties. *J. Mech. Behav. Biomed. Mater.*, 26:119–126, October 2013.

[158] Dar Weiss, Cristina Cavinato, Authia Gray, Abhay B Ramachandra, Stephane Avril, Jay D Humphrey, and Marcos Latorre. Mechanics-driven mechanobiological mechanisms of arterial tortuosity. *Sci. Adv.*, 6(49):eabd3574, December 2020.

[159] Justin R Garcia, Shawn D Lamm, and Hai-Chao Han. Twist buckling behavior of arteries. *Biomech. Model. Mechanobiol.*, 12(5):915–927, October 2013.

[160] E Riks. An incremental approach to the solution of snapping and buckling problems. *Int. J. Solids Struct.*, 15(7):529–551, 1979.

[161] Avione Y Lee, Boyang Han, Shawn D Lamm, Cesar A Fierro, and Hai-Chao Han. Effects of elastin degradation and surrounding matrix support on artery stability. *Am. J. Physiol. Heart Circ. Physiol.*, 302(4):H873–84, February 2012.

[162] Heiko Topol, Murtadha J Al-Chlaihawi, Hasan Demirkoparan, and José Merodio. Bulging initiation and propagation in fiber-reinforced swellable Mooney–Rivlin membranes. *J. Eng. Math.*, 128(1), June 2021.

[163] Heiko Topol, Hasan Demirkoparan, and Thomas J Pence. Morphoelastic fiber remodeling in pressurized thick-walled cylinders with application to soft tissue collagenous tubes. *Eur. J. Mech. A Solids*, 77(103800):103800, September 2019.

[164] J A Otero, Y Espinosa-Almeyda, R Rodríguez-Ramos, and J Merodio. Semi-analytical finite element method applied for characterizing micropolar fibrous composites. *Appl. Math. Mech.*, 45(12):2147–2164, December 2024.

[165] M H B M Shariff, R Bustamante, and J Merodio. Basic errors in couple-stress hyperelasticity articles. *Math. Mech. Solids*, 29(9):1729–1738, September 2024.

[166] H Asghari, L Miller, R Penta, and J Merodio. On an isotropic porous solid cylinder: the analytical solution and sensitivity analysis of the pressure. *Appl. Math. Mech.*, 45(9):1499–1522, September 2024.

[167] Hadi Asghari, Heiko Topol, Jesús Lacalle, and José Merodio. Sensitivity analysis of fibrous thick-walled tubes with mechano-sensitive remodeling fibers in homeostasis. *Acta Mech.*, 235(9):5727–5745, September 2024.

[168] Heiko Topol, Hojjat Nazari, Marcus Stoffel, Bernd Markert, Jesús Lacalle, and José Merodio. Instabilities of an inflated and extended doubly fiber-reinforced cylindrical membrane under damage processes and different natural configurations of its constituents with application to abnormal artery dilation. *Thin-Walled Struct.*, 197(111562):111562, April 2024.

[169] M H B M Shariff, R Bustamante, and J Merodio. A generalized strain model for nonlinear residually stressed magneto-electrically coupled viscoelastic solids. *Int. J. Solids Struct.*, 289(112659):112659, March 2024.

[170] Soheil Moradalizadeh, Heiko Topol, Hasan Demirkoparan, Andrey Melnikov, Bernd Markert, and José Merodio. Remarks on bifurcation of an inflated and extended swellable isotropic tube. *Math. Mech. Solids*, 29(3):474–493, March 2024.

[171] A Valverde-González, J Reinoso, N K Jha, J Merodio, and M Paggi. A phase field approach to fracture for hyperelastic and visco-hyperelastic materials applied to pre-stressed cylindrical structures. *Mech. Adv. Mater. Struct.*, 31(4):749–768, February 2024.

[172] Heiko Topol, Alejandro Font, Andrey Melnikov, Jesús Lacalle, Marcus Stoffel, and José Merodio. On the inflation, bulging/necking bifurcation and post-bifurcation of a cylindrical membrane under limited extensibility of its constituents. *Math. Mech. Solids*, January 2024.

[173] M Doblare and J Merodio. *Biomechanics*. Encyclopedia of Life Support Systems (EOLSS) Publications, 2015.

[174] M Doblare and J Merodio. An introduction to biomechanics and mechanobiology. *Encyclopedia of Life Support Systems (EOLSS) Publications*, pages 1–37, 2015.

[175] J Merodio and G Saccomandi. *Continuum mechanics - volume I, II, III*. Encyclopedia of Life Support Systems (EOLSS) Publications, 2011.

[176] J. Merodio and R. W. Ogden, editors. *Constitutive Modelling of Solid Continua*. Springer Cham, 2020.

[177] J Merodio and R Ogden. Basic equations of continuum mechanics. *Constitutive Modelling of Solid Continua Eds.*, pages 1–16, 2020.

[178] Hadi Asghari, Heiko Topol, Jesús Lacalle, and José Merodio. Sensitivity analysis of an inflated and extended fiber-reinforced membrane with different natural configurations of its constituents. *Math. Mech. Solids*, August 2024.

[179] H Asghari, H Topol, B Markert, and J Merodio. Application of the extended fourier amplitude sensitivity testing (FAST) method to inflated, axial stretched, and residually stressed cylinders. *Appl. Math. Mech.*, 44(12):2139–2162, December 2023.

[180] Pietro Mascheroni, Raimondo Penta, and José Merodio. The impact of vascular volume fraction and compressibility of the interstitial matrix on vascularised poroelastic tissues. *Biomech. Model. Mechanobiol.*, 22(6):1901–1917, December 2023.

[181] Heiko Topol, Hadi Asghari, Marcus Stoffel, Bernd Markert, and José Merodio. Post-bifurcation of inflated fibrous cylindrical membranes under different fiber configurations. *Eur. J. Mech. A Solids*, 101(105065):105065, September 2023.

[182] N K Jha, S Moradalizadeh, J Reinoso, H Topol, and J Merodio. On the helical buckling of anisotropic tubes with application to arteries. *Mech. Res. Commun.*, 128(104067):104067, February 2023.

Arc length methods

.1 Introduction

Finite element analysis (FEA) stands as a cornerstone in engineering and scientific disciplines, providing a versatile computational framework for simulating complex physical phenomena. One of the challenges encountered in solving nonlinear finite element problems is tracking solution paths efficiently, particularly when dealing with structures subjected to large deformations, material nonlinearities, or geometric instabilities. Traditional solution methods, such as Newton-Raphson iteration, may face convergence difficulties or encounter abrupt changes in solution behavior, necessitating robust techniques to ensure numerical stability and convergence. The arc-length algorithm emerges as a powerful tool in this context, offering an effective approach for traversing nonlinear solution paths and capturing post-bifurcation behavior accurately. The arc-length method, also known as the load control method, is a numerical technique employed to solve nonlinear finite element problems by incrementally tracking equilibrium paths in load-displacement space. Unlike traditional methods that rely solely on displacement increments, the arc-length algorithm introduces an additional parameter, typically termed as the arc-length or load factor, to govern the magnitude of load increments. This parameter enables the algorithm to follow a smooth path in solution space, mitigating convergence issues associated with abrupt changes or singularities in the response. The fundamental principle underlying the arc-length algorithm lies in maintaining equilibrium at each iteration while simultaneously controlling the magnitude of load increments to ensure numerical stability. At each step, the algorithm iteratively adjusts the load factor to satisfy equilibrium conditions and incrementally advances along the solution path. By incorporating both displacement and load increments, the arc-length method offers robustness and flexibility in handling a wide range of nonlinearities, including material nonlinearities, large deformations, and geometric instabilities. The arc-length algorithm can be formulated within the framework of the finite element method, where the governing equations are discretized using suitable approximation schemes, such as linear or nonlinear finite elements. At each iteration, the algorithm solves the nonlinear equilibrium equations, typically expressed as a system of algebraic equations, using iterative techniques such as Newton-Raphson iteration or modified Newton methods. In addition to enforcing equilibrium, the algorithm adjusts the load factor to control the arc-length of the solution path, ensuring smooth and stable convergence. One of the key advantages of the arc-length method is its ability to handle bifurcation and post-bifurcation phenomena effectively. Bifurcation occurs when the structure undergoes a qualitative change in its response, leading to multiple equilibrium solutions or

instability points in load-displacement space. By continuously monitoring the arc-length parameter and detecting changes in solution behavior, the algorithm can accurately capture bifurcation points and track post-bifurcation paths, enabling the analysis of complex nonlinear behavior such as snap-through, limit point, or periodic instabilities. Moreover, the arc-length algorithm facilitates the simulation of load-controlled processes, where the applied load or boundary conditions vary continuously over time. By adjusting the load factor dynamically in response to changing external loads, the algorithm ensures stable and accurate solutions throughout the simulation. This feature is particularly valuable in applications involving dynamic or transient phenomena, where the response may exhibit nonlinear behavior under varying loading conditions. In summary, the arc-length algorithm represents a robust and efficient approach for solving nonlinear finite element problems, offering superior convergence properties and the ability to capture complex solution paths accurately. By incorporating both displacement and load increments, controlling the arc-length parameter, and detecting bifurcation phenomena, the algorithm enables the simulation of a wide range of nonlinear behaviors encountered in engineering and scientific applications. In the following sections, we will delve deeper into the theoretical foundations, implementation aspects, and practical considerations of the arc-length method, illustrating its effectiveness through numerical examples and case studies.

.2 Basic equations

According to general arc length schemes, the loading parameter λ_{n+1} at time t_{n+1}, introduced to incrementally increase the load magnitude, is allowed to vary during the iteration process. The particular value of the loading parameter is governed by a non-linear scalar constrain equation of the form $f(\psi_{n+1}, \lambda_{n+1}) = 0$ in terms of the current displacement ψ_{n+1}: For the sake of clarity, we restrict the following description to uncoupled purely mechanical problems; the extension to coupled problems is straightforward. Consequently, the residual format of the non-linear balance of momentum enhanced by the constraint equation reads:

$$r^{\psi}(\psi, \lambda) = f^{\psi}_{int}(\psi) - \lambda f^{\psi}_{ext} = 0 \tag{1}$$

$$f(\psi, \lambda) = 0 \tag{2}$$

where here and in the following, we often omit the subscript index $n + 1$ associated with time t_{n+1} as well as the dependencies on ψ and λ for the sake of readability. A Taylor series expansion around the solution at the current iteration step l-terms of quadratic and higher order being neglected gives:

$$r^{\psi}_{l+1} = r^{\psi}_{l} + \delta r^{\psi} = 0 \tag{3}$$

$$f_{l+1} = f_{l} + \delta f = 0 \tag{4}$$

with the increments of the residuals:

$$\delta r^{\psi} = \frac{dr^{\psi}}{d\psi}\delta\psi + \frac{dr^{\psi}}{d\lambda}\delta\lambda \tag{5}$$

$$\delta f = \frac{df}{d\psi}\delta\psi + \frac{df}{d\lambda}\delta\lambda \tag{6}$$

Herein, the increments $\delta\psi = \psi_{l+1} - \psi_l$ and $\delta\lambda = \lambda_{l+1} - \lambda_l$ represent the difference between the values at iteration step $l+1$ and l, while the derivatives are abbreviated by:

$$K^{\psi\psi} = \frac{dr^{\psi}}{d\psi} \tag{7}$$

$$r_{,\lambda}\frac{dr^{\psi}}{d\lambda} = -f_{ext} \tag{8}$$

This results in the following linearized system of equations on element level:

$$\begin{bmatrix} K^{\psi\psi} & -f_{ext} \\ f_{,\psi} & f_{,\lambda} \end{bmatrix} \cdot \begin{bmatrix} d\psi \\ d\lambda \end{bmatrix} = \begin{bmatrix} \lambda f_{ext}^{\psi} - f_{int}^{\psi} \\ -f \end{bmatrix} \tag{9}$$

which is neither symmetric nor banded. The solution of this system of equations can be obtained by means of so-called block solutions:

$$\delta\psi_r = K^{\psi\psi-1}(\lambda f_{ext}^{\psi} - f_{int}^{\psi}) \tag{10}$$

$$\delta\psi_{\lambda} = K^{\psi\psi-1}.f_{ext}^{\psi} \tag{11}$$

which enable us to give an explicit representation for the increment of the loading factor:

$$\delta\lambda = -\frac{f + f_{,\psi}\delta\psi_r}{f_{,\psi}\delta\psi_{\lambda} + f_{,\lambda}} \tag{12}$$

Based on this, the increment in placement is calculated as:

$$\delta\psi = \delta\psi_r + \delta\lambda.\delta\psi\lambda \tag{13}$$

and the updates of displacements and loading parameter then read $\psi_{l+1} = \psi_l + \delta\psi$ and $\lambda_{l+1} = \lambda_l + \delta\lambda$. Note, that within the predictor step at t_0, constraint condition 4 is not determined. As a remedy, the loading parameter λ_n is increased by one providing the displacement increment based on the last equilibrium state (ψ_n, λ_n) reads as:

$$\delta\psi_{\lambda} = K^{\psi\psi-1}.f_{ext}^{\psi} \tag{14}$$

and the distance to the last equilibrium point reads as:

$$s_0 = \sqrt{1 + \delta\psi_{\lambda}\delta\psi_{\lambda}} \tag{15}$$

Comparing the distance s_0 and the prescribed arc length d, the increments of the loading parameter and the placement can be scaled by $\delta\lambda = \frac{s}{s_0}$ and $\delta\psi = \frac{s}{s_0}$. The updates of the displacements ψ_{l+1} and the loading-parameter λ_{l+1} can then be calculated for $l = 0$.

The constraint equation 2 remains to be specified. Different solution strategies are suggested in the literature as summarized, for instance, One prominent example is the

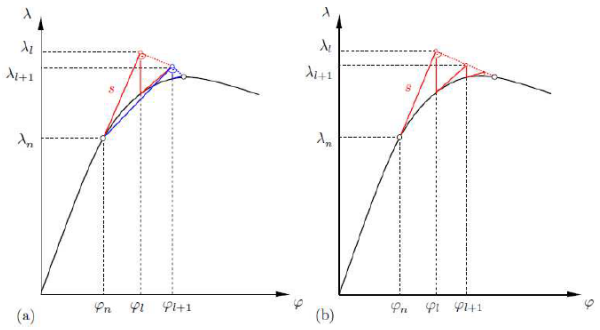

Figure 1: Illustration of arc-length methods according to Crisfi
eld [2]. (a) Iteration on the current normal plane (Ramm's method), (b) Iteration on the initial normal plane (Riks-Wemper method). Quantities without subscript n is associated with t_{n+1}.

iteration on the current normal plane according to Crisfield [2] which is referred to as the Ramm's method.

Following this approach, which is illustrated in Fig. A.1(a), the equation

$$f = (\psi - \psi_n).(\psi_{l+1} - \psi_l) + (\lambda_l - \lambda_n).(\lambda_{l+1} - \lambda_l) \tag{16}$$

constrains the solution to the normal plane with respect to the current iteration step. According to equation 12, the related increment can be specified as:

$$\delta\lambda = \frac{(\psi_n - \psi)\psi_r}{\lambda_l + \lambda_n + \psi_\lambda(\lambda_n - \lambda)} \tag{17}$$

Within this approach, the increment size is limited by moving a given distance along the tangent of the current solution point. Equilibrium is then sought in the plane that passes through the point thus obtained and that is normal to the same tangent. Moreover, the constraint 17 ensures that the iterative change is always normal to the secant change, which causes the equilibrium-search to be normal to the tangent of the previous iteration step, rather than to the tangent at the beginning of the increment.